Study of Precipitation Kinetics and Strengthening in Mg-Zn Alloys

by

Yi Yang
B.Eng., M.Sc.

Submitted in fulfilment of the requirements for the degree of
Doctor of Philosophy

Deakin University
June 2023

DEAKIN UNIVERSITY
CANDIDATE DECLARATION

I certify the following about the thesis entitled:

"Study of Precipitation Kinetics and Strengthening in Mg-Zn Alloys"

submitted for the degree of **Doctor of Philosophy (Engineering)**

a. I am the creator of all or part of the whole work(s) (including content and layout) and that where reference is made to the work of others, due acknowledgment is given.

b. The work(s) are not in any way a violation or infringement of any copyright, trademark, patent, or other rights whatsoever of any person.

c. That if the work(s) have been commissioned, sponsored or supported by any organisation, I have fulfilled all of the obligations required by such contract or agreement.

d. That any material in the thesis which has been accepted for a degree or diploma by any university or institution is identified in the text.

e. All research integrity requirements have been complied with.

'I certify that I am the student named below and that the information provided in the form is correct'

Full Name: Yi Yang

Signed: Yi Yang

Date: 15/06/2023

Acknowledgement

First, my sincerest gratitude and respect go to my principal supervisor, Prof. Matthew R. Barnett, for offering me this great opportunity to work on this exciting project. His constant support, insightful opinions and genuine passion towards knowledge have greatly helped me to complete this unforgettable journey and will keep inspiring me to be a better person.

I am also deeply grateful to my external supervisor, Prof. Michel Perez at INSA Lyon, for his invaluable support and guidance during my PhD study. His profound knowledge of precipitation simulation and strong curiosity about learning new things keep me motivated. This work would not be achieved without his help.

My sincere thanks go to my associate supervisors Dr. Thomas Dorin and Dr. Sitarama Raju Kada. They always provide strong support to solve the problems that I encountered during my study. Their help on my Atom probe and X-ray diffraction data collection, experiment data analysis and academic writing is greatly appreciated.

I am indebted to many of my colleagues and friends from the metal group. I want to express my greatest gratitude to Dr. Jun Wang, who not only provides me the material and helped me with Electron back-scattered diffraction for my project, but also offers many meaningful discussions. I will never forget he and his wife Mrs. Xiang Ding helped me settle down in Australia and supported me through my toughest times. I am deeply grateful to Dr. Mahmoud Reza Ghandehari Ferdowsi, his invaluable assistance on Electron back-scattered diffraction and Transmission electron microscope characterization is greatly appreciated. Many thanks to Dr. Lu Jiang for the help with Atom probe tomography, and Dr. Alban de Vaucorbeil for the valuable discussions about simulation. I would also like to thank Huan Wang, Tao Zhang, Daniel Grasser, Kyle Stephan Nicholson, Steven Babaniaris, Jun Cheng and Ramesh Kumar Varma for their generous advice and support during my study.

I am thankful for all the assistance and training I received from the technician team: Mr. John Vella, Mr. Mohan Setty, Mr. Robert Pow, Mr. Robert Lovett and Dr. Huaying Yin.

I sincerely appreciate the MATEIS team in INSA Lyon for their generous support during my study in France. Thank Prof. Damien Fabrègue for organising this great opportunity. My special thanks go to Dr. Véronique Massardier for helping me perform my experiment

on Thermoelectric power and Dr. Arnaud Allera for his kind assistance in programming the model for this study.

Also, my sincere appreciation goes to my friends in Australia for their dearest support and company, which makes my life here so memorable: Rania, Yuen, Ana, Priyanka, Pascal, Sith, Alex, Florant, Pao, Khagesh, Vamsi, Milad, Cyril, Jan, Shauna, Chao, Mauricio and the McCoy family.

The funding provided by Deakin University and China Scholarship Council (File No. 201706370176) are highly acknowledged.

Last but not least, my utmost thanks go to my family. To my parents, LiQing Luo and YingGuo Yang, I am forever indebted to them for their unconditional love and support throughout my life.

Abstract

This work is dedicated to a further understanding of precipitation kinetics in Mg-Zn alloys and how the precipitation influences slip and twinning.

Firstly, the precipitate evolution in a Mg-4.5 wt.%Zn alloy is characterized using a combination of Thermoelectric power, X-ray diffraction, Atom probe tomography and transmission electron microscopy. The experimental results are then supported by a modified KWN model from thermodynamics aspects. It is found that rod-shaped precipitates are prevalent in the early ageing stage while plate-shaped precipitates dominate over-ageing stage, the kinetics of both precipitates are depicted in detail to represent this competition. The solubility limit of the studied system is also found lower than that in current databases.

Secondly, an Orowan-based mechanical model is developed to predict the precipitation strengthening on slip in aged Mg-Zn alloys. The proposed model considers the strengthening effect of rod and plate-shaped precipitates on basal and prismatic planes, the influences of different precipitate arrangements on modelling results are also discussed. The model is then coupled with the precipitation model to further predict the strength evolution during ageing. It is found that shearing of rod precipitates dominates the strengthening of basal slip at early ageing stages, while the bypass mechanism dominates intermediate and over-ageing stages. On prismatic plane, the bypass of rod precipitates is dominating across all ageing stages. The strengthening from plate-shaped precipitates is found very poor for the studied slip modes. Results agree well with experimental tests.

Finally, the precipitation hardening on twinning plane is studied using an Orowan-based super dislocation model and EBSD analysis. First, the strengthening model has been coupled with the precipitation model to predict the strength evolution during ageing, results are compared with experiment. Next, the twin number density, aspect ratio and volume fraction with different ageing conditions are characterized in detail using EBSD. The twin volume fraction in each ageing condition has then been divided into different Schmid factor classes to observe the orientation effect. Results show that ageing decreases the twin aspect ratio due to the co-influence of precipitates and Zn depletion, while the twin number density is increased with the increased yield strength. The twin volume fractions in low Schmid factor areas for twinning are found to increase more than those in high Schmid factor areas for twinning, it is proposed that slip is hardened more by rod-shaped precipitates than twinning.

Contents

List of Figures

List of tables

1. Introduction

1.1 Overview

As one of the most abundant deposits on earth, magnesium (Mg) has a low density (1.74 g·cm^{-3}) and its alloys show outstanding biocompatibility, excellent damping capability and high specific bending strength [1-4]. They are, therefore, attracting increasing interest in aerospace, transportation, digital communication and biomedical industries. However, the application of Mg alloys can be hampered by relatively low strength and formability, as well as undesirable fatigue resistance [5, 6]. It is thus meaningful to find strategies to overcome these shortcomings.

Age hardening is a typical method to increase the strength of Mg alloys by generating nano-scale precipitates to impede dislocation movement [7]. Though Mg alloys usually have lower age hardening response than that in aluminium alloys, it is observed that the precipitates can increase or decrease the yield asymmetry, by influencing the twinning behaviour, based on their shape and size distributions [2]. Accurate characterization of precipitates microstructural evolution with ageing time is thus essential to establish structure-property relationships for future material development.

Mg-Zn alloy is an important candidate to investigate precipitation hardening. It provides excellent age-hardening response as the solid solubility of Zn decreases sharply with temperature [8]. And the precipitation strengthening in this system can be well described by the Orowan model [9, 10]. However, there is a limited understanding regarding precipitation kinetics in Mg-Zn alloys and its interaction with different deformation modes is still under debate.

On the other hand, twinning on $\{10\bar{1}2\}$ planes is an important plastic strain accommodation mechanism that is readily activated in Mg alloy, which is considered the dominant mechanism in determining the plasticity and strength in certain cases [11, 12]. While it is shown that twinning contributes to almost 45% of the macroscopic strain at yielding [13], the change of twinning strain under the influence of different precipitate volume fractions and solute levels is not fully understood.

The current research focuses on the further elaboration of precipitation kinetics in Mg-Zn system and investigates the precipitation influences on slip and twinning using a series of characterization techniques and modelling methods. Hopefully, the outcomes of this study could benefit ageing guided mechanical design of Mg alloys for future application.

1.2 Thesis outline

Chapter 2 contains a comprehensive literature review which summarizes the current knowledge related to the field of study. The development of precipitation theories and how precipitates interact with deformation mechanisms in Mg-Zn system are reviewed and discussed. Finally, gaps in knowledge are presented and the scope of this work is discussed.

Chapter 3 introduces the characterization methods and modelling principles that have been applied in the current study.

Chapter 4 studies the precipitation kinetics in Mg-Zn alloy. The size evolution of precipitates during ageing is characterized by Transmission electron microscopy, and the solute evolution is characterized by Thermoelectric power, Atom probe tomography and X-ray diffraction. The experimental results are then used to calibrate a precipitation model which is built on classical nucleation and coarsening theories and the precipitation kinetics in Mg-Zn alloys is discussed. In the end, a TTT diagram is proposed for the studied system.

Chapter 5 is dedicated to developing an Orowan-based mechanical model, coupled with the precipitation model from the previous chapter, to describe the evolution of strength during ageing for Mg-Zn alloys when tensile along extrusion. This model is then compared with the experimental results, and the precipitation hardening on basal and prismatic planes is discussed.

Chapter 6 investigates the precipitates' influence on twinning behaviour. First, a twinning model is coupled with the precipitation model to predict strength evolution during ageing for Mg-Zn alloys when compression along the extrusion direction, following the same strategy in Chapter 5. Then, a in-depth study of twinning behaviour at different ageing conditions is performed using Electron back-scattered diffraction. The change of twin aspect ratio, twin number density and twin fraction under the influence of precipitation is discussed.

Chapter 7 concludes the original contributions from this study and the potential direction for the future work is proposed.

2. Literature review

The first part of this chapter is focusing on the general background theories of precipitation, a summary of the precipitation in Mg-Zn alloys and methods to study precipitation kinetics are also reviewed. The second part summarises the deformation modes that has been studied in Mg alloys and how the precipitates interact with these mechanisms. The last part of this chapter identifies the gaps in literature and the scope of this work is presented.

2.1 Formation of precipitates

2.1.1 Phase equilibrium

In metals, the relative stability of a system at constant temperature and pressure is determined by the Gibbs free energy[14]:

$$G = H - TS \qquad (2.1)$$

Where S is the entropy of the system, T is the absolute temperature and H is enthalpy.

At a given temperature and pressure, atoms in the system always seek to rearrange into one of the states with minimum free energy, i.e. $\mathrm{d}G = 0$. This is where the system reaches its equilibrium. The variation of Gibbs free energy with atom arrangement can be graphically illustrated in Fig. 2.1 [14], as shown, there is a situation where local free energy minima is achieved but do not have the lowest possible value of G (B in Fig. 2.1), such situations are called meta-stable equilibrium to distinguish from the stable equilibrium state (A in Fig. 2.1).

The idea of forming certain precipitates is to induce the system into one of the equilibrium states (often meta-stable) by controlling the temperature and time and locking them between the energy barriers (energy hump in Fig. 2.1) by rapid cooling. In practice, the processes usually include [14-16]: (1) solution treatment at relatively high temperatures followed by water quenching to obtain super-saturated solid solution, and (2) subsequent ageing at lower temperatures to decompose the super-saturated solid solution into finely distributed precipitates.

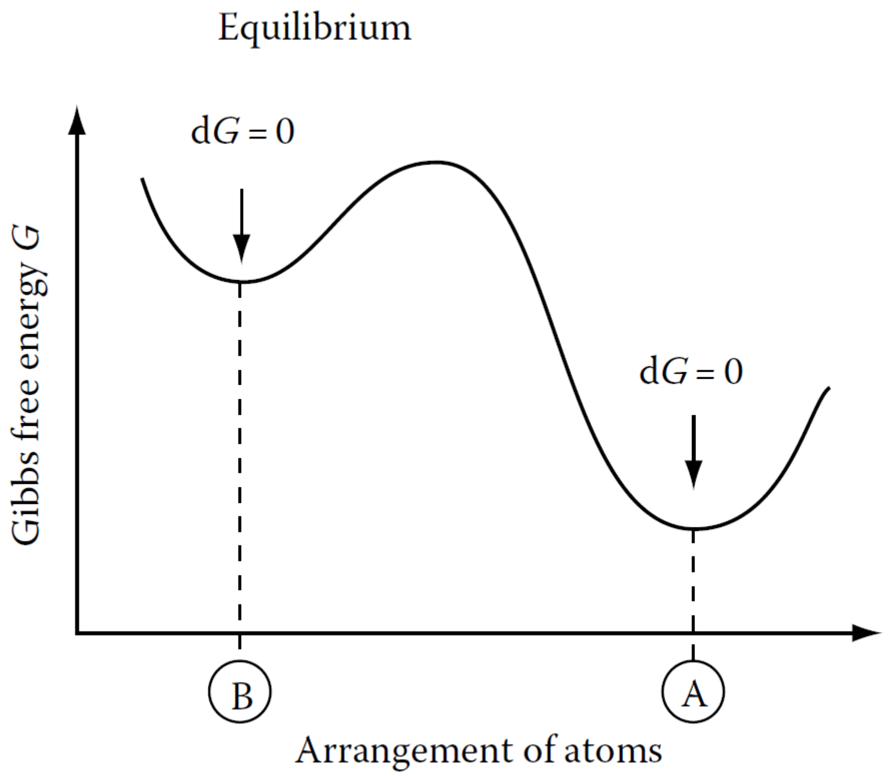

Fig. 2.1 The Gibbs free energy as a function of the arrangement of atoms. A is the stable equilibrium state and B is the meta-stable equilibrium state [14].

2.1.2 Precipitation kinetics

The typical precipitation kinetics comprises three distinct processes [14-17]: nucleation, growth and coarsening. Nucleation corresponds to the formation of new particles and can be categorized into two types [15]: homogeneous nucleation where the nucleation event happens uniformly across the whole parent phase, and heterogeneous nucleation where certain structural sites are preferred to form the nuclei such as grain boundaries or dislocations. Though in engineering alloys the common mechanism is heterogeneous nucleation, homogeneous nucleation is still a popular assumption in many studies as it is easier to treat [16, 18, 19]. Particles generated from supersaturated solid solution change the Gibbs free energy, which for spherical particles can be expressed as [16]:

$$\Delta G = \frac{4}{3}\pi r^3(\Delta G_{ch} + \Delta G_{el}) + 4\pi r^2\gamma \qquad (2.2)$$

Where r is the radius of particle. The left term is volume energy defined by chemical driving force ΔG_{ch} and the elastic energy ΔG_{el} and it scales with the volume of spherical particle $\frac{4}{3}\pi r^3$. This term makes a negative contribution to ΔG. The right term is the surface energy defined by the specific interfacial energy γ and it scales with the surface area $4\pi r^2$. It has a positive contribution to ΔG. The competition between volume and surface energies leads to the formation of new precipitates. Fig. 2.2 illustrates the change of total ΔG in this competition [15], it shows that with the increase of radius r, the free energy first increase until the radius reaches r^*, then keep decreasing. As the system always seeks to minimise the Gibbs free energy, particles that have a value of radius lower than r^* will shrink and dissolve, while particles with a radius larger than r^* will continue growing. r^* is therefore the critical radius for a precipitate to form, and its corresponding ΔG^* is the nucleation energy barrier.

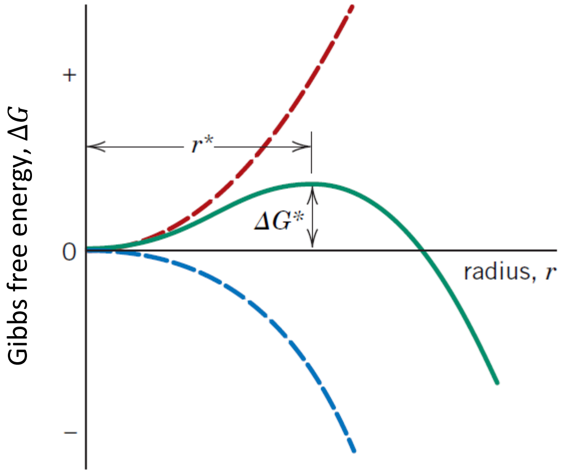

Fig. 2.2 Schematic illustration of the variation of Gibbs free energy as a function of the precipitate radius r. The red line is ΔG caused by surface energy, the blue line is ΔG caused by volume energy and the green line is the total ΔG. ΔG^* is the nucleation energy barrier, r^* is the critical radius for a precipitate to nucleate [15].

The growth of a stable nucleus results in the consumption of parent phase [20]. It is considered a long-range atomic diffusion process, the growth rate is thus determined by the element diffusion coefficient D, which follows an Arrhenius-type law [15, 20]:

$$D = D_0 \exp\left[-\frac{Q}{kT}\right] \quad (2.3)$$

Where T is the absolute temperature, k is the Bolzmann constant, Q is the activation energy and D_0 is the pre-exponential factor. Note that the nucleation can happen continuously accompanying the growth stage.

The coarsening of precipitates is a result of the Gibbs-Thomson effect, in which the local equilibrium and atomic fraction at the interface change due to the presence of curved interfaces between the matrix and precipitates [21]. A consequence is that small precipitates become less stable than the larger ones, so the large precipitates keep growing while the small precipitates will shrink back during the longer ageing time [16, 22]. Coarsening is also a diffusion-controlled process but is slower than growth because the driving force is lower [23]. It does not cause variation of total precipitate volume fraction but it decreases the number density of precipitates. For more detailed description readers are referred to theories developed by Greenwood [24], Wagner [25], and Lifshitz and Slyozov [26].

2.1.3 Morphology of precipitates

The classical nucleation theory assumes particles with spherical shapes, but in practice, the precipitates observed in engineering alloys often have a non-spherical shape [23]. This is reasonable as the precipitate-matrix interface over one particle does not have the same energy over every facet when the precipitates and matrix have different structures. Also, the incoherent interfaces tend to be more mobile [27, 28]. In many alloys, the precipitate shape has not been found to be the one that minimises the total surface energy, and as the precipitate grows larger its shape can be subject to change [29-33]. This is due to the lattice misfit between precipitate and matrix causing elastic stress that can also affect particle shape [34]. The co-influence of interfacial and elastic energies is therefore the major reason for determining the precipitate equilibrium shape [35, 36], their relative importance can be described using the characteristic parameter [37-39]:

$$L = \frac{\varepsilon C r}{\gamma} \qquad (2.4)$$

Where γ is the specific interfacial energy, C is the elastic constant of matrix, ε is the lattice misfit between precipitates and matrix and r is the average precipitate size.

Thompson *et al.* [37] developed a set of Fourier series to describe the shape of a particle that minimises the system energy. The resulting shape of the particle is determined by a Fourier coefficient a^R, its relationship with parameter L is shown in Fig. 2.3 [37]. As can be seen, the spherical precipitates usually correspond to a small L, which can be transformed into an ellipsoidal or cuboidal shape as L increases, in this stage the precipitate size is small and its shape tends to minimise the surface energy. While with larger precipitates size and L, elastic energy gradually takes dominance and low symmetric shapes start to form due to elastic anisotropy.

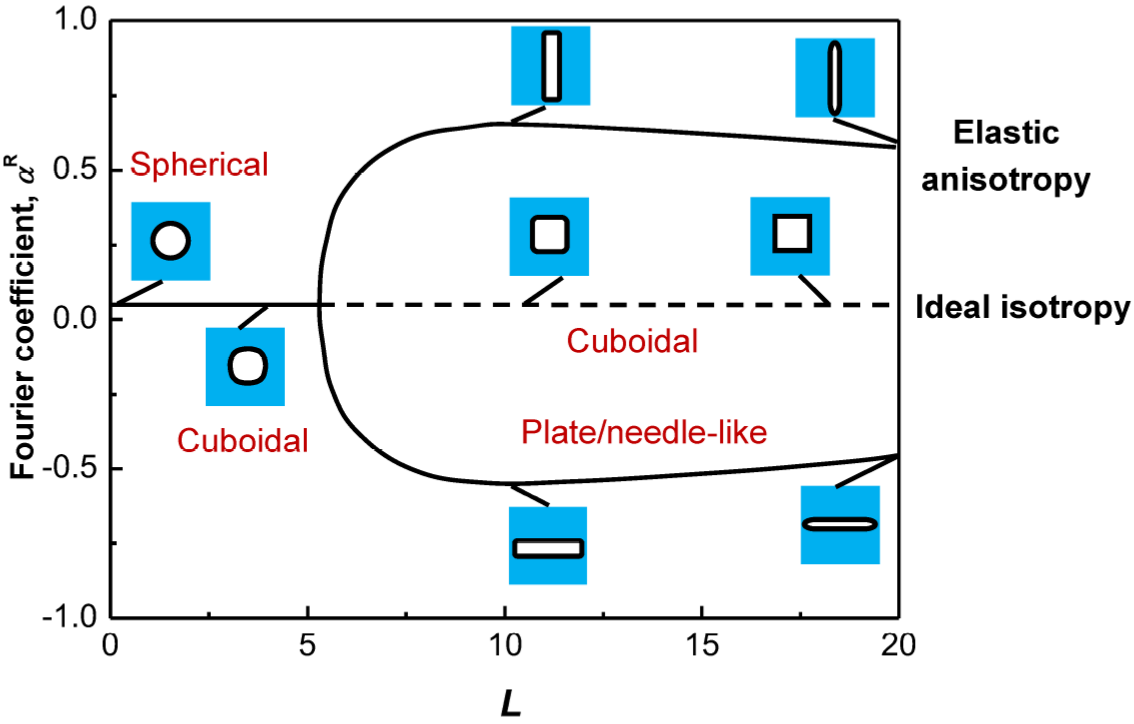

Fig. 2.3 Influence of characteristic parameter L on precipitate morphological shape. The energy that determines particle shape is represented by the Fourier coefficient [37, 39].

2.2 Precipitate species in Mg alloys

In Mg Alloys, the most frequently observed precipitate types are rods along c-axis, basal plates and prismatic plates. Basal plates are most readily formed in Mg-Al, Mg-Ca, Mg-Gd-Zn and Mg-Y-Zn based alloys [40-43]. In Mg-Al based alloys, the precipitates are continuously or discontinuously precipitated directly from the super-saturated solid solution, forming a lamellar structure with α-Mg [40, 44]. In Mg-Ca based alloys, they are thin plates that are finely distributed in the matrix [41]. Prismatic plates are often found in Mg-Nb and Mg-Y-RE alloys [17, 45], their habit plane is parallel to $(10\bar{1}0)_{\text{matrix}}$. The rod-shaped precipitates are typically found as the metastable phase Mg_4Zn_7 in Mg-Zn alloy [46], it can also be formed as an equilibrium phase in Mg-Nb [17]. This precipitate acquires a length multiple times the thickness and forms along the c-axis of $(0001)_{\text{matrix}}$. c-axis rods are also found in Mg-Al based alloys [47, 48].

2.3 Mg-Zn system

2.3.1 Precipitation sequence

A typical phase diagram of Mg-Zn system is shown in Fig. 2.4. It can be seen that, at eutectic temperature (340 °C), the solubility limit of Zn in Mg is 6.2 wt.%, therefore most age hardenable Mg-Zn alloys have a Zn content below 6.2 wt%.

The reported precipitation in Mg-Zn system generally has a sequence as below [46, 49-51]:

"Super-saturated solid solution (SSSS) -> Guinier-Preston (GP) zone -> β_1' precipitate (rod-shape) -> β_2' precipitate (coarse plates) -> β equilibrium phase"

GP zone is a fine-scale solute-enriched region which usually appears during the early stage of precipitation [52]. The GP zone in Mg-Zn system is previously suggested to not appear above 100 °C [46], this is considered as a possible contributor to the poor strengthening effect in aged Mg-Zn alloy. However, recent studies showed the presence of GP zones in aged Mg-Zn alloy containing Ag and Ca [53, 54], which is described as coherent disks parallel to $\{0001\}\alpha$ [49, 55]. It is also reported that β_2' sometimes form prior to or simultaneously with β_1' [17]. Recently, Wang *et al*. [56] justified this phenomenon using first principle study by showing that this is because the formation of β_1' and β_2' are energetically competitive.

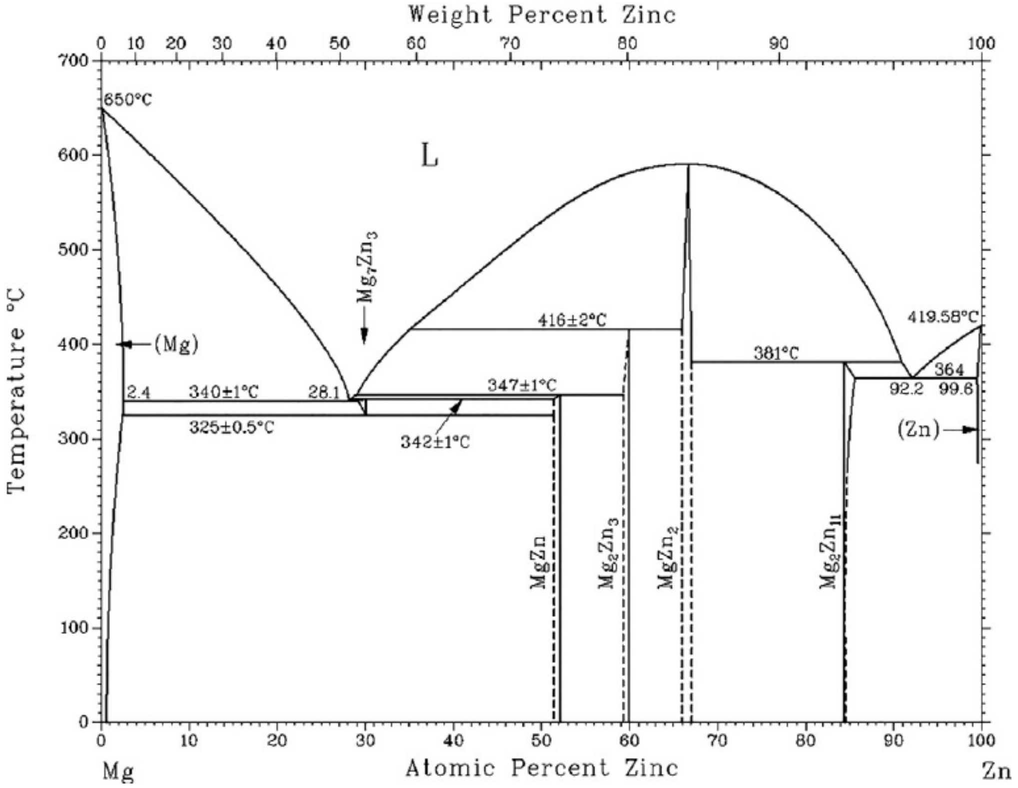

Fig. 2.4 The Mg-Zn phase diagram [57].

2.3.2 Microstructural features of precipitates

Although there are debatable aspects of the precipitation process, it is generally accepted that the density and structure of metastable phases β_1' and β_2' dominate the ageing response in Mg-Zn, because they provide good resistance to basal slip and twinning [46, 58].

From the early X-ray and electron diffraction results and more recent TEM studies [59-64], β_1' forms as [0001] α rods with a base-centred monoclinic structure (a = 2.596 nm, b = 1.428 nm, c = 0.524 nm, γ = 102.5^{o}), its orientation relationship with α-Mg is:

(630) β_1' ~ // (01-10) α, [001] β_1' ~ // [0001] α

Such structure and orientation relationship resembles that of Mg_4Zn_7 and agrees with literature where a similar precipitate structure is reported in Mg-Zn-Y alloys [65-67]. A small amount of blocky-shaped β_1' phase is also found in the same study. Rosalie *et al.* [68] used high-resolution TEM observation and found that β_1' rods can have a co-existence of Mg_4Zn_7 and β_2' ($MgZn_2$) phases for a cast Mg-3Zn alloy aged at 150 ℃.

β_2' forms as (0001) α plates and has a hexagonal structure (a = 0.520 nm, c = 0.857 nm) [59-63], this is close to the structure of $MgZn_2$, whose space group is P63/mmc, a and c are 0.5221 nm and 0.8567 nm respectively. It has an orientation relationship with α-Mg as:

(0001) β_2' // (0001) α, [11-20] β_2' // [10-10] α

The morphology and distributions of precipitates, and the coexistence of Mg_4Zn_7 and $MgZn_2$ in a β_1' precipitate are shown in Fig. 2.5.

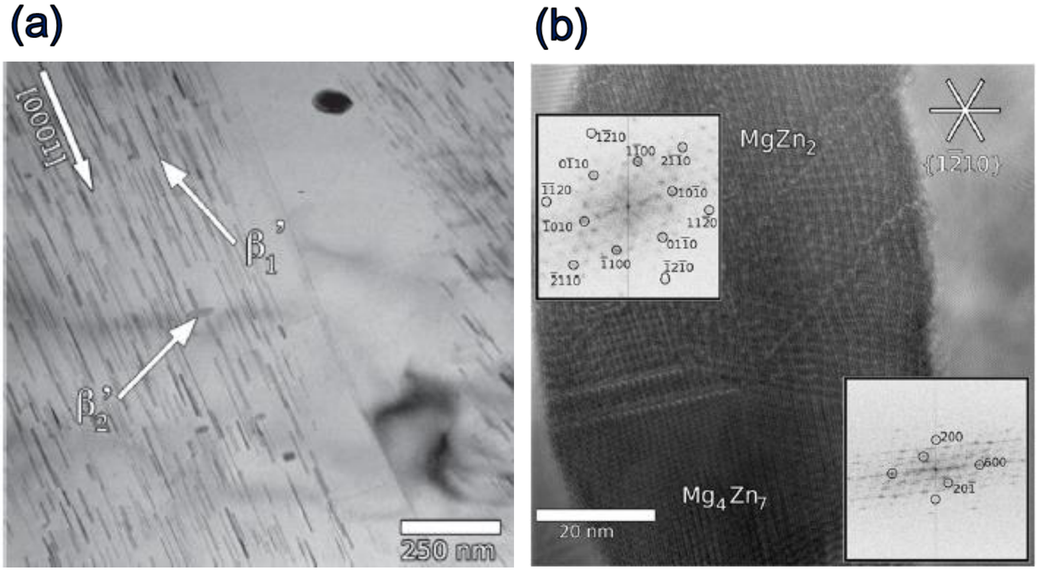

Fig. 2.5 TEM images of (a) the distribution of precipitates in a Mg-3.4Zn alloy aged at 150 ℃ for 48 h [69] and (b) domains of $MgZn_2$ and Mg_4Zn_7 found in the same β_1' precipitate in a Mg-3Zn alloy [68], Fourier transforms of each phase are inset.

Although the structure of the β equilibrium phase has not yet been resolved, it has long been accepted as a triclinic structure close to that of Mg_2Zn_3. Based on the electron microscopy study by Gao *et al.* [70], it is suggested that the β phase has a base-centred monoclinic structure (a = 1.61 nm, b = 2.579 nm, c = 0.88 nm, γ = 112.4°) and a composition of MgZn. Recently, some studies showed a more precise composition of $Mg_{21}Zn_{25}$ [71, 72].

2.4 Methods to study precipitation kinetics

The study of the complete precipitation process has been a long-term focus in metallurgy which can provide insightful information of different precipitation stages, this can be done by interpreting the precipitation kinetics using various experimental techniques coupled with some theoretical modelling. The following review intends to summarize the most used experimental methods and theoretical models in the realm of precipitation kinetics studies.

2.4.1 Experimental methods

Characterizing precipitation kinetics involves measuring the evolution of several parameters as a function of time and temperature. This includes structural information, chemical composition, morphological information, possible spatial distribution and orientation. Generally, if the types of precipitates are already known, measuring hardness evolution is the easiest and most popular way to indirectly follow the precipitation kinetics [7, 46, 73], but it does not provide any microstructural information.

Transmission-electron microscopy (TEM) is one of the most popular techniques to characterize nano-scale precipitates and is particularly useful for measuring the structural, chemical and morphological parameters through high-resolution imageing [74-77]. Recent development further allows TEM to be used in situ to directly image the evolution of precipitation kinetics [78]. But such high-resolution is inevitably restricted to a local region, which challenges the statistical relevance of measurements in terms of kinetics.

Another frequently used in-situ measurement is Small angle scattering (SAS) with X-rays (SAXS) or neutrons (SANS), where the volume fraction and size of precipitates in a bulk region can be directly assessed by analysing the scattering intensity in the reciprocal space [79, 80]. SAS interpretation can be complex in the case where multiple precipitate species are present and when precipitates display anisotropic morphologies. It is necessary to combine SAS with other techniques such as TEM or Differential scanning calorimetry (DSC) to understand and analyse the SAS signal [69, 81, 82].

DSC is sensitive to thermodynamic transformations and is hence useful to estimate precipitation kinetics, as the heat signal is proportional to the derivative of precipitate volume fraction [81, 82]. The typical use of DSC is for isochronal study, where the individual peaks can be associated with different structural transformations. And it can be used for multiple precipitates if the precipitation and dissolution peaks can be separated. But one needs to take care during the analysis since complex behaviours can occur under non-isothermal conditions. It is also possible to use DSC under isothermal conditions. To do so, sensitive low-temperature equipment is required, it is thus mostly used on light metals such as Al and Mg alloys where the ageing temperature is relatively low [83].

Up to now, few studies have characterized the precipitation kinetics of rod-shaped precipitates in Mg-Zn system. Jain *et al.* [84] have successfully used TEM to study the precipitation kinetics in a Mg-6Zn alloy aged at 200 ℃. Rosalie *et al*. [69] combined TEM and SAXS to characterise the precipitation kinetics during ageing at 150 ℃ in a Mg-8Zn alloy. The size and volume fraction of rod precipitates are quantitatively investigated in their work, but the authors report significant variations between their TEM and SAXS results. These variations can come from the small volume analysed in TEM and large errors arising from the difficulty in correctly measuring the TEM foil thickness to quantitatively obtain the precipitate volume fraction.

Atom probe tomography (APT) is also commonly used to assess precipitate morphology and compositions. The biggest advantage of APT is that it provides the 3D reconstruction of detailed chemistry information, which makes it reliable to identify the composition transitions within precipitates and solid solution in matrix. A limited number of studies have used APT on Mg alloys [85-88], Honma *et al.* [89] used a three-dimensional atom probe (3DAP) to analyse the chemical structure of precipitates in a Mg-Gd-Y-Zr alloy aged at 200 ℃, it is found that the phase transformation occurs continuously by changing the rare earth composition in the metastable precipitates. In a recent study of Mo *et al.* [85], the presence of Gd–Ca co-clusters was observed for the first time through APT in a solution-treated Mg-Gd-Ca alloy. APT suffers from a number of artefacts such as the different evaporation fields between elements and the effective resolution of the instrument. Similarly to TEM, APT only analyses a small volume and can lack statistical relevance compared to the bulk in terms of precipitation kinetics study.

An alternative way to quantitatively analyse precipitation mechanisms is by using techniques that are sensitive to variations in solid solution such as conductivity and Thermoelectric power (TEP) measurements. TEP measures the change of thermoelectric voltage when there is a temperature gradient across the sample. In metal alloys, the solute atoms are the major factor that influences the TEP result, therefore it is a sensitive tool to follow the precipitation kinetics [90, 91]. This technique has the advantage of requiring minimal sample preparation and data analysis while providing considerable accuracy and giving statistical information on a bulk sample. So far, TEP has been successfully applied to follow precipitation in a range of alloying systems such as steel, Al and Cu alloys [90, 92, 93], but it has not been applied to Mg alloys.

The matrix lattice parameter variation with the presence of solute elements can be measured by XRD [94, 95], the solid solution concentration can then be estimated with the help of known correlation between solute concentration and the change of lattice parameters. A recent study of Filep *et al.* [95] has used this method to test the solute level in Al alloys. While in the case of Mg alloys, alloying additions are shown to have a significant effect on the lattice parameter of Mg matrix, in which Ag and Zn additions have the largest influence [8, 96]. However, one should be careful when using XRD to follow the precipitation kinetics as both the solutes and second phases could have influences on the lattice parameters [97, 98].

2.4.2 Modelling Methods

2.4.2.1 Classical nucleation and growth theories for precipitation

Accurate characterization of precipitation kinetics is needed to validate precipitation models. Those models provide computed evolution of a wide range of parameters such as precipitate size, number density and volume fraction as a function of ageing time and temperature [16, 18, 19, 99, 100]. So far, the most commonly used approach is the mean-field model, usually based on the Kampmann-Wagner-Numerical (KWN) method which couples nucleation, growth and coarsening at the continuum level [16, 99, 101-106], In this model the nucleation rate usually has a classical form [107]:

$$\frac{dN}{dt} = N_0 Z \beta^* \exp\left(-\frac{\Delta G^*}{kT}\right) \qquad (2.5)$$

Where T is the absolute temperature, Z is the Zeldovich factor, ΔG^* is the nucleation energy barrier which can be derived from Eq. (2.2), N_0 is the number of nucleation sites per unit volume, N is the number of precipitates per unit volume, β^* is the frequency at which atoms are added to the critical nucleus and k is the Boltzmann constant.

The growth and coarsening rate of spherical precipitates in a binary system is described by Zener's diffusion-controlled growth solution [20]:

$$\frac{dR}{dt} = \frac{D}{R}\left(\frac{C_m - C_e^R}{C_\beta - C_e^R}\right) \qquad (2.6)$$

Where D is the diffusion coefficient of element in matrix, C_e^R is the solute concentration at the precipitate-matrix interface, C_m is the solute concentration in matrix, R is the precipitate radius and C_β is the solute concentration in precipitate.

The KWN model numerically integrates Eq. (2.5) and Eq. (2.6), in a "multi-class" approach [16, 108], to monitor the full precipitate size distribution. The precipitate size evolution can be described either with a Lagrangian-type approach where, in a precipitate size class, the size of precipitates evolves with time but its proportion remains constant, or an Eulerian-type approach where the proportion of a precipitate class with fixed size changes during growth or dissolution [19, 109]. One significant advantage of these approaches is the relatively smaller computational cost and ease of implementation. It has therefore been adopted in a number of software packages such as PreciSo, MatCalc and PanPrecipitation [19, 109-111].

Up to now, many studies have successfully implemented KWN model to follow the precipitation in Al alloys and steel [101, 112-116]. For example, Myhr *et al*. [101, 113] used a controlled volume KWN method to evaluate the precipitate number density in each size group and establish an ageing strengthening model by introducing the precipitate average strength. Nicolas *et al.* [114] developed a simplified KWN model, in which the composition of precipitates is fixed and the nucleation process is excluded. They predicted the precipitate volume fraction and size distribution in an Al-Zn-Mg alloy. These models have been successful in describing the precipitation kinetics which is used to predict the strength of common Al alloys [116, 117]. Only few studies have attempted to model precipitation kinetics in Mg alloys. In a precipitation study of AZ91 alloy Hutchinson *et al*. [44] developed a model that shows reasonable agreement with experimental data by Cellotto [118], which proposed a plausible explanation for the relatively poor ageing response in some Mg alloys. These prior works treat the nucleation and coarsening as two independent processes, which require different inputs to provide better agreement with experiments. Moreover, the model idealized the chemical free energy and only considered Al diffusivity. Robson [119] later developed a coupled KWN model and successfully predicted the competition between continuous and discontinuous precipitation in an AZ91 alloy. Recently, Zhang *et al.* [103] proposed a similar model which has been adopted in an integrated simulation module of the PANDAT software [111], the simulation results are well validated by experiments in an aged AZ91 alloy [118, 120].

These previous modelling attempts often make the assumptions of spherical precipitates. For the case of non-spherical precipitates, Bardel *et al.* [121] developed a modified KWN model by introducing a shape factor $\xi = \frac{l}{r_p}$, where l is the precipitate length and r_p is the tip diameter, to successfully model the evolution of radius and volume fraction of needle-shaped precipitates in a 6061 alloy. A similar shape factor has been adopted by Chen *et al.* [122] to model the precipitation kinetics of needle-shaped precipitates in a Al-Mg-Si alloy. For the case of rod-shaped precipitates in Mg-Zn alloys, Paliwal *et al.* [123] and Robson *et al.* [124] developed modified KWN models and have been compared with the experimental results from Jain *et al.* [84] and Rosalie *et al.* [69]. These proposed models showed some agreement with experiments but some inconsistencies remained in terms of precipitate volume fraction.

2.4.2.2 Other precipitation modelling methods

Mean-field type models do not consider morphological changes and often the precipitates are required to have constant surface energy and chemical composition. This is not always reasonable. A more sophisticated alternative is using the full-field method, such as phase field simulation, to describe the morphology evolution of precipitates. The phase field simulation considers the anisotropy in micro-elastic strain energy and interfacial kinetics and therefore is useful to study the precipitate growth and coarsening [125-129]. This approach can naturally capture the coarsening of non-spherical precipitates and their interactions with each other. But despite its flexibility, phase field simulation usually requires expensive computational cost, and it cannot simulate nucleation directly, the nucleation is often treated as noise or with a classical form as in Eq. (2.5).

Another interesting method is the atomistic simulation, such as Lattice Kinetic Monte Carlo (LKMC) method [100, 130]. In this model, the precipitates are designed as atomic configurations and evolve through the jumping of atoms between neighbouring sites in a rigid matrix lattice. No assumptions of precipitate morphology and surface energy need to be made as they are included in the bond energy summations. Several studies [131, 132] have successfully modelled the nucleation and growth of precipitates using the LKMC method, but the results are constrained to large supersaturation levels and short ageing times due to the extensive computational requirements.

2.5 Deformation mechanisms in Mg alloys

2.5.1 Crystal structure of Mg

Magnesium shows a typical hexagonal close-packed (HCP) crystal structure, the theoretical stacking sequence of Mg is ABABAB…. Mg has a c/a ratio of 1.624 [133], which is slightly less than the ideal value of 1.633 for HCP metal.

The crystallographic planes and direction in the HCP Mg crystal are represented by the four-index Miller-Bravais notation. In Mg, the close-packed plane and close-packed direction are (0001) basal plane and $\langle 11\bar{2}0\rangle$ respectively. 1/3$\langle 11\bar{2}0\rangle$ is the shortest lattice vector [134]. Some important crystal planes and directions in Mg are presented in Fig. 2.6.

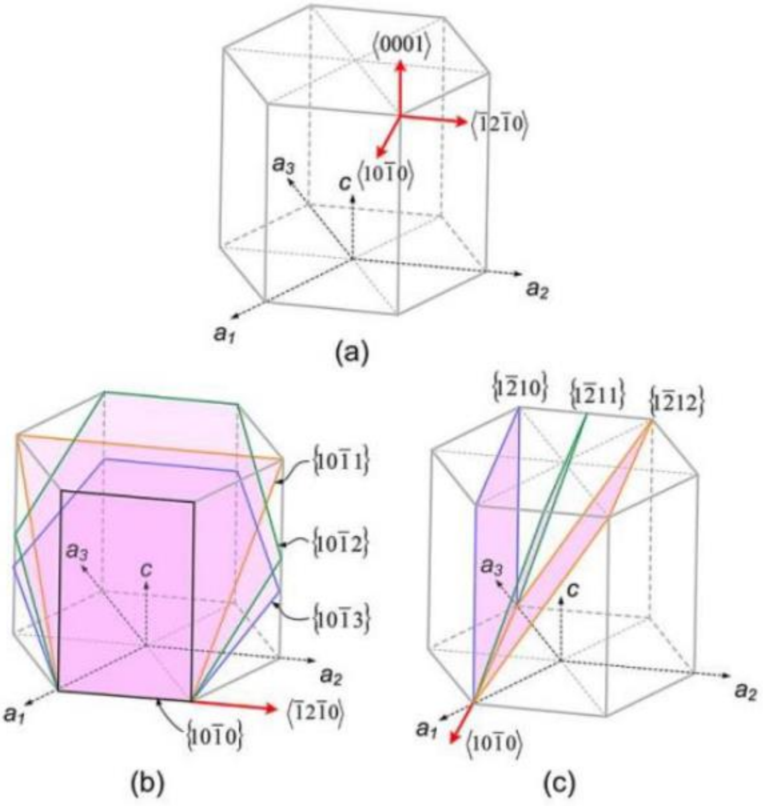

Fig. 2.6 Important crystal planes and directions in the magnesium crystal [135, 136].

2.5.2 Slip in Mg alloys

Slip occurs by the movement of dislocation lines along certain directions and planes. A critical value of stress along the slip directions and planes needs to be reached to initiate slip, it is referred as critical resolved shear stress (CRSS) [137]. The relationship between CRSS and applied stress can be resolved by the Schmid law [138], which for a uniaxial strength state can be expressed as:

$$\tau = \mathrm{m}\sigma \tag{2.7}$$

where σ is the applied stress, τ is critical resolved shear stress and m is the Schmid Factor (SF) which can be represented as:

$$\mathrm{m} = \cos(\phi) \cos(\lambda) \tag{2.8}$$

where λ is the angle between applied stress axis and slip direction, ϕ is the angle between applied stress axis and slip plane.

According to Eq. (2.7), microstructures with high Schmid Factor (SF) for a slip system are easier to reach the CRSS. Theoretically, the highest SF value is 0.5 [139].

2.5.2.1 Slip modes

A slip system represents a set of slip planes and their associated slip directions in the crystal lattice [140]. Due to the HCP structure of Mg having a low symmetry, the number of directions and planes in HCP metals favourably oriented for slip movement is limited. Common slip modes are summarized in Table 2.1.

Basal <a> slip can be easily activated at room temperature since its CRSS is low (~ 0.5 MPa) [141]. However, basal slip can only provide two independent slip systems. On the other hand, prismatic <a> slip can provide two additional slip systems. Pyramidal <a> slip has four independent slip systems but it is usually not treated as an additional slip mode since it can be considered as a combination of basal and prismatic slip modes [142]. None of these < a> type slip modes can deform along the c-axis, therefore pyramidal <$c + a$> slip or twinning is needed.

However, the activation of pyramidal slip requires high applied stress as its CRSS is nearly significantly higher than that for basal slip at room temperature [143, 144].

Therefore, only four independent slip systems are readily activated in Mg alloys (basal and prismatic slip). This is insufficient to meet the Von-Mises criterion [145], where a homogeneous arbitrary deformation requires five independent slip systems. In consideration of this, the importance of twinning in Mg alloy is evident, as it has a relatively low CRSS and provides deformation along the c-axis [146].

Table 2.1 The CRSS values of different slip modes for single crystals in Mg at room temperature.

	Slip plane and direction	Independent slip system provided	CRSS (MPa)
Basal <a>	$\{0001\} < 11\bar{2}0 >$	2	~ 0.5 [141]
Prismatic <a>	$\{10\bar{1}0\} < 11\bar{2}0 >$	2	8 ~ 40 [147-149]
Pyramidal <a>	$\{10\bar{1}1\} < 11\bar{2}0 >$	4	
Pyramidal <$c + a$>	$\{11\bar{2}2\} < 11\bar{2}3 >$	5	~ 40 [150]

2.5.3 Twinning in Mg alloys

Twinning occurs when a lattice structure shears into two symmetrical crystals about a certain twinning plane [151]. It can be produced by simple shuffling of atoms in the twined region, a typical schematic illustration of twin formation is shown in Fig 2.7. In wrought Mg alloys, macroscopic yielding can be related to the onset of prolific tensile twinning [152]. this twinning mode induces the rotation of c-axis by ~86.3° [148, 153]. In textured Mg alloys, twinning causes asymmetry of yield response due to its polarity nature [154], in a sense that twins can only be activated along particular directions.

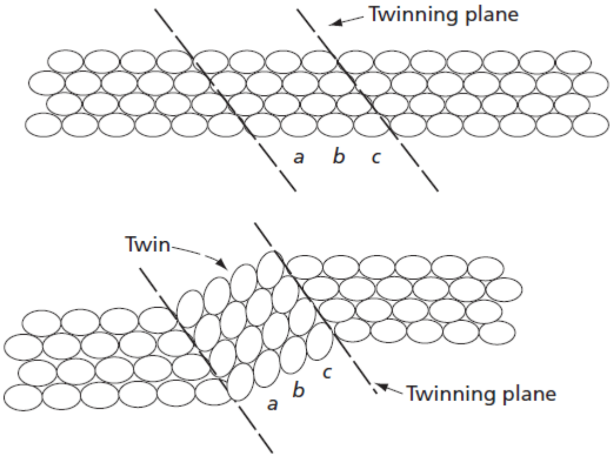

Fig. 2.7 Schematic illustration showing a twin is produced by the simple movement of atoms [155].

2.5.3.1 Twinning geometry

Typical twinning elements are given in Fig. 2.8, where K_1 is the first invariant plane (or shear plane), and K_2 is the second invariant (or conjugate) plane. The plane of shear is given by s. $\eta_1$and η_2 correspond to the shear direction and intersection of K_2 plane and plane of shear. A shear mode is the collection of elements K_1, K_2, η_1 and η_2.

The resolved shear stress on K_1 plane is considered as the driving force for a twin to occur. In Mg alloys, and most HCP metals, the $\{10\bar{1}2\}$ twinning is the most prevalent twinning mode since it has a low CRSS [156].

$\{10\bar{1}2\}$ twinning leads to extension along the c-axis [146]. There are six possible variants of $\{10\bar{1}2\} < \bar{1}011 >$ tensile twinning. Selection of these variants generally follows the Schmid law, in which the system with the higher SF is typically activated [157]. However, it does not mean that systems with lower SFs cannot be selected [158].

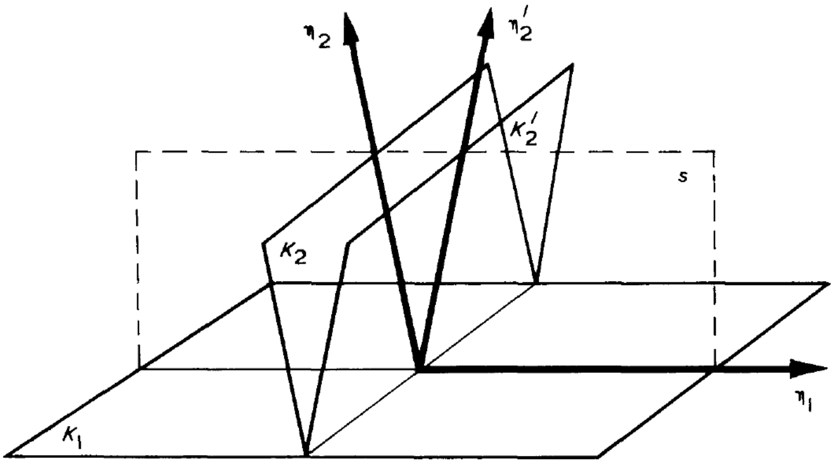

Fig. 2.8 Schematic illustration of twinning elements [159].

2.5.3.2 Twinning process

It is generally believed that twinning comprises three stages [160, 161]: (1) Nucleation, (2) Propagation and (3) Growth (thickening). A Schematic illustration of these stages is presented in Fig. 2.9.

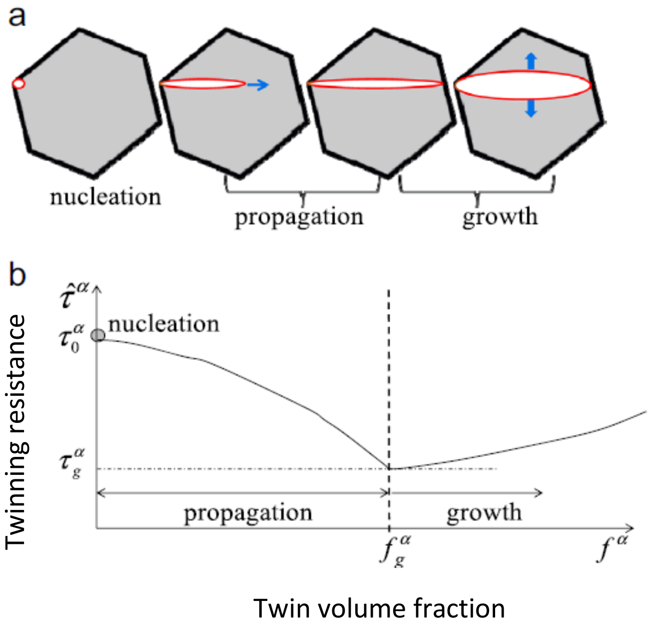

Fig. 2.9 Three stages in the twinning process [162].

Twin nucleation is a stochastic process that is observed to nearly always occur at grain or pre-existing twin boundaries [163]. These regions provide high-stress concentration that facilitates the occurrence of glossily twinning dislocations from the dissociation of perfect dislocations [164-168]. This reaction combined with atomic shuffling leads twins to occur. Twin propagation refers to the lengthening of twins in the twinning plane until they are blocked by grain boundaries or other obstacles (e.g. another twin, precipitate). Twin growth is a thickening process that involves the expansion of twinned area in a direction perpendicular to the K_1 plane [164, 169-171]. It consists of twin propagation (expansion of dislocation loops) and twin thickening (formation of new twin dislocation loops) [169-171]. It is generally believed that twin propagation requires much lower resolved shear stress than that for nucleation [162], thus the propagation and growth after twin nucleation are quick and spontaneous.

The formation of a twin within the matrix causes back stress which impedes the existing twins to further grow. If the back stress becomes too large, the twin will cease to grow as the interior twinning stress falls below the CRSS that is required for the movement of twinning dislocations [172]. This back stress is an important mechanism to be considered in twinning and the observed detwinning (a shrink of twin volume fraction) upon unloading [173, 174]. On the other hand, high stresses occur at twin tips [175, 176]. It triggers slips ahead of the twin tip and produces a plastic deformation zone, which causes plastic relaxation [176].

2.6 Methods for evaluating the CRSS

The CRSS for different deformation modes is traditionally tested through single crystal studies [177]. Here, the CRSS can be measured by applying stresses along different crystallographic directions. Approximate CRSS value measurement can be achieved through deforming the highly textured alloys, by knowing the dominant deformation mechanism along specific orientations [178]. Several other experimental techniques including micropillars [179, 180], nanoindentations [181] and in-situ diffraction methods [45, 182-185] are also applied to estimate the CRSS. However, micropillars and the indentation-based approach suffer from size effects [179-181].

Simulation is another way to estimate CRSS values. Barnett *et al.* [186] proposed a value of 32 MPa as the CRSS for tensile twinning through a Taylor approach. Agnew *et al.*

[187] conducted Visco-Plastic Self-Consistent (VPSC) simulation for the deformation of a Mg-Li alloy, the twinning CRSS value is found to be 15 MPa. However, both Taylor and VPSC methods cannot determine the microplasticity (stress below microscopic yielding) as they are based on fitting macroscopic stress-strain curves using a set of parameters. Elasto-Plastic Self-Consistent models (EPSC) [152, 188] were therefore developed to address the lattice strain evolution in soft and hard oriented grains that are not resolved by the two aforementioned models. Several studies have applied this approach to determine the CRSS values for different deformation modes in wrought Mg alloys in conjunction with diffraction analysis [189-191].

2.7 Impact of precipitates on deformation modes in Mg alloys

2.7.1 Interactions between precipitates and slip

Mg alloys have a relatively low age hardening response when compared to Aluminium alloys, this is partly due to the precipitate number density in Mg alloys, which is unusually low [192]. Clark *et al.* [40] investigated the ageing response of a Mg-9Al alloy, and found that the basal plates formed in this alloy can poorly harden basal slip. A similar point was made by Gharghouri *et al.* [193] in a study on an aged Mg-7.7Al alloy. Prismatic plates, on the other hand, show excellent resistance to basal slip [194]. Celloto *et al.* [192] investigated the continuous precipitates with different morphologies in AZ91 alloy including the rod and plate-shaped precipitates with different orientations. Results show that the long lath-shaped precipitates after ageing at 100 ^{o}C for around a year produce the strongest hardening effect.

Efforts have then been made to elucidate the age-hardening response through measuring the CRSS increment of slip systems caused by precipitates. Basal plates in Mg-Al alloy are found to increase the CRSS for basal slip by 5 MPa (13%) and the CRSS for prismatic slip by 25 MPa (40%) [190]. Stanford *et al.* [195] used VPSC simulation to show that the CRSS for prismatic slip increases from 54 MPa to 140 MPa by the presence of *c*-axis rod-shaped precipitates in an aged Mg-5Zn alloy. The effective hardening of prismatic slip by rod-shaped precipitates has also been reported by Jain *et al.* [196] through TEM observations. Recently, Wang *et al.* [197] suggested that the rod-shaped precipitates in an aged Mg-5Zn alloy also produce a moderate increase of CRSS for basal slip of 17 MPa

(33%), according to the micropillar compression results. Agnew *et al.* [198] using in-situ neutron diffraction and EPSC modelling found that the prismatic plates in Mg-RE alloy increased the CRSS for basal slip from 12 MPa to 37 MPa, i.e. an increment of over 200%, while the CRSS for prismatic slip increased by 18%, from 78 MPa to 92 MPa.

Normally, two possible interaction mechanisms between precipitates and slip are considered [7, 199, 200]: (a) dislocations bypass precipitates via the Orowan mechanism and (b) dislocation shears through precipitates. In Mg alloys, since most strengthening precipitates are either too large or incoherent to be sheared, the former is considered as dominating mechanism [17]. The stress required to pass through the obstacles for a dislocation line can be expressed as [201, 202]:

$$\Delta\tau = \frac{\bar{F}}{b\bar{L}} \qquad (2.9)$$

Where $\bar{L}$ is the average particle spacing, $\bar{F}$ is the force acting on precipitate and b is the Burgers vector.

And the Orowan bypass equation is given by [7, 17]:

$$\Delta\tau = \frac{Gb}{2\pi\bar{L}\sqrt{1-v}} \ln\frac{d_p}{r_0} \qquad (2.10)$$

Where r_0 is the core radius of dislocations, v represents the Poisson's ratio, $\Delta\tau$ is the CRSS increment, G is the shear modulus of the matrix phase and d_p is the mean planar diameter of the particles.

The classical Orowan equation is usually used to predict strengthening from spherical particles. But due to the unique morphology of precipitates in Mg alloys, a modified Orowan equation has been applied by Nie [9] and Robson *et al.* [10] to calculate the hardening effect of precipitates with different geometries on basal and prismatic slips. It is demonstrated that (a) prismatic plate has a more significant strengthening effect on basal slip than basal plate and rod-shaped precipitates, (b) the strengthening of prismatic slip decreases in the order of c-axis rods, basal plates and prismatic plates, (c) the rod-shaped precipitates have a good hardening effect on both slip systems, such effect decreases when the precipitate size enhances. These predictions have been confirmed by recent Transmission Electron Microscopy (TEM) and in-situ diffraction studies [45, 84] and agree well with the above CRSS estimations [190, 195-198]. In another study by Wang *et al.* [203] through modified Orowan calculation, prismatic plates are indicated to have a better hardening effect on the prismatic $<c+a>$ slip system. rod-shaped precipitates only show a strong hardening effect when the volume fraction of prismatic plates is below 4%.

It is still unclear regarding the shearing mechanism of precipitates in Mg alloys. Recently, shearing of thin prismatic plates and rod-shaped precipitates by the basal slip in Mg alloys have been shown by TEM [197, 204-206], but the reported results are mostly based on single-crystal micropillar experiments where the shearing force can be significantly larger than the cases of polycrystals. Bhattacharyya *et al.* [205] have developed an order strengthening model and predict that the shearing resistance of precipitates may be related to the formation of anti-phase boundaries (APB) within precipitates. The APB energy for basal slip is estimated to be $210\,\mathrm{mJ/m^2}$ in this study, high enough to account for the observed shearing. Bardel *et al.* [121] have developed a coupled strength model based on Orowan theories to predict the yield strength in a 6061 Al alloy by taking into account both shearing and bypassing mechanisms for needle-shaped precipitates, where the strength increment caused by shearing can be evaluated by considering the force acting on a dislocation line and the area swept by the moving dislocation.

2.7.2 Interactions between precipitates and twinning

Clark *et al.* [46] first reported the influence of precipitates on twinning in a Mg-5Zn alloy in 1965, the results show that precipitates can be sheared by $\{10\bar{1}2\}$ twins instead of slip dislocations. Shearing of the precipitates by twins has also been observed in Mg-Gd-Zn and Mg-Zn-Y alloys [207, 208]. Such shearing usually occurs when precipitates are thin (< 20 nm) and coherent with the matrix. In most cases, however, twins do not produce shearing of precipitates [190, 195, 209]. Instead, the rod-shaped precipitates in Mg-Zn alloy undergo a rigid body rotation of ~ 4° as it interacts with a twin [46, 195, 210]. In a study of Mg-Al alloy by Stanford *et al.* [190], precipitates are found to be slightly bent little and partially embedded in a twinned area. In this case, the rigid body rotation is unlikely to happen as part of the stiffer precipitate remains in the parent matrix (See Fig. 2.10), leading to a misfit strain. Gharghouri *et al*. [193] found that twins can either engulf, arrest at the precipitates or even bypass precipitates depending on their size differences. They also suggest that when a precipitate is fully engulfed by the twin, it also undergoes rigid body rotation that could relax part of the strain misfit, which is evidenced by the observed dislocations at twin-precipitate interfaces. Recently, Robson *et al.* [211] using Eshelby methods studied the misfit strain caused by different precipitate types. The results showed that the prismatic plate causes the greatest strain misfit, followed by basal plates, and the strain misfit caused by prismatic rods is the lowest. But since this calculation simplified the situation as purely elastic, the predicted misfit strains are usually large. Liu *et al.* [212] using full-field simulation showed that the misfit strains are highest at (1) the tips of precipitates and (2) the contact point between twin boundary and precipitates. The best strengthening effect is provided by the precipitates whose habit planes are parallel to the twinning plane.

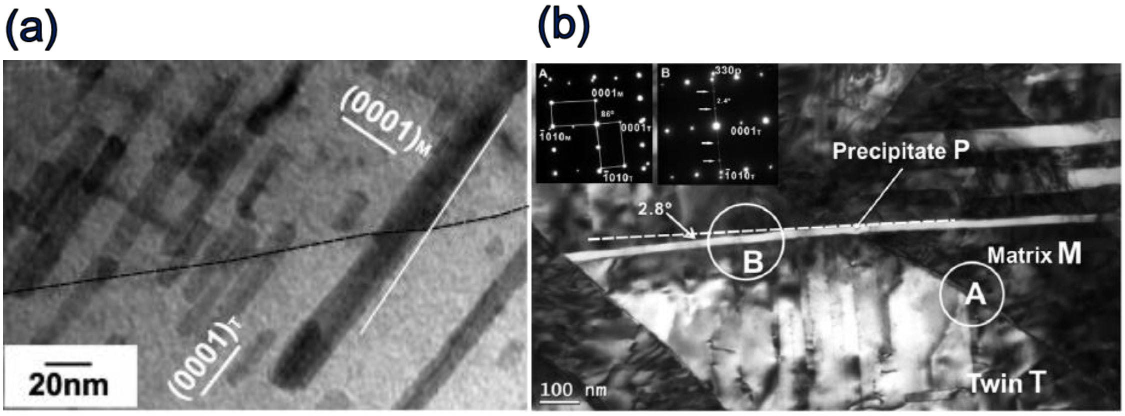

Fig. 2.10 Interaction of a $\{10\bar{1}2\}$ twin and precipitates in (a) Z5, precipitates show a rigid body rotation [210] and (b) AZ91, precipitates bend and partially embedded in the twinned region [190].

It is also interesting to compare the twin volume fractions before and after ageing. For Mg-Zn alloy, the twin volume fraction does not seem to be changed by the rod-shaped precipitates [46, 213]. Nevertheless, Stanford *et al.* [195] observed that the total volume fraction in aged Mg-5Zn alloy decreased a little after 5% compression strain. Through in-situ neutron diffraction, Agnew et al. [45] found that the twin volume fraction increased with the presence of prismatic plates in an aged Mg-Y-Nb-Zr alloy. While the twin volume fraction against plastic strain in AZ series alloys shows no change [214] or slightly decreased [185, 209]. Though there is no consistent conclusion in the literature about the influence of precipitates on the twin volume fraction, it is commonly observed that the twin number density is increased and accompanied by a simultaneous decrease of twin aspect ratio with the presence of precipitates. Such a case has been reported by

Standford *et al.* [195], Robson *et al.* [215] and Wang *et al.* [216] in aged Mg-Zn alloy, and has also been found in Mg-Al alloys [209]. This has been rationalized by the fact that precipitates are likely to suppress the twin growth process while having little influence on nucleation, as a result, twining response inclines to more nucleation and less thickening [215]. This assumption has recently further been elucidated by Wang et al. [197, 217] through micropillar compression tests, the twin growth stress in a peak-aged Mg-5Zn alloy is reported hardened by ~ 30MPa while the influence of precipitates on the stress for nucleation is negligible.

Precipitates are known to influence yield asymmetry in Mg alloys. Specifically, precipitates in Mg-Al alloys can decrease the yield asymmetry [209], while in Mg-Zn alloys the yield asymmetry increases with the presence of precipitates [195]. Robson *et al.* [10] suggested that the change of yield asymmetry of strongly textured Mg alloys is determined by the CRSS difference between prismatic slip and twinning in the presence of precipitates.

Table 2.2 summarizes some example studies that calculated the CRSS increment for twinning caused by precipitates. The case of prismatic plates in Mg-RE alloys are not included due to the strong influence of rare earth element on twinning and their CRSSs for different slip modes are relatively close, it is therefore hard to reliably quantify the threshold for twinning in these systems [45]. It is shown that the strengthening increment for twinning is comparable to the precipitation hardening against slip [84, 213], but there is a considerable scatter between different studies of CRSS increment, this could be because different methods were used in determining the onset of twinning. Besides, the CRSS increment for twinning is also affected by ageing conditions [213].

The Orowan equation has been applied to study precipitate strengthening against twinning [9, 10], where the twin partial dislocation is treated in the same way as a lattice slip dislocation. However, since the Burgers vector of twinning dislocations is much smaller than that of slip, the predicted Orowan hardening from Eq. (2.10) is typically smaller than the experimentally observed CRSS values reported [10, 190, 195, 213, 218], as can be seen in Table 2.2. Alternatively, the long-range back-stress method was applied to predict the observed strengthening increment [10, 211, 213]. This is based on the volume fraction of precipitates and the subsequent strain incompatibility produced at the precipitate-twin interface. [185, 219]. By using Eshelby stress tensor, the misfit strain and related back stress calculated for AZ91 alloy are ~ 6.5% and 1600 MPa [40, 211]. This high value substantially overestimated the strengthening effect of precipitates on twinning. On the other hand, in the case of Mg-Zn alloy, the back stress approach seems to provide a reasonable estimate for the observed strengthening [213]. However, this back stress is very hard to be accurately calculated as it will be reduced by plastic relaxation processes [176].

Table 2.2 Estimated increment of critical resolved shear stress for $\{10\bar{1}2\}$ twinning in peak-aged alloys

Alloy	Precipitate type	Processing	Method	Measured CRSS increment, MPa	Orowan prediction, MPa	Reference
Z5	c-axis rods	Extruded	VPSC	62	10	[195]
Z6	c-axis rods	Extruded	VPSC	29	10	[213]
Z5	c-axis rods	Single crystal	Micropillar compression	30		[217]
AZ91	basal plates	Rolled	Schmid Factor	21	5	[190]
AZ91	basal plates	Rolled	Schmid Factor	36		[185]
AZ91	discontinuous precipitates	Extruded	Schmid Factor	50		[214]

Recently, Barnett *et al.* [220] proposed a double super dislocation model for the propagation of twins based on Orowan theory, where the movement of twin tip consists of a set of twin partials, the leading dislocation is “pushed” by trailing super dislocation to bypass the particles, as shown in Fig. 2.11.

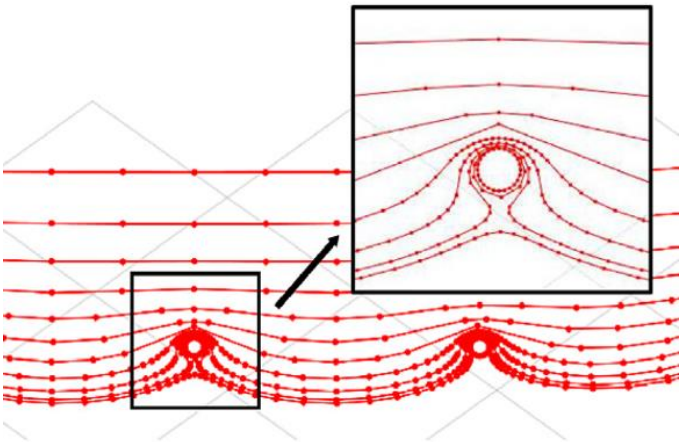

Fig. 2.11 Simulation results of interaction between obstacle and twin dislocations [220]. The leading dislocations are pushed by the trailing dislocations to bypass the obstacle.

In this model, the classical Eq. (2.10) has been modified to [220]:

$$\Delta\tau = \frac{\tau_0 G(n'b)^2}{2\pi\sqrt{1-v}2\gamma L}\ln\left(\frac{\bar{D}}{n'b}\right) \qquad (2.11)$$

Where τ_0 is the obstacle-free reference propagation stress which has a form as $\tau_0 = \frac{2\gamma}{nb}$, 2γ is the coherent twin interface energy, L is the effective precipitate spacing, $\bar{D}$ is the harmonic mean of precipitate length l and particle diameter d, which is given by $2/(l^{-1}+d^{-1})$, $n'b$ is the magnitude of leading super dislocation burgers vector,

According to the model, the twin propagation stress reasonably predicts the observed CRSS increment in a Mg-6Zn alloy [213, 220].

2.8 Gaps in the literature and scope of present work

To help control the formation of β_1' precipitates, and therefore benefit the design of high-performance Mg-Zn alloys, efforts have been exerted to understand the evolution of this precipitate during ageing [64, 65, 67, 68, 70]. However, current precipitation models have not been readily applied in the Mg-Zn system. Though the growth kinetics has been experimentally examined by Jain *et al*. [196] and Rosalie *et al*. [69], their results show inconsistency between techniques and modelling [123, 124]. The asymmetrical nature of precipitates in Mg-Zn alloys and the complexity of precipitate compositions makes it challenging to accurately characterize and describe precipitation kinetics in these alloys.

As a result, the details of precipitation processes and driving forces for the formation of rod-shaped precipitates at different ageing conditions are still unclear. To help better understand precipitation processes in Mg-Zn alloys, we analysed the precipitation kinetics of rod and plate-shaped precipitates in a Mg-Zn alloy using multi-characterization (TEP, TEM, XRD and APT) to compensate limitations of each technique. Modified KWN models for rod and plate-shaped precipitates are also proposed to support the experimental results by giving a detailed view from thermodynamics aspects.

Precipitation strengthening on slip has been a long-standing topic in metallurgy and thoroughly examined by experiment and modelling [9, 10, 40, 192-194]. However, in most studies, models are only developed for spherical precipitates, and the shearing mechanism has not been readily considered. Nie [9] and Robson *et al.* [10] discussed different particle shapes in the Orowan mechanism, but the importance of influence of different particle arrangements on slip planes is still unclear. Consequently, precipitation strengthening in Mg-Zn alloys with rod-shaped precipitates has not been well described. Also, little studies have tried to correspond the strength model to the precipitation kinetics. To address those issues, the current study develops a strength model based on Orowan theory and coupled with the precipitation kinetics model to predict strength evolution during ageing in Mg-Zn alloy.

Precipitates also have profound effects on twinning behaviour [10, 195, 209, 215], and further influence the mechanical properties of the material such as yield asymmetry [195]. This shows there is a great potential to control twinning in Mg-Zn alloys through changing the precipitate type, size and volume fraction. But the change of twin volume fraction in aged Mg-Zn alloys has not been well represented [46, 195, 213], and there is a lack of quantitative and systematic comparison of twinning behaviour between different ageing conditions (where precipitates distributions and solute concentrations differ significantly). On the other hand, progress has been made in developing models predicting precipitation hardening on twinning plane [176, 220], but there are still difficulties in relating precipitation evolution with the resultant mechanical properties. In this thesis, the twin super dislocation model is coupled with a precipitation model to predict the strengthening of twinning plane during ageing. A quantitative analysis of twinning behaviour with the presence of precipitates in bulk area will also be discussed in detail using Electron backscatter diffraction (EBSD) technology.

Overall, this thesis is dedicated to answering the following questions:

1. How ageing affects the number density, size and volume fraction of strengthening precipitates in Mg-Zn alloys and how can this be modelled mathematically as a function of ageing time and temperature?
2. How the evolution of precipitates during ageing in Mg-Zn alloys effects hardening on basal and prismatic planes and how to model the relevant strengthening mechanisms?
3. How does the precipitation in Mg-Zn alloys impact hardening on twinning plane and how the dispersion of precipitates influences the twin volume fraction, twin aspect ratio and twin number density?

3. Methodology

This chapter describes the materials and experimental methods, including characterization techniques and mechanical tests, used in the current study. Detailed introduction of modelling principles are also presented.

3.1 Alloy preparation

The material used in this study is extruded Mg - 4.5 wt.% Zn alloy and no grain refining Zr was used. This composition is selected to obtain a considerable precipitate volume fraction after heat treatment, while a Zn level higher than 4.5 wt% may lead to unstable solid solution and Zn clustering [49]. The cast Mg - 4.5 wt% Zn was solution treated at 330 ℃ for 24 h and 370 ℃ for 120 h, followed by extrusion at 350 °C with a reduction ratio of ~ 36 and ram speed of 0.1 mm/s.

In order to consider the solute loss due to ageing, reference alloys are obtained following the same procedures with Zn concentrations of ~ 1.9 wt.% and ~ 2.8 wt.%. The Mg-Zn phase diagram in PANDAT software is used to calculate the reference compositions, in which 1.9wt.% and 2.8wt.% Zn correspond to the respective maximum solubilities of Zn in Mg at the temperatures of 150 ℃ and 200 ℃ after reaching equilibrium. However, this is a rough estimate since the studied phases are meta-equilibrium in the current study

3.2 Isothermal ageing

Two groups of samples were prepared for the ageing treatment: extruded sample without solution treatment and sample solution treated at 370 ℃ for 6 h and 12 h. Isothermal ageing was then performed at 150 ℃ and 200 ℃ using silicon oil bath, all samples were quenched in water at ambient temperature after ageing. Note that the reference sample Mg-1.9Zn and Mg-2.8Zn follow the same solution treatment.

3.3 Mechanical testing

3.3.1 Hardness test

The hardness of samples with various ageing conditions was measured using Vickers micro-hardness measurements and the surface of samples was mechanically polished up to 4000 SiC grit paper before testing. A load of 300 g and a holding time of 20 s were used for the measurements, the reported value is an average of at least 8 different indentations.

3.3.2 Tensile and compression tests

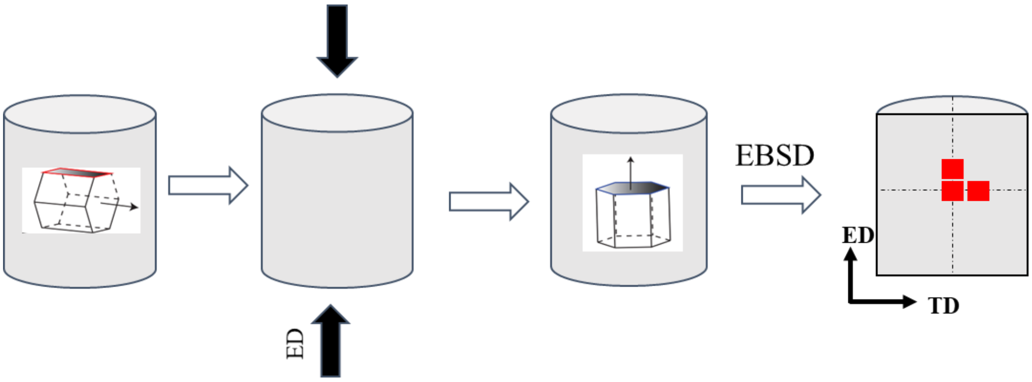

Fig. 3.1 Sample preparation process for EBSD

Fig. 3.1 shows the schematic representation of the section where EBSD measurements were carried out. Cylinder samples for compression test and tensile samples were cut from the centre of the extruded and aged material. The compression sample has a height of 6 mm and a diameter of 4 mm, the gauge size of tensile sample is present in Fig. 3.2. Compression and tensile tests were carried out using a universal INSTRON machine, with a compression strain rate of 2×10^{-4} s^{-1} and tension strain rate of 1×10^{-3} s^{-1}, in a direction parallel to the extrusion direction (ED) so that the $\{10\bar{1}2\}$ twinning dominates the compression stress-strain behaviour and prismatic slip dominates tensile stress-strain behaviour.

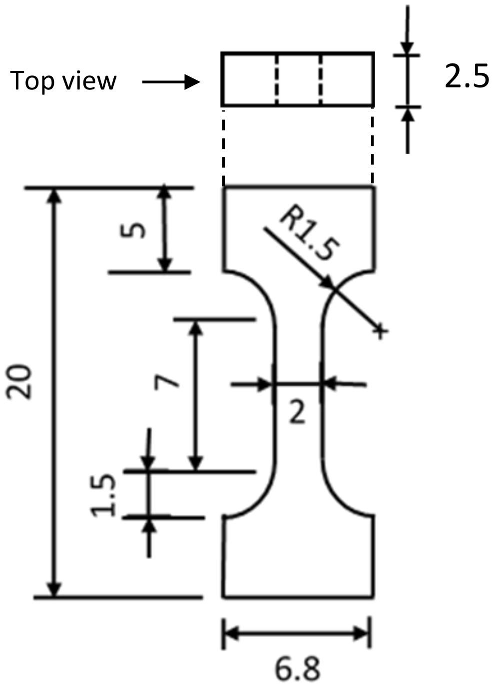

Fig. 3.2 Schematic illustration of tensile sample used for the study, the unit is mm.

3.4 Microscopy

3.4.1 Transmission Electron Microscopy (TEM) observation

Foils for TEM observation were machined from the centre of aged samples with a thickness of 0.5-1 mm and manually ground to ~ 120 μm with 1200 grit SiC paper then to ~ 60 μm with 4000 SiC paper. 3 mm discs were punched from these thin foils using GATAN PIPS (precision ion polishing system) to make a hole through their centre. The TEM observations were performed using JEOL 2100 FEG TEM.

The size of rod and plate-shaped precipitates was measured by observing them perpendicular to the c-axis of Mg matrix. To distinguish overlapped particles, multiple TEM images with high magnification were taken and compounded together to cover a large area, each condition is supported with at least 300 measured precipitates. The average aspect ratio is calculated from the measured aspect ratio of all individual particles. The number density of precipitates was obtained by counting the number of particles in a specific area with known average thickness, where the foil thickness was estimated through the electron energy loss spectroscopy (EELS) technique with the assisted calibration from convergent beam electron diffraction (CBED) technique. The volume fraction of rod and plate-shaped precipitates was estimated by considering the average precipitate size and their number density.

Mahmoud Reza Ghandehari Ferdowsi is acknowledged for performing the TEM measurements. The author contributed to the result analysis.

3.4.2 Electron-backscattering Diffraction (EBSD) observation

EBSD measurements were carried out to investigate the twin area fraction and evolution of twin morphological parameters. Observation of plane parallel to the compression direction is conducted using a LEO 1530 SEM equipped with HKL Technology Flamenco data collection software. Samples for EBSD study were grounded to 200, 600 and 1200 grit, followed by polishing using colloidal diamond suspension. Finally, the samples were polished using colloidal silica solution. The aperture size used for the scan was 60 μm. The accelerating voltage is 20 keV and the working distance is 10-12 mm. The step size for undeformed and deformed samples is 2 μm and 0.25 μm, respectively.

Jun Wang and Mahmoud Reza Ghandehari Ferdowsi are acknowledged for performing the EBSD measurements. The author contributed to the result analysis.

3.5 TEP measurement

Samples from all groups before and during ageing process were prepared for TEP measurement has a gauge size of 75 mm × 5 mm × 1.5 mm. TEP measures the voltage (V) arising from the Seebeck effect between the two junctions of studied material which are attached to a reference pure metal (here pure Cu was used) [90]. During the measurements, a temperature gradient (ΔT) at the junctions is established. In the current study, the temperature of the blocks used was T and T+ΔT with T = 15 ℃ and ΔT = 10 ℃. The relative TEP is defined as:

$$S = S^{*} - S^{*}_{Cu} = V/\Delta T \quad (3.1)$$

Where S^{*} is the absolute TEP of the studied alloy and S^{*}_{Cu} is the TEP of pure Cu.

The absolute TEP S^{*} is affected by the defects present in the Mg matrix, it can be represented as:

$$S^* = S_0^* + \Delta S_{SS} + \Delta S_d + \Delta S_{pp} \quad (3.2)$$

Where S_0^* is the TEP of pure metal without defects. ΔS_{SS}, ΔS_d and ΔS_{pp} are TEP values induced by solid solution (ss), dislocation (d) and precipitates (pp).

The contribution of solute element Zn (concentration $[\mathrm{Zn}]_{wt\%}$) on TEP ΔS_{SS} is given by the Gorter–Nordheim law [221]:

$$\rho\Delta S_{ss} = (\rho_0 + \alpha_{\mathrm{Zn}}[\mathrm{Zn}]_{wt\%})\Delta S_{SS} = \alpha_{\mathrm{Zn}} S_{\mathrm{Zn}} [\mathrm{Zn}]_{wt\%} \quad (3.3)$$

Where ρ is the resistivity of alloy, ρ_0 is the resistivity of pure Mg, α_{Zn} is the specific resistivity of Zn in Mg and S_{Zn} is the specific thermoelectric power of Zn in Mg.

As far as precipitates are concerned, small coherent or semi-coherent precipitates are likely to have an intrinsic effect, depending on their shape, size and volume fraction. While the influence of large incoherent precipitates is negligible [90-93]. Dislocations can also have minor influences on the TEP. For example, in Fe alloys, the increased dislocation density was shown to result in a decrease of TEP value [91]. In the current study, the effect of dislocations is neglected and the precipitates are large enough that their effect on the TEP will be minimal [90-93]. Assuming only solute atom variations influence TEP ($\Delta S_d = \Delta S_{pp} = 0$), the Gorter–Nordheim law can be applied to estimate the solute variations [221]:

$$\Delta S_{SS} = S - S_0 = \frac{\alpha_{Zn} S_{Zn} [\mathrm{Zn}]_{wt\%}}{\rho_0 + \alpha_{\mathrm{Zn}}[\mathrm{Zn}]_{wt\%}} \quad (3.4)$$

Where S_0 is the relative TEP of pure Mg.

Eq. (3.4) can also be written as:

$$\frac{1}{\Delta S_{SS}} = \frac{A}{[Zn]_{wt\%}} + B, \text{ where } A = \frac{\rho_0}{\alpha_{Zn} S_{Zn}}, \; B = \frac{1}{S_{Zn}} \quad (3.5)$$

Where A and B are constant in this equation that can be determined by conducting a linear fit of $1/\Delta Sss$ against $1/[\mathrm{Zn}]_{\mathrm{wt\%}}$.

3.6 XRD measurement

X-ray diffraction measurements are carried out to quantify the concentration of solute elements in Magnesium matrix. The measurements were performed in the powder diffraction beamline at Australian synchrotron using a monochromatic beam of 21 keV (wavelength of 0.58998 A^o) and with a spot size of 4 x 1.2 mm^2 incident on the sample at 90^o angle [222]. Samples of 1 mm thick were cut into thin pillars with the pillar's long axis along the extrusion direction. These pillars were rotated continuously to compensate the orientation effects and to improve the grain sampling statistics. The diffraction profiles were analysed using TOPAS software suite [223] to evaluate the lattice parameters. The diffraction profiles were calibrated using a scan performed on Lanthanum-hexaboride (LaB6) sample using the same conditions as the sample.

Sitarama R. Kada is acknowledged for performing the XRD measurements. The author contributed to the sample preparation and result analysis.

3.7 APT measurement

APT samples were prepared by standard two-step electropolishing at room temperature. The APT experiments were carried out for samples peak-aged at 150 ℃ and 200 ℃ using a Local Electrode Atom Probe (LEAP 5000XR) instrument (CAMECA Instrument, USA), operated in voltage mode at a pulse rate of 200 kHz and a pulse fraction of 20%. The temperature was controlled at 60 K and the detection rate was 0.5%. The APT data were reconstructed and analysed using the CAMECA Integrated Visualization and Analysis Software (IVAS) version 3.8.2 software.

Lu Jiang is acknowledged for performing the APT measurements. The author contributed to the sample preparation.

3.8 Modelling

3.8.1 Precipitation model

The classical nucleation, growth and coarsening theories are adopted in this work which provides predictions of precipitation kinetics during various heating processes and are fully described in [99]. The precipitation state was characterized by a precipitation model tailored for rod and plate-shaped precipitates in Mg-Zn system and the strategy is based on the precipitation model proposed by Perez *et al*. [18, 19], and modified by Bardel *et al*. [121] and Balan *et al*. [224], which is briefly revisited below.

The current model uses “mean field multi-class approach” (Lagrange-like approach), which is based on the following assumptions:

- The nucleation is homogeneous and elastic energy is assumed to be negligible.
- The interfacial energy and chemical composition of precipitates are considered constant and do not vary with precipitate size, time or temperature.
- The rod-shaped precipitates are assumed to be equivalent to a cylinder of length $l - 2r_r$ and radius r_r, the plate-shaped precipitates are assumed as plates of thickness h and radius r_p (see Fig. 3.3).
- The shape factors for rods $b_r = l/r_r$ and plates $b_p = 2r_p/h$ are considered constant as determined by the average value from TEM.

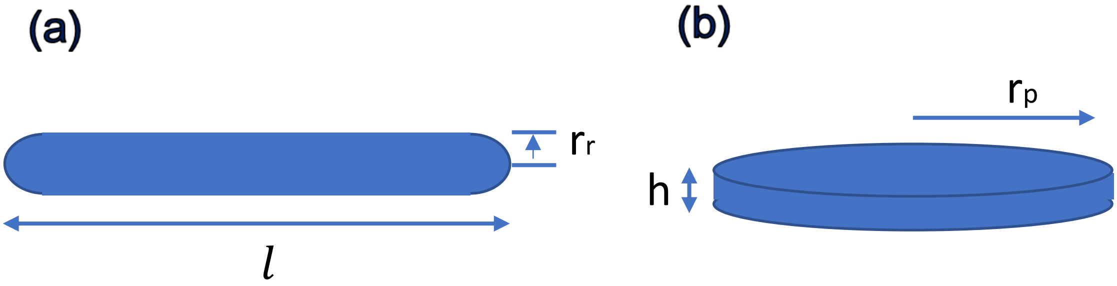

Fig. 3.3 Schematic illustration of (a) rod precipitate and (b) plate precipitate in the precipitation model.

The classical nucleation theory represents the competition between volume energy and surface energy, and the total Gibbs energy change ΔG with the presence of rod and plate-shaped precipitates can be written as:

For rod [121]: $\Delta G = \left(b_r - \frac{2}{3}\right)\pi r_r^3 \Delta g + b_r 2\pi r_r^2 \gamma$ (3.6)

For plate [224]: $\Delta G = \frac{2}{b_p}\pi r_p^3 \Delta g + (1 + \frac{2}{b_p}) 2\pi r_p^2 \gamma$ (3.7)

Where Δg is the chemical driving force which has a negative contribution to the energy change, and γ is the surface energy.

The critical radius r_r^* can then be modified as:

For rod [121]: $r_r^* = -\frac{2\gamma}{(-)\Delta g}\frac{2b_r}{3b_r-2}$ (3.8)

For plate [224]: $r_p^* = -\frac{2\gamma}{(-)\Delta g}\frac{b_p+2}{3}$ (3.9)

So the energy barrier for nucleation becomes:

For rod [121]: $\Delta G^* = \frac{16}{3}\pi\frac{\gamma^3}{\Delta g^2}\frac{2b_r^3}{(3b_r-2)^2}$ (3.10)

For plate [224]: $\Delta G^* = \frac{16}{3}\pi\frac{\gamma^3}{\Delta g^2}\frac{(b_p+2)^3}{18b_p}$ (3.11)

The classical nucleation rate for rod and plate-shaped precipitates is given by [18, 19]:

$$\frac{dN}{dt} = N_0 Z\beta^* \exp\left[-\frac{\Delta G^*}{k_b T}\right][1-\exp\left(-\frac{t}{\tau}\right)] \qquad (3.12)$$

Where t is the ageing time, τ is the incubation time, T is the temperature (in kelvin), k_b is the Boltzmann constant, N_0 is the nucleation site density, the current study considers homogeneous nucleation where every atom of the matrix is a possible nucleation site, then $N_0 = \frac{1}{v_{at}^m}$, where v_{at}^m is the atomic volume of the matrix. β^* is the condensation rate and Z is the Zeldovich factor. For rod precipitates, Z and β^* are given by [121]:

$$Z = \frac{v_{at}^p}{\pi r_r^{*2}(3b_r-2)}\sqrt{\frac{2b_r\gamma}{k_b T}} \qquad (3.13)$$

$$\beta^* = \frac{4\pi r_r^{*2}}{a^4}\left(\frac{X_{Zn}^p}{D_{Zn}X_{Zn}}\right) \qquad (3.14)$$

For plate precipitates, they are [224]:

$$Z = \frac{v_{at}^p}{3\pi r_p^{*2}}\sqrt{\frac{(b_p^2+2b_p)\gamma}{2k_b T}} \qquad (3.15)$$

$$\beta^* = \frac{4\pi r_p^{*2}}{a^4}\left(\frac{X_{Zn}^p}{D_{Zn}X_{Zn}}\right) \qquad (3.16)$$

Where v_{at}^p is the atomic volume of precipitate, a is the lattice parameter, D_{Zn} is the Zn diffusion coefficient. D_{Zn} can be expressed as [18, 19]:

$D_{Zn} = D_{Zn}^{0} \exp\left[-\frac{Q_{Zn}}{RT}\right]$ (3.17)

The growth equation is using Zener-Hillert expression adapted for rod and plate-shaped precipitate:

For rod [121]: $\frac{dl}{dt} = 1.5\frac{D_{Zn}}{2r_r}\frac{X_{Zn}-X_{Zn}^{i}}{\alpha X_{Zn}^{p}-X_{Zn}^{i}}$ (3.18)

For plate [224]: $\frac{dl}{dt} = 0.5b_p\frac{D_{Zn}}{r_p}\frac{X_{Zn}-X_{Zn}^{i}}{\alpha X_{Zn}^{p}-X_{Zn}^{i}}$ (3.19)

Where X_{Zn}^{i} is the Zn atomic fraction at interface.

The multiplicative term $1 - r^{*}/r$ in the original Zener-Hillert expression which accounts for capillarity effects is removed here because the Gibbs–Thomson effect is more efficiently accounted for in the current model [21, 121].

The solubility product of precipitates is expressed in a classical form:

$\log_{10} K_S = -\frac{A}{T} + B$ (3.20)

Where A and B are parameters that need to be evaluated from the experimental solubility limit.

At each time step, K_s for the precipitate with composition Mg_xZn_y is evaluated as:

$K_S = X_{\mathrm{Mg}}{}^{x} X_{\mathrm{Zn}}{}^{y}$ (3.21)

Finally, the mass balance is calculated to update the solute content as precipitation proceeds, it can be expressed as:

$X_{Zn} = \frac{X_{Zn}^{0} - \alpha X_{Zn}^{p} f_v}{1 - \alpha f_v}$ (3.22)

Where f_v is the volume fraction of precipitates at each time step, it can be easily calculated by knowing the radius and number density of all modelled classes i. α is the ratio of atomic volumes between Mg matrix and precipitates, X_{Zn}^{0} is the initial atomic fraction of Zn in solid solution, X_{Zn} is the atomic fraction of Zn in solid solution at each time step, X_{Zn}^{p} is the atomic fraction of Zn in the precipitates.

3.8.2 Precipitate strengthening model

Models based on interactions between dislocations and microstructure are used to study the precipitation strengthening on slip and twinning, their principles are briefly revisited below.

3.8.2.1 Precipitate strengthening model for slip

3.8.2.1.1 Force acting on precipitates

The classical formulations proposed by Friedel [225] and improved by Kocks [201] and Deschamps [202] are considered in the current study.

If we consider a dislocation line of Burgers vector b and line vector I, as shown in Fig. 3.4, located at a region of applied stress contains only yz shear components, and I make an angle α with b, each portion of a dislocation line will be subjected to a stress given by Peach-Koehler force [226]:

$$f = \tau b \times I = \tau b \begin{bmatrix} \sin \alpha \\ \cos \alpha \\ 0 \end{bmatrix} \qquad (3.23)$$

Where τ is the critical resolved shear stress (CRSS).

The force f will be always perpendicular to the dislocation line and make a circular profile of the dislocation with a radius R. Also, the dislocation is subjected to a line tension $\mathcal{T}$ that is always parallel to the dislocation line. At equilibrium, the net force acting on a dislocation arc length $\mathrm{d}l = Rd\theta = 0$, this gives:

$$\tau bdl = 2\mathcal{T}\mathrm{d}\theta/2 \qquad (3.24)$$

And therefore:

$$\mathcal{T} = \tau bR \qquad (3.25)$$

The radius of dislocation line curvature is then inversely proportional to the applied stress. Next, when the dislocation line moves into interaction with particles, the net force acting on neighbouring particles due to the arc of dislocation can be calculated as [201, 202]:

$$F = \int_{\alpha_0+\frac{\theta}{2}}^{\alpha_0-\frac{\theta}{2}} \tau b \begin{bmatrix} \sin \alpha \\ \cos \alpha \\ 0 \end{bmatrix} Rd\alpha = 2R\tau b sin\left(\frac{\theta}{2}\right) \begin{bmatrix} sin\alpha_0 \\ cos\alpha_0 \\ 0 \end{bmatrix} \qquad (3.26)$$

To estimate the net force acting on single particle $\bar{F_p}$, on average, we assume the forces acting on the left and right side of particle are equal:

$$F_{left} = F_{right} = \bar{F_p}/2 \qquad (3.27)$$

And the distance L between the central particle to its neighbouring particles are equal:

$$L_{left} = L_{right} = L \qquad (3.28)$$

Noting that:

$$\frac{L}{2} = R\sin(\theta/2) \qquad (3.29)$$

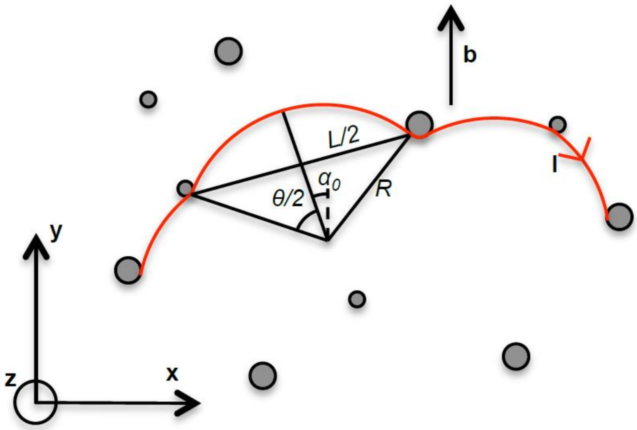

Fig. 3.4 Dislocation with Burgers vector b and line vector I interacting with particles [227].

Finally, we can derive the intensity of the force:

$$\bar{F_p} = \mathrm{L}\tau b \qquad (3.30)$$

The CRSS increment due to the presence of particles is then [201, 202]:

$$\Delta\tau_p = \frac{\bar{F_p}}{bL} \qquad (3.31)$$

3.8.2.1.2 Bypassed precipitates

For bypassed precipitates, the dislocation bows until $\theta = \pi$ and $L = 2R$, leading to the force due to bypassed precipitates:

$$F^{bp} = 2\tau bR = 2\mathcal{T} \qquad (3.32)$$

The line tension $\mathcal{T}$ is often approximated by [121, 201, 202]:

$$\mathcal{T} = \beta\mu b^2 \qquad (3.33)$$

Where β is the tension line constant and μ is the shear module.

Then we have:

$$F^{bp} = 2\beta\mu b^2 \qquad (3.34)$$

Take Eq. (3.35) into Eq. (3.32), the CRSS increment due to bypassed precipitates is finally:

$$\Delta\tau^{bp} = \frac{2\beta\mu b}{L} \qquad (3.35)$$

3.8.2.1.3 Sheared precipitates

For sheared precipitates, F_p can be expressed as [202]:

$$F^{sh} = k\mu b\bar{r} \qquad (3.36)$$

Where $\bar{r}$ is the average intersect radius of precipitates with the shear plane and k is a constant.

Fig. 3.5 shows a situation where dislocation line shearing through one particle. The dislocation line swept area A after shearing through an obstacle and before meeting other obstacles (from situation 1 to situation 2, shadow area in Fig. 3.5). This area contains exactly one obstacle, therefore we have:

$$AN_A = 1 \qquad (3.37)$$

Where N_A is the area density of precipitates.

The bowing occurs at constant mean critical radius R_c. Since in the shearing situation the bowing angles are small, so we can estimate $\sin\theta \approx \theta$, the area A can then be calculated:

$$A = R_c^2\left[\frac{2\theta_c}{2} - \frac{sin2\theta_c}{2}\right] - 2R_c^2\left[\frac{\theta_c}{2} - \frac{sin\theta_c}{2}\right] \approx \frac{R_c^2\theta_c^3}{2} \qquad (3.38)$$

From Eq. (3.29) we know that:

$$L^{sh} = 2R_c \sin(\theta_c/2) \qquad (3.39)$$

This leads to:

$$R_c^2\theta_c^3 \approx {L^{sh}}^2\theta_c \qquad (3.40)$$

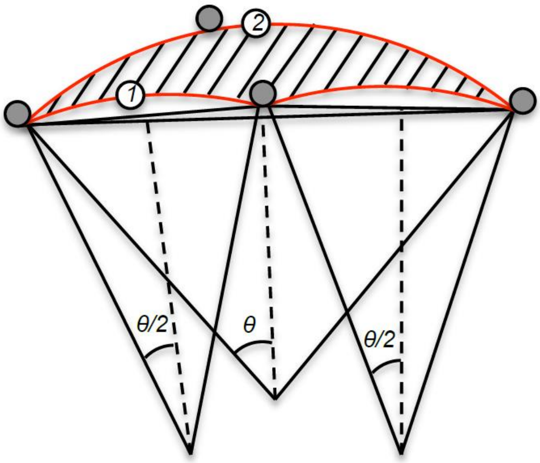

Fig. 3.5 Dislocation shearing through a particle. The area swept by dislocation line from situation 1 to situation 2 contains one particle [227].

With $AN_A = 1$, we can finally have:

$$\frac{{L^{sh}}^2\theta_c}{2}N_A = {L^{sh}}^2\frac{F^{sh}}{2\mathcal{T}}N_A = 1 \qquad (3.41)$$

The effective particle spacing is then:

$$L^{sh} = \sqrt{\frac{2\mathcal{T}}{F^{sh}N_a}} \qquad (3.42)$$

Combine Eq. (3.32), (3.37) and (3.43). The CRSS increment due to sheared precipitates is finally:

$$\Delta\tau^{sh} = \frac{{F^{sh}}^{3/2}}{b}\sqrt{\frac{N_a}{2\mathcal{T}}} = \mu\sqrt{\frac{k^3\bar{r}^3N_a}{2\beta b}} \qquad (3.43)$$

Usually, the precipitate is sheared when its size is small, while the large precipitates are bypassed. We can then define a critical radius r_c where the shearing mechanism starts to transit to bypass and the forces for shearing and bypass are equal [121]:

$$r_c = \frac{2\beta b}{k} \qquad (3.44)$$

3.8.2.2 Precipitate strengthening model for twinning

The current study uses the equation from a super dislocation model proposed by Barnett *et al.* [220] to estimate the precipitate strengthening on twinning plane. As described in Section 2.7.2, the principal equation is Eq. (2.11).

Where the term $n'b$ can be eliminated with an empirical relationship from [220]:

$$n'b = b_0' \left(\frac{d}{b}\right)^{\frac{1}{3}} \qquad (3.45)$$

Where b is the Burgers vector, d is the diameter of precipitates, b_0' is an empirical coefficient. For $b = 0.3$ nm, $b_0' = 0.39$ nm. For $b = 0.049$ nm, $b_0' = 0.22$ nm.

4. Precipitation kinetics in Mg-Zn alloy

4.1 Introduction

For a better understanding of precipitation processes in Mg-Zn alloys, this chapter investigates the precipitation kinetics of rod and plate-shaped precipitates in a Mg-Zn alloy using a combination of TEP, TEM, XRD and APT. TEM observation is conducted to measure the shape, size and distribution of rod and plate precipitates. TEP, XRD and APT are employed to characterize the solute evolution during ageing. In addition, a modified KWN model for rod and plate-shaped precipitates is applied to guide the interpretation of the experimental results.

4.2 Results

4.2.1 TEM characterization of precipitates during ageing

The state of precipitation in the Mg-4.5Zn alloy was observed at key ageing times using TEM (courtesy of Mahmoud Reza Ghandehari Ferdowsi). Fig. 4.1 presents a selection of TEM images at peak-aged conditions at 150 ℃ and 200 ℃ and over-aged conditions at 200 ℃. It is shown that, at all conditions, the dominant precipitate is β_1' along the [0001] axis. This is in agreement with previous literature [194, 228, 229]. For peak-aged conditions at 150 ℃ and 200 ℃ (Fig. 4.1(a) and (b)), the majority of precipitates observed are rod-shaped and a few blocky-shaped β_1' precipitates with no β_2' precipitates. The rod-shaped β_1' precipitates formed at peak-ageing condition at 200 ℃ were observed to be shorter and thicker and with a smaller number density than that at 150 ℃. When over-aged at 200 ℃ (Fig. 4.1(c)), the presence of plate shaped β_2' precipitates can also be observed.

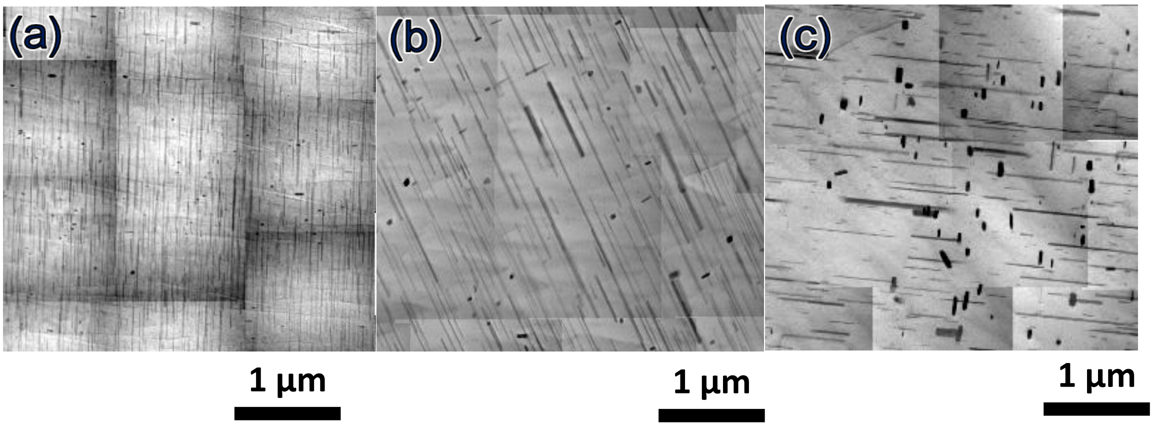

Fig. 4.1 TEM images of precipitates in aged Mg-4.5Zn alloy. (a) aged at 150 ℃ for 84 h (peak-aged). (b) aged at 200 ℃ for 12 h (peak-aged). (c) aged at 200 ℃ for 180 h (over-aged). In all figures, the zone axis is $[11\bar{2}0]$.

The average size, number density and volume fraction of β_1' and β_2' precipitates obtained from TEM are summarized in Table 4.1 and Table 4.2. The size of both precipitates is increasing, and number density is decreasing with increasing ageing temperature and time. The volume fraction of β_1' precipitates at 150 ℃ peak-ageing is twice larger than that at 200 ℃ peak-ageing, and the volume fractions of β_2' precipitates are negligible in the peak-aged conditions. In the over-aged condition at 200 ℃, the volume fraction of β_1' and β_2' precipitates appear to be similar. This is clear evidence that the β_2' precipitates

Table 4.1 Average size, number density and volume fraction of rod-shaped β_1' precipitates calculated from TEM measurement at different ageing conditions.

Ageing conditions	Length l (nm)	Diameter r (nm)	Aspect ratio (l/r)	Number density (m^{-3})	Volume fraction
150 ^{o}C-84h (peak-ageing)	275(±10)	10(±2)	29	4.3×10^{-20}	0.0093
200 ^{o}C-12h (peak-ageing)	395(±14)	11(±3)	37	1.3×10^{-20}	0.0051
200 ^{o}C-180h (over-ageing)	251(±12)	19(±8)	13	8.4×10^{-19}	0.0054

Table 4.2 Average size, number density and volume fraction of plate-shaped β_2' precipitates calculated from TEM measurement at different ageing conditions.

Ageing conditions	Thickness t (nm)	Diameter r (nm)	Aspect ratio $(2r/t)$	Number density (m^{-3})	Volume fraction
150 ºC-84h (peak-ageing)	13.9(±0.4)	28.7(±1.4)	2.06	4.7×10^{-19}	0.00043
200 ºC-12h (peak-ageing)	19.0(±0.6)	50(±2)	2.6	2×10^{-19}	0.00077
200 ºC-180h (over-ageing)	39.3(±1.4)	101.2(±3.4)	2.57	1.7×10^{-19}	0.0055

appear after peak-ageing. The volume fraction of β_1' precipitates appears to plateau from peak-ageing to over-ageing at 200 ℃ combined with an increase of their diameter, showing a clear sign of coarsening. This also suggests that the β_2' precipitates form as a new phase rather than arising from a structural transformation of the β_1' precipitates.

4.2.2 APT measurement

To further analyse the state of precipitation in the peak-aged alloys, APT was used to analyse the matrix solute content in these conditions (courtesy of Lu Jiang). Fig. 4.2 (a) and (b) show the three-dimensional reconstructed areas of alloys peak-aged at 150 ℃ and 200 ℃, respectively. The Mg solute appears to be highly uniform in the collected APT volumes. The presence of rods precipitates is revealed in the two studied volumes and the different precipitates are observed to be aligned in the same direction, agreeing with the TEM results in Fig. 4.1. Iso-concentration surfaces were used to highlight the precipitates and to generate average proxigrams for the two conditions, as shown in Fig. 4.2 (c) and (d). The proxigrams are computationally generated 1D composition profiles from the matrix to the centre of the precipitates. The Zn content in the matrix was respectively found to be 0.59 and 0.72 at.% after peak-ageing at 150 ℃ and 200 ℃. This increased matrix solute content as a function of temperature agrees with the increased Zn solubility when the temperature is increased.

The Zn-to-Mg ratio in the precipitates is found to be close to 3 : 2 in the two samples, which differs from the commonly proposed ratio in the literature of ~ 2 : 1. This difference might arise from the local magnification artefacts inherent to APT caused by the uneven evaporation rates of Mg (21 V/nm) and Zn (33 V/nm), which artificially

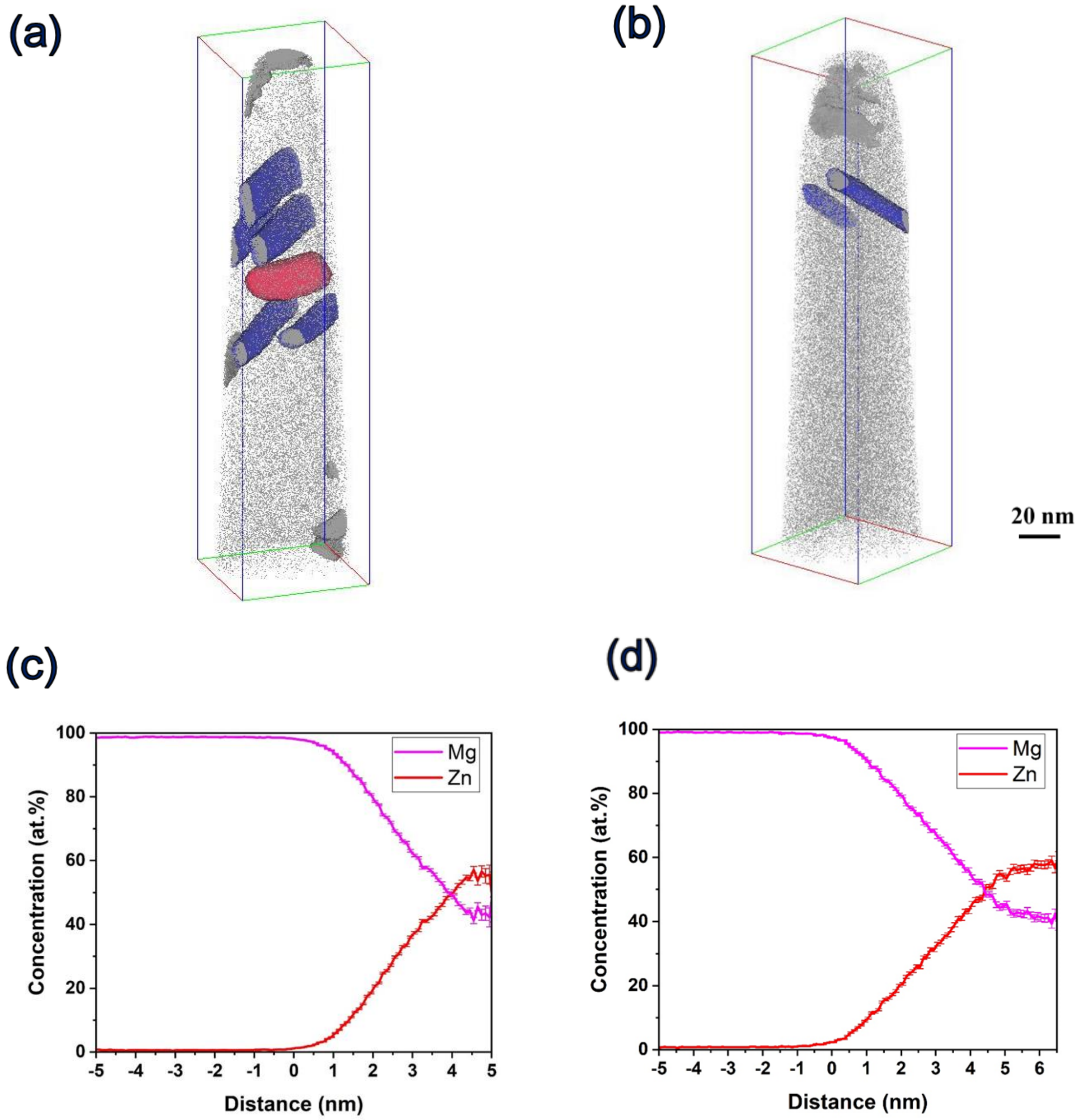

Fig 4.2 Reconstructed elemental maps containing Mg and Zn of samples aged at (a) 150 ℃ for 84 h and (b) 200 ℃ for 12 h, elements are coloured grey and the precipitate surfaces are coloured blue. And the corresponding Proxigram generated from the matrix to the centre of precipitates of samples aged at (c) 150 ℃ for 84 h and (d) 200 ℃ for 12 h.

enriches the precipitates with the matrix element. This points out to the limits of using APT for obtaining accurate precipitate compositions. However, APT is a powerful tool to quantitatively assess the matrix solute content (far from the precipitate interfaces) that can provide a reliable tool to assess the state of the precipitation process.

4.2.3 TEP and hardness measurements

The relative TEP variations during ageing of Mg-4.5wt%Zn, Mg-2.8wt%Zn, Mg-1.9wt%Zn alloys and pure Mg were measured, samples were extruded and solutionized for 0 h, 6 h and 12 h at 370 ℃ followed by water quenching. Fig. 4.3 shows the TEP variations (ΔS) of the extruded and solution-treated Mg-4.5Zn alloy during isothermal ageing at 150 ℃ (Fig. 4.3(a)) and at 200 ℃ (Fig. 4.3(b)), the variations are compared to the Vickers hardness kinetics of Mg-4.5Zn alloy (Fig. 4.3(c) and (d)). As can be seen, the precipitation kinetics are found to be very similar in both as-extruded and as-solutionised samples, suggesting that the as-extruded samples are fully solutionised. For both temperatures, the TEP kinetics was found to be stable at the early stages of ageing, followed by a sharp decrease, then the decreasing rate becomes slower. Contrarily the hardness was found to increase at first, then stabilise to a plateau before initiating a decrease over long ageing times. Three distinct stages during ageing can be identified from this kinetics: (I) The nucleation period where both TEP variation and hardness increment are close to 0 (this is because small coherent clusters will act as solute elements and will not impact TEP). (II) The growth stage where the TEP drops and the hardness increases. This stage corresponds to the precipitation of rod-shaped β_1' phase, which is known to be the dominant strengthening precipitate in the studied material [194, 228, 229]. Peak-ageing conditions are reached at the end of this stage which is demonstrated by a plateauing of hardness at respectively ~ 20 ΔHv and 17 ΔHv at 150 ℃ and 200 ℃. (III) The coarsening stage, during which the TEP decreases at a slower rate and the hardness decreases, indicating the over-ageing of the alloy. The continued drop of TEP after peak-ageing indicates that the matrix solute content continues to drop indicating that the precipitation process is still ongoing despite the drop in hardness which is often largely attributed to coarsening. As a result, step (III) can be better described as a "combined coarsening and precipitation stage". This agrees with the TEM results which revealed the apparition of the majority of β_2' precipitates between the peak-aged and over-aged conditions. To summarise, stage (III) corresponds to: 1. coarsening of the β_1' precipitates, which leads to the decrease of hardness and 2. The formation of the β_2' precipitates, which leads to a decrease in solute concentration and a drop in TEP. 3. The decrease of solute concentration itself also leads to a decrease in hardness. It can hence be concluded that the softening effects caused by coarsening of β_1' precipitates and loss of solute elements exceed the hardening effect from the formation of the β_2' precipitates.

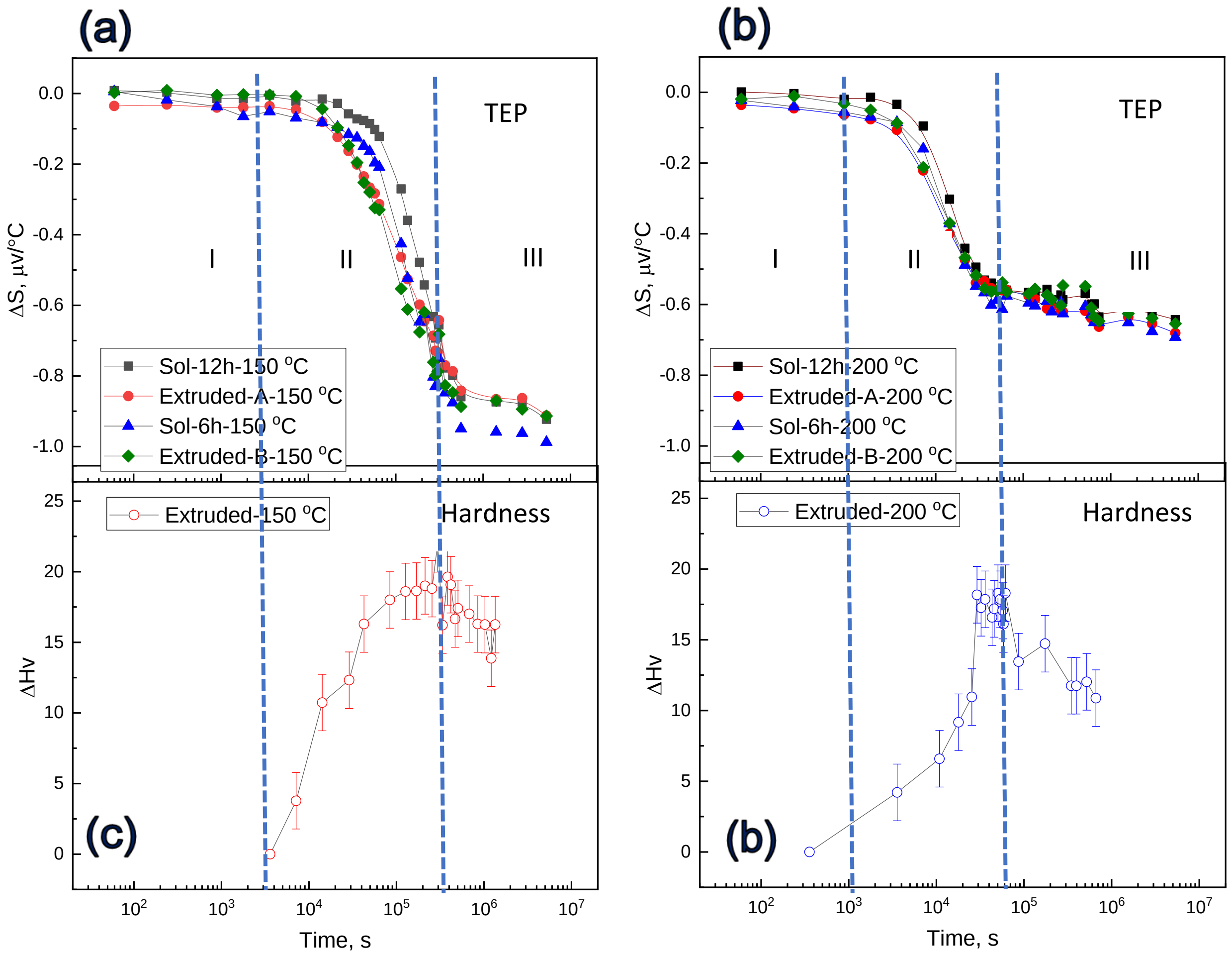

Fig 4.3 Comparison between TEP and hardness kinetics during ageing at (a), (c) 150 ℃ and (b), (d) 200 ℃.

4.2.4 Determination of Zn solute through TEP and XRD

The Zn solute concentrations in aged alloys can be determined using TEP and XRD. But the analysis of both TEP and XRD requires the knowledge of relationship between solute content and TEP signal/lattice parameter. This can be obtained from samples with known solute levels. To achieve this, solution-treated samples with Zn concentrations of ~ 1.9 wt.%, ~ 2.8 wt.% and ~ 4.5 wt.% were prepared and examined by energy-dispersive X-ray (EDX) analysis together with scanning electron microscopy (SEM) (courtesy of Jun

Wang). Tests were performed using a field emission LEO 1530 SEM with an accelerating voltage of 20 kV and a working distance of ~ 10 mm. Relevant results are presented in Fig. 4.4. As can be seen samples with ~ 1.9 wt.% Zn and ~ 2.8 wt.% Zn display a spatially homogeneous distribution of Zn, close to its nominal composition, while the sample with ~ 4.5 wt.% Zn presents some fluctuation of Zn with concentrations from ~ 4 to 5 wt.%. This is the result of micro-segregation during the casting of the alloys.

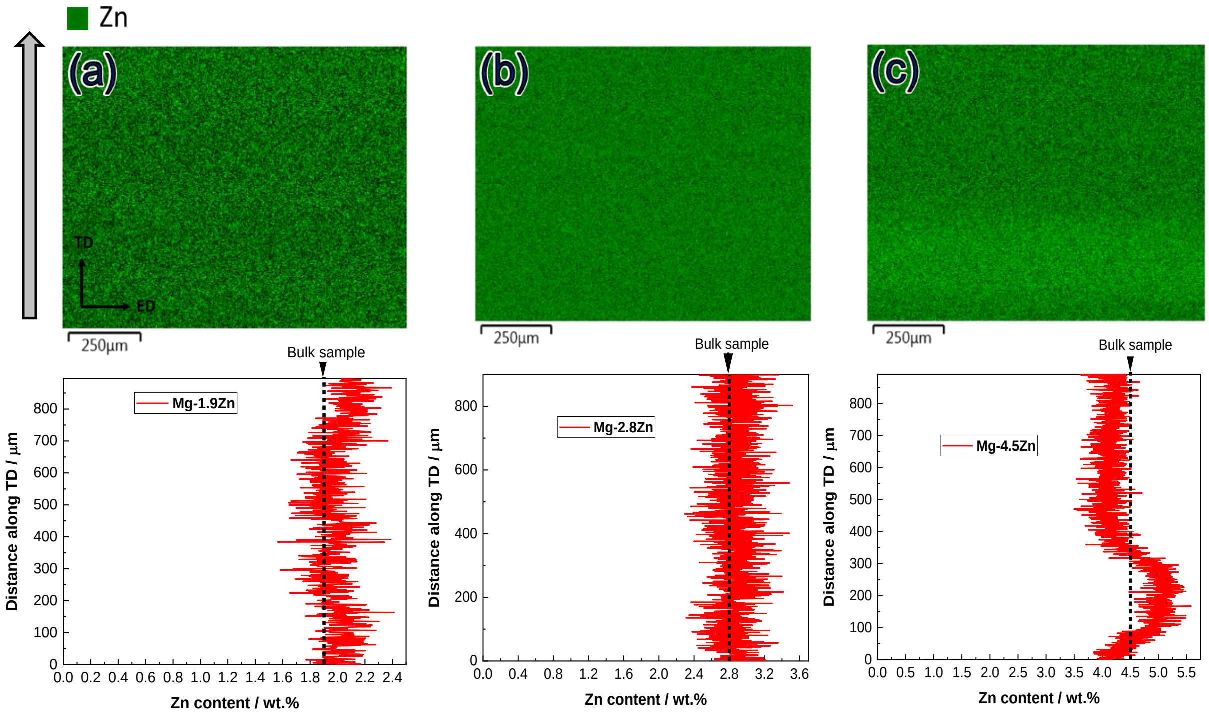

Fig. 4.4 EDX scans and relevant line scans along TD of samples solution treated for 6 h with Zn concentration of (a) ~ 1.9 wt.%, (b) ~ 2.8 wt.% and (c) ~ 4.5 wt.%.

In addition, as revealed by the APT measurements conducted on the ~ 4.5 wt.% Zn sample (Fig. 4.5), Zn clusters are observed. The concentration of Zn solute content was found to be ~ 3.5 wt.% in the analysed volume. The small clusters are believed to be due to natural ageing effects. Similar results were also reported in [49] where clusters are formed following the heat treatment of Mg-Zn alloys with higher Zn concentration. According to the EDX and APT results, ranges of element in solution can be obtained for the three conditions.

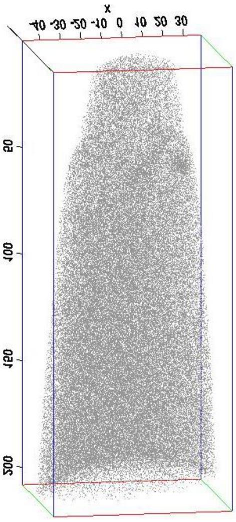

Fig. 4.5 Reconstructed elemental maps of Zn in a Mg-4.5Zn sample solution treated for 6 h.

Combining the TEP results for samples with known composition, we plot 1/ΔSss against 1/[Zn]wt% based on Eq. (3.5) in Fig. 4.6. The uncertainties in the composition measurements are obtained from EDS measurements, a 95% confidence band is presented to estimate the regression line between variables. The plots show a linear relationship, which validates the Gorter–Nordheim law in the current material and provides a reference.

The lattice parameters measured from XRD in Mg-Zn with the addition of Zn in magnesium alloys are shown in Fig. 4.7 (courtesy of Sitarama R. Kada). The trend is linear, which agrees with [96]. This allowed us to determine the lattice parameters and subsequently the solute content in aged alloys. Table 4.3 shows the measured lattice parameters using XRD for aged alloys and the corresponding Zn concentrations. The Zn concentrations are derived by fitting the tested lattice parameters into the linear relationship in Fig. 4.7.

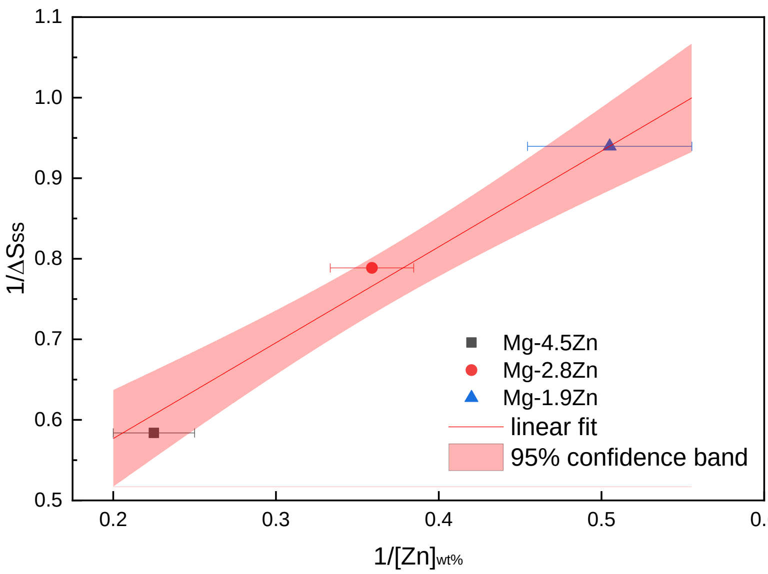

Fig. 4.6 Relationship between 1/[Zn]wt% and 1/ΔSss derived from alloys with three different Zn concentrations in Gorter-Nordheim law.

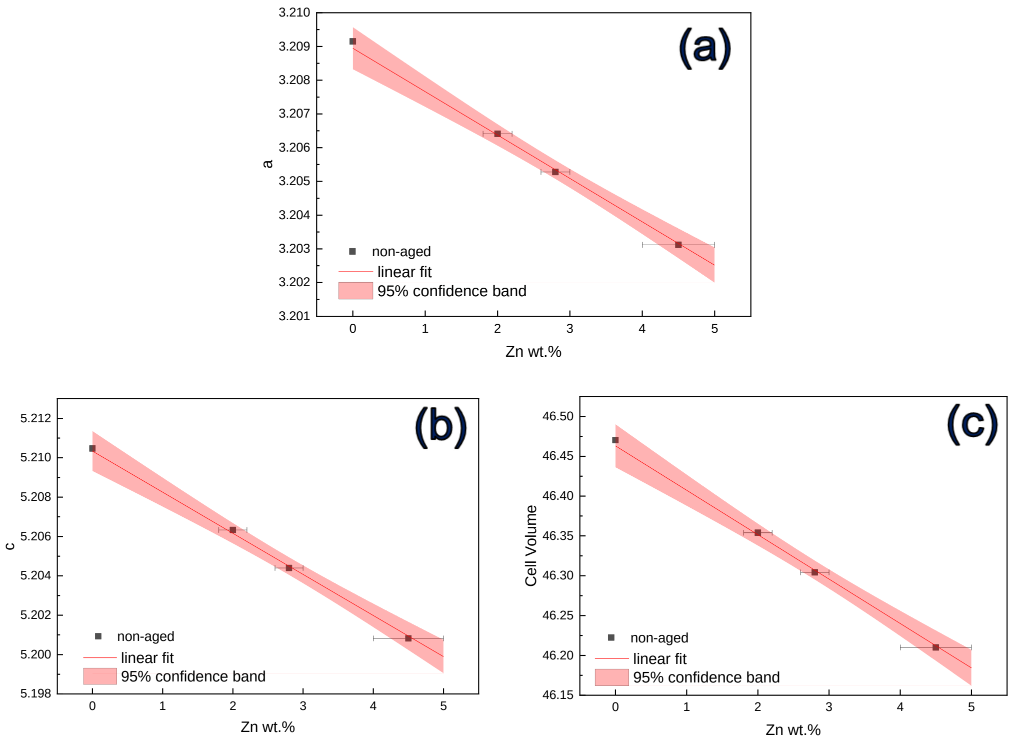

Fig. 4.7 Influence of Zn content on lattice parameters (a) a, (b) c and (c) cell volume in Mg-Zn alloy. Errors limits are derived from Fig. 4.4.

Table 4.3 Measured lattice parameters (Å) and derived Zn concentration (wt.%) for alloys with different ageing conditions using the relationship from Fig. 4.7

Ageing conditions	Measured a (corresponding Zn concentration)	Measured c (corresponding Zn concentration)	Measured cell volume (corresponding Zn concentration)	Derived mean Zn concentration value
150 ºC-84h (peak-ageing)	3.2057 (2.51±0.2)	5.2046 (2.69±0.22)	46.3191 (2.58±0.2)	2.59±0.22
150 ºC-155h (over-ageing)	3.2068 (1.63±0.24)	5.2066 (1.78±0.27)	46.3707 (1.69±0.25)	1.7±0.27
200 ºC-12h (peak-ageing)	3.2051 (2.94±0.21)	5.2041 (2.95±0.21)	46.2977 (2.95±0.2)	2.95±0.21
200 ºC-180h (over-ageing)	3.2059 (2.31±0.2)	5.2055 (2.29±0.23)	46.3346 (2.31±0.26)	2.3±0.26

4.2.5 Comparison between results from different techniques

Using Eq. (3.5) and the relationship in Fig. 4.6, the evolution of Zn solute as a function of ageing time can be obtained from TEP and is compared to the solute obtained from other techniques in Fig. 4.8.

The solute content from TEM is back-calculated from the measured volume fractions of β_1' and β_2' precipitates using Eq. (3.22). Here X_{Zn}^0 =0.0172, and we assume the β_1' precipitate composition is Mg_4Zn_7, corresponding X_{Zn}^p = 7/11, and β_2' precipitate composition is $MgZn_2$, corresponding X_{Zn}^p = 2/3. To address the atomic ratio α, the atomic volume of Mg, $MgZn_2$ and Mg_4Zn_7 are calculated. For Mg, the atomic volume can be obtained through averaging volume by atom number in a lattice unit. The structure of $MgZn_2$ and Mg_4Zn_7 can be analysed using the VESTA software [230], the atomic volumes of $MgZn_2$ and Mg_4Zn_7 are calculated as 1.62×10^{-29} and 1.72×10^{-29} m^3. The atomic ratios α for $MgZn_2$ and Mg_4Zn_7 are then determined as 1.43 and 1.35.

Fig. 4.8 shows an overall agreement between the different techniques used to obtain solute content, particularly at long ageing times. Larger discrepancies can be observed at intermediate ageing times which can be attributed to the uncertainties arising from the different techniques, this will be discussed in the later section.

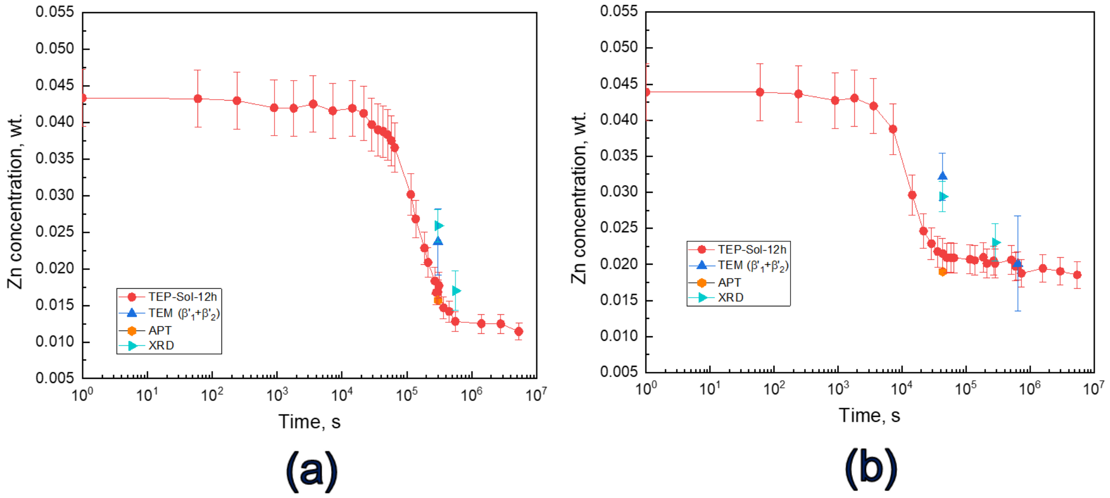

Fig. 4.8 Zn solute content at different ageing times obtained from different characterization techniques at (a) 150 ℃ and (b) 200 ℃.

It is also interesting to find that the solute limit from all techniques in the current study (~ 1.3 – 1.7 wt.% at 150 ℃ and ~ 2 – 2.3 wt.% at 200 ℃) is lower than the equilibrium limit in Mg-Zn phase diagram from many popular databases such as KNOVEL (ASM Handbook, Volume 03 - Alloy Phase Diagrams) [231] (~ 2.6 wt.% at 150 ℃ and ~ 3.6 wt.% at 200 ℃), THERMOCALC (TT Mg-alloys database v4.2) [232] (~ 2 wt.% at 150 ℃ and ~ 3.1 wt.% at 200 ℃) and PANDAT [233] (~ 1.9 wt.% at 150 ℃ and ~ 2.8 wt.% at 200 ℃). The values in the mainstream databases are calculated based on thermodynamic equations with certain parameters fitted from experiments in literature, thus results are always slightly different from database to database depending on their resources. The current study indicates that more work needs to be done to improve the phase diagram calculation.

4.3 Precipitation modelling

Precipitation modelling was employed to analyse the formation kinetics of β_1' and β_2' precipitates. To distinguish the two precipitate species, all β_1' rods are assumed to have a composition of Mg_4Zn_7, and β_2' plates are assumed to have a composition of $MgZn_2$. The current work is built on the PreciSo software [18, 19]. It uses classical nucleation and growth theories to simulate precipitation kinetics which is fully described in Section 3.8.1. An interface is written in Python which incorporates the PreciSo module to simulate the precipitation kinetics in Mg-Zn alloy. The code can be found in Appendix 8.2.1.

4.3.1 Calibration of precipitation model

The precipitate solubility (A and B in Eq. (3.20)) can be acquired through linear fitting of $log_{10}K_s$ with $1/T$, by taking the K_S at 150 ℃ and 200 ℃ when the solute reaches equilibrium for certain precipitates. Here we estimate the solutes at peak-ageing conditions are the equilibrium for β_1' since β_1' rod is the dominant phase at this stage (Fig. 4.1), and we took the longest ageing time (~ 2 months) for the equilibrium of β_2' as this is the condition where the largest amount of β_2' has formed. The Zn concentrations for calibration were obtained from APT and TEP and are corrected by Gibbs-Thomson equation to eliminate the surface effect [21]:

$$[\mathrm{Zn}]_{wt.\%}^{GT} = [\mathrm{Zn}]_{wt.\%} \exp\left[-\frac{r_0^i}{r}\right] \qquad (4.1)$$

For β_1' rod-shaped precipitates with composition Mg_4Zn_7:

$$r_0^1 = \frac{4b_r\gamma v_{at}^p \times (4+7)}{k_bT(3b_r-2)} \qquad (4.2)$$

For β_2' plate-shaped precipitates with composition $MgZn_2$:

$$r_0^2 = \frac{2(b_p+2)\gamma v_{at}^p \times (1+2)}{3k_bT} \qquad (4.3)$$

Since in Eq. (3.14) and (3.16) only one lattice parameter is permitted while Mg alloy has two lattice parameters, the equivalent cubic structure with same volume is considered and an equivalent lattice parameter a is used. The diffusion coefficient for Zn has been taken from ref. [234]. The chemical composition of respectively rod-shaped β_1' and plate-shaped β_2' is assumed to be Mg_4Zn_7 and $MgZn_2$. Their atomic volume was calculated with VESTA [230]. The surface energy of precipitates was set as a fitting parameter, it was first evaluated from the reported values for Mg alloys [123, 124] to give a rough range (~ 0.02 to ~ 0.4 J/m^2), and the final value selected is the one that provides best agreement between simulation and experimental results.

Parameters for the precipitation model are listed in Table 4.4.

Table 4.4 Model parameters

Parameters	β_1'(Mg$_4$Zn$_7$)	β_2' (MgZn$_2$)	Reference
X_{Zn}^0 (at%)	1.72	1.72	This work
X_{Zn}^p	7/11	2/3	
Aspect ratio	25 (b_r)	2.5 (b_p)	TEM
A (k)	3759	1095	Derive from
B	-6.89	-2.06	APT and TEP
D_{Zn}^0 (m^2/s)	2.9×10^{-5}	2.9×10^{-5}	[234]
Q_{Zn} (kJ/mol)	118.6×10^3	118.6×10^3	[234]
γ (J/m^2)	0.041	0.0753	fitted
v_{at}^p (m^3)	1.72×10^{-29}	1.62×10^{-29}	[230]
α	1.35	1.43	[230]
Equivalent lattice parameter a	2.85×10^{-10}	2.85×10^{-10}	This work

4.3.2 Simulation results

The simulated precipitate radius and number density in comparison with TEM results at 150 °C and 200 °C are presented in Fig. 4.9. The model is in reasonable agreement with the TEM results apart from the radius for β_1' rods (Fig. 4.9 (a)) for which the predictions are smaller than the radius directly measured from TEM. This discrepancy could come from overly low surface energy used in the model.

The radius of the β_2' plates is always higher than that of β_1' rods (Fig. 4.9 (a) and (b)), the β_1' rods start dissolving after peak-ageing where β_2' plates start coarsening which is in good agreement with the TEM results. The number density of β_2' plates, on the other hand, has a slower kinetics and is always lower than β_1' rods until β_1' rods dissolve (Fig. 4.9 (c) and (d)). Though only few experiment points were compared with the model, it validates the most important phases during ageing (peak and over-ageing stages) for the precipitation model. Overall, the current model and parameters give a reasonable prediction of precipitation kinetics of the studied alloy.

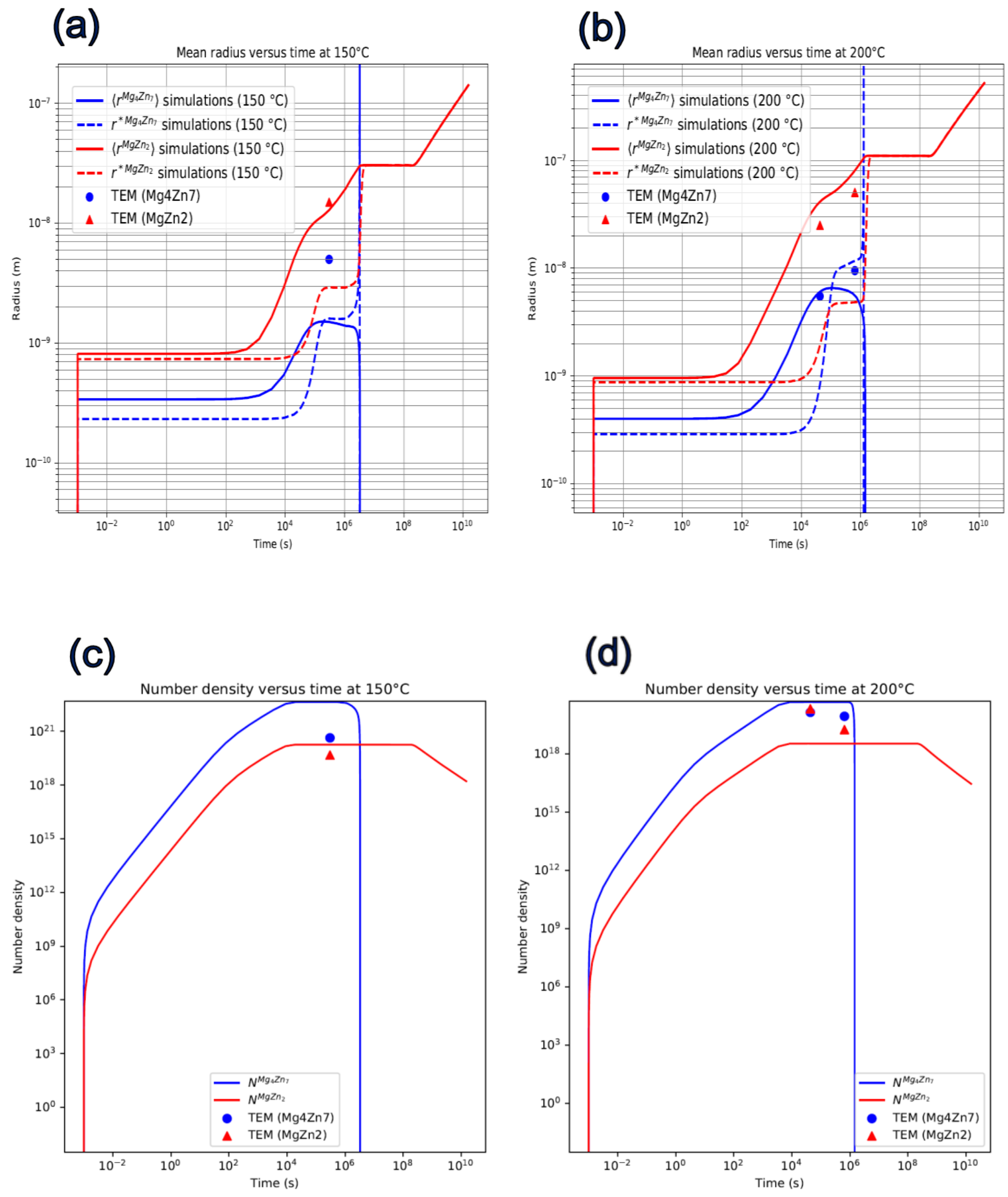

Fig. 4.9 Simulation results of (a)(b) mean radius and (c)(d) number density evolution of rod and plate-shaped precipitates in Mg-4.5Zn alloy during ageing at (a)(c) 150 ℃ and (b)(d) 200 ℃, in comparison with experimental data from TEM.

4.4 Discussion

4.4.1 Limitations of characterization techniques

The solute content at different ageing conditions and the precipitation kinetics are compared in Fig. 4.8 using various techniques. Though the overall results show good agreement with each other, some differences are still observed at intermediate ageing times.

The analysis of TEP and XRD has the advantage of measuring bulk area. But both rely on the assumption that the initial solute composition is known. The solute contents obtained from TEP and XRD measurements also assume no contribution from the precipitates. Although this might be true for a long ageing time where the precipitates are largely incoherent, some influence of the precipitates might arise at early ageing time where the precipitates are smaller with added coherency. Such influences have been reported in some other alloying systems. For example, in a TEP study of Al-Mg-Si alloy, the prevalence of a semi-coherent phase causes an increase in TEP signal [235], it is believed to be due to the evolution in the intrinsic effect of the precipitates during the phase transformation [236-238]. The misfitting precipitates are also shown to induce the change in matrix lattice parameters in the XRD studies on Cu, Al alloys and steel [97, 98]. While a small change of lattice parameters could lead to a considerable variation of solute content during the XRD analysis according to Fig. 4.7. However, the intrinsic influence from precipitates on TEP and XRD analysis differs from material to material. Quantifying this influence in the current system is challenging.

With regards to the APT and TEM, they provide direct and precise microstructural and chemical information. But these techniques are only able to analyse relatively small areas and the extrapolation of these results to the bulk can be hindered by the presence of local inhomogeneity in the material as was revealed earlier in SEM observations in Fig. 4.4. The TEM results are also affected by the significant errors arising from the estimation of the foil thickness to obtain the precipitates volume fractions. In the current study, an uncertainty of ~ 10% was observed between the foil thicknesses measured from EELS and CBED. Also, when using TEM to access the solute content, additional errors could come from the assumptions of precipitate composition when translating the volume fraction into solute concentration.

4.4.2 Evolution of precipitate volume fraction during ageing

The solute content obtained in Fig. 4.8 can be translated to precipitate volume fraction using a variation of Eq. (3.22), with the exception of TEM where precipitate volume fraction was first obtained, assuming a certain composition for all precipitates:

$$f_v = \frac{X_{Zn}^0 - X_{Zn}}{\alpha\,(X_{Zn}^p - X_{Zn})} \quad (4.4)$$

For the case of the β_2' plate, the stoichiometry of $MgZn_2$ is well-established. There is however some uncertainty regarding the composition of the β_1' precipitates. Up to now, the proposed compositions for β_1' rod found in literature are meta-stable Mg_4Zn_7 [64-67] and $MgZn_2$ [60, 73]. They have even been found to coexist as dual phases in a single β_1' rod [68]. The question is to what degree the variation from one composition to another could affect the calculation of precipitate volume fraction. To answer this, the translated volume fractions of precipitates using Eq. (4.4) at 150 ℃ and 200 ℃ from different techniques (except TEM which is a direct measurement) are depicted in Fig. 4.10 to have a direct comparison. Note that, in each translated result, all precipitates can only be assumed to have one composition, in this case, either Mg_4Zn_7 or $MgZn_2$. Respectively solid points and dotted lines from TEP represent the translated volume fraction assuming all precipitates have the composition of Mg_4Zn_7 (FV_{Mg4Zn7}) and $MgZn_2$ (FV_{MgZn2}). The difference between FV_{Mg4Zn7} (solid points) and FV_{MgZn2} (hollow points) at early ageing stage appears negligible. For a longer ageing time, the difference becomes more significant with FV_{Mg4Zn7} ~ 7% higher than FV_{MgZn2}. Overall, the difference is minor. Recent simulation works based on first principle methods indicate that hexagonal $MgZn_2$ is more thermally stable than monoclinic Mg_4Zn_7, but they have similar formation energies [239, 240]. It is likely that the composition of the β_1' rods evolves from the metastable Mg_4Zn_7 at early ageing times to the more stable $MgZn_2$ for longer ageing times. Hence the "real" volume fraction will be closer to FV_{Mg4Zn7} during early ageing and tend towards FV_{MgZn2} at later ageing stage (from both β_1' rods and β_2' plates, with the dominant composition of $MgZn_2$). This agrees with the volume fraction measured in TEM on an over-aged sample, which is closer to FV_{MgZn2}.

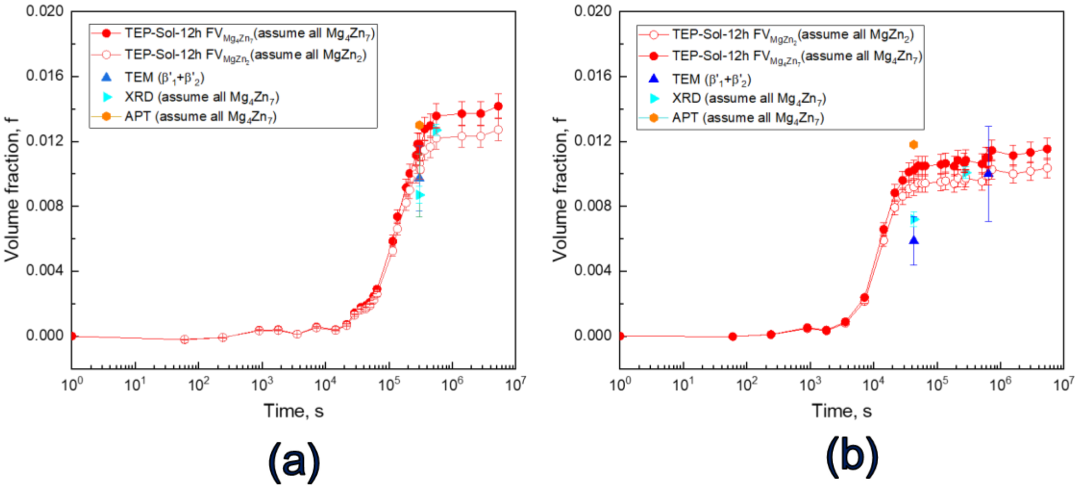

Fig. 4.10 Precipitate volume fraction evolution as a function of ageing time obtained from different characterization techniques at (a) 150 ℃ and (b) 200 ℃. Solid points consider all precipitates are Mg_4Zn_7 (except TEM), hollow points consider all precipitates are $MgZn_2$.

4.4.3 Modelling precipitate volume fraction

Modelling precipitate volume fraction can be computed from calculated radius and number densities. Historically $MgZn_2$ has been used as the only phase in existing models for the β_1' rods [124, 241] which has the limitation of not accounting for the possible presence of β_2' plates. Since changing precipitate composition does not induce a significant variation of estimated volume fraction, and for the convenience of distinguishing two precipitate species, the simulation in this work uses Mg_4Zn_7 to represent β_1' rods and $MgZn_2$ to represent β_2' plates.

Fig. 4.11 gives the simulated Zn solute concentration and precipitate volume fraction in comparison with experimental results. It shows that the Zn concentration evolution measured experimentally is pretty well captured by the model (Fig. 4.11 (a) and (b)). Note that there is a small plateau in the simulated curve which indicates the transition from one composition to the other. Fig. 4.11 (c) and (d) show the competition of volume fraction kinetics between β_1' rods and β_2' plates. Before peak-ageing, β_1' rods are dominating the precipitation, and they are then gradually replaced by β_2' plates. This is a new finding that has not been previously shown in the literature [124, 241]. The simulated results for the β_2' plates agree well with the TEM measurements and tend towards FV_{MgZn2} in Fig. 4.10.

The simulated results for the β_1' rods are below FV_{Mg4Zn7} in Fig. 4.10 but above the XRD and TEM results. This is reasonable as the experiments measure the overall precipitate volume fraction of Mg_4Zn_7 and $MgZn_2$, while the simulated β_1' rods only consider a composition of Mg_4Zn_7.

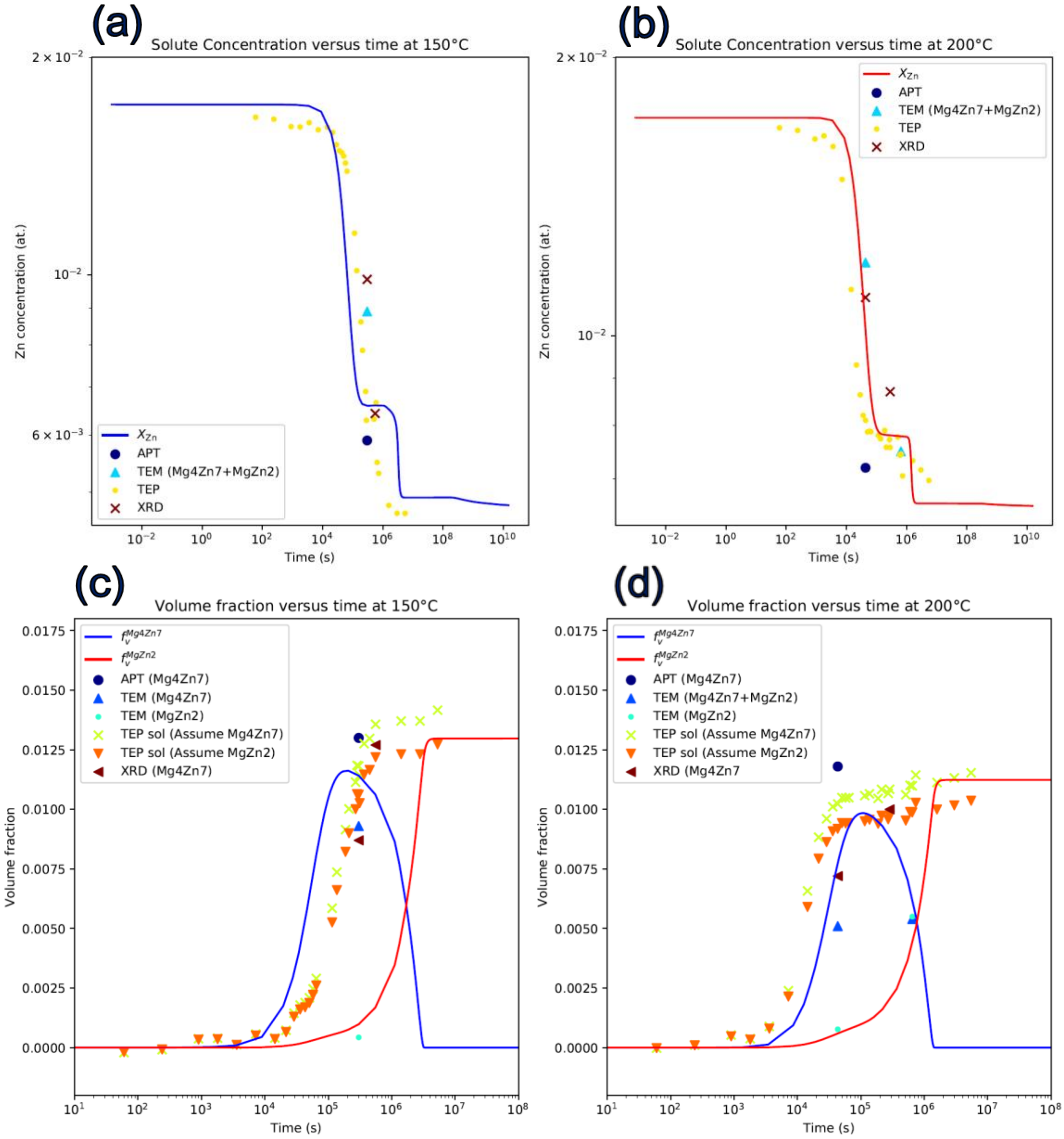

Fig. 4.11 Simulation results of (a)(b) Zn solute concentration and (c)(d) volume fraction evolution of rod and plate-shaped precipitates in Mg-4.5Zn alloy during ageing at (a)(c) 150 °C and (b)(d) 200 °C, in comparison with experimental data.

Based on the above information, a TTT (time-temperature-transformation) diagram can be calculated and proposed for the meta-stable $MgZn_2$ and Mg_4Zn_7 phases in the Mg-4.5wt.%Zn alloy (Fig. 4.12), where the time and temperatures required to reach 20%, 50% and 80% of maximum volume fraction of each phase are presented. Both phases show typical C-shape curves, with the Mg_4Zn_7 phase forming first, and the two phases starting to overlap at higher temperatures. This study is the first report of such a TTT diagram for Mg-Zn system.

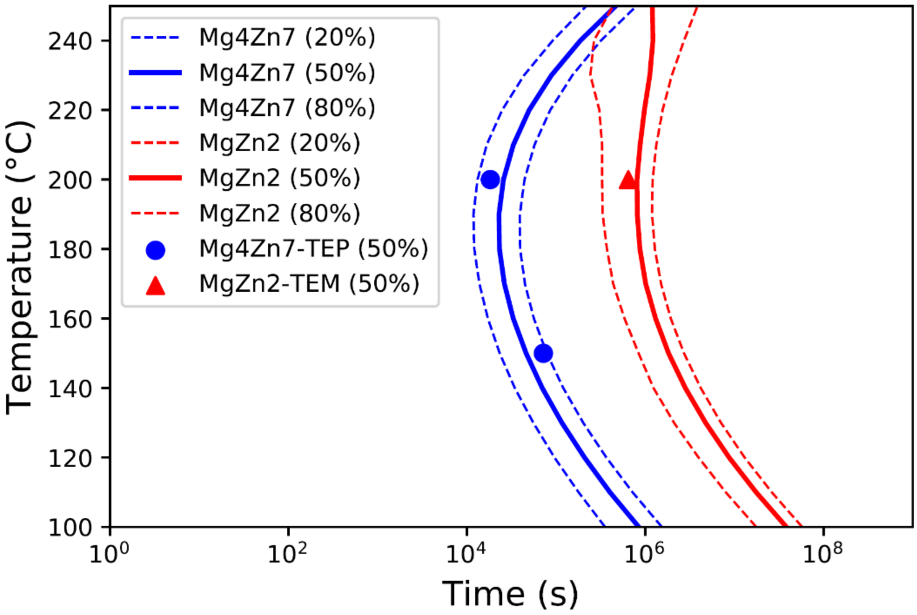

Fig. 4.12 TTT diagram of the formation of Mg_4Zn_7 and $MgZn_2$ phases in Mg-4.5wt.%Zn alloy. Experimental data estimated from TEP and TEM are also shown.

Although the present work considers both β_1' and β_2' with certain compositions (Mg_4Zn_7 and more stable $MgZn_2$), these precipitates would display a range of intermediate compositions which are not accounted for in the current model. The assumptions on precipitate compositions can explain some of the discrepancies between model and experimental results. One of the key assumptions to obtain the solubility product was that the microstructures are fully precipitated which is likely not the case which would lead to a slight underestimation of the total volume of precipitates at equilibrium. However, the current study only focuses on the meta-stable phases and the final equilibrium state is not considered. Overall, the proposed model, combined with the experimental results, assists in better understanding the precipitation sequence in Mg-Zn alloys.

4.4 Conclusion

The current study used multiple characterization techniques and a precipitation model to provide new perspectives in understanding complex precipitation in Mg-Zn alloy. The main conclusions are summarized below:

1. A combination of different techniques is used to measure the size of precipitates and solute concentration in Mg-Zn alloy, the precipitation kinetics is well characterized. TEP is applied in Mg alloy to follow the precipitation kinetics for the first time.
2. The solubility limit from this study at 150 ℃ and 200 ℃ was found lower than the current phase diagram in database (in THERMOCALC, PANDAT and KNOVEL).
3. A precipitation model based on classical nucleation and coarsening theories was adapted for Mg-Zn alloys that reproduces microstructural evolutions of β_1' and β_2' precipitates. A TTT diagram is proposed for this system.
4. Experimental and simulation results show that β_1' dominates the precipitation at early ageing stage, while β_2' starts to form after ~ 84 h at 150 ℃ and ~ 12 h at 200 ℃ and takes the dominance for the longer ageing time.

5. Influence of precipitates on slip in Mg-Zn alloy

5.1 Introduction

In Mg alloys, basal and prismatic slips are the two major slip modes that accommodate the deformation in tension along extrusion direction [152, 189, 196]. This chapter aims to investigate the precipitation hardening mechanism on basal and prismatic slips in Mg-Zn alloys, and eventually the tensile strength evolution during ageing, through a mechanical model. The model is built on interactions between dislocations and microstructure. First, classical expressions for mono-dispersed precipitates on basal and prismatic planes are developed where the size of precipitates are considered the same throughout the system. The effect of precipitate arrangements on the modelling results is discussed. They are then modified to model poly-dispersed precipitates on slip planes where different size distributions are considered, the results are compared with experiments.

5.2 Results

5.2.1 Mechanical model for mono-dispersed precipitates

The principles of the mechanical model used in this study were described in detail in Section 3.8.2.1. This model takes into account both Orowan bypass and shearing mechanisms with a critical radius r_c. For the shearing mechanism in Eq. (3.43), the particle spacing L has been eliminated so that the particle arrangement does not directly influence the results, instead, the area density N_a is more relevant. While for the bypass mechanism in Eq. (3.35), the key information to be solved is the mean particle spacing on slip planes. In Mg-Zn alloys, the two major strengthening precipitates are rod-shaped β_1' phase and plate-shaped β_2' phase, their geometry relationship with basal and prismatic shear planes are depicted in Fig. 5.1. As seen, rod precipitates have their long side perpendicular to the basal plane and parallel to the prismatic plane. And the plate precipitates have their large surface plane parallel to the basal plane and perpendicular to the prismatic plane. Currently, there are two kinds of arrangements proposed in the literature for this system: square (Robson *et al*. [10]) and triangle (Jain *et al*. [84] and Rosalie *et al*. [242]). Based on this, and assuming all precipitates have the same size and are distributed homogeneously on the slip planes, the mean particle spacing and resultant mechanical model for β_1' and β_2' precipitates are calculated in the following sections.

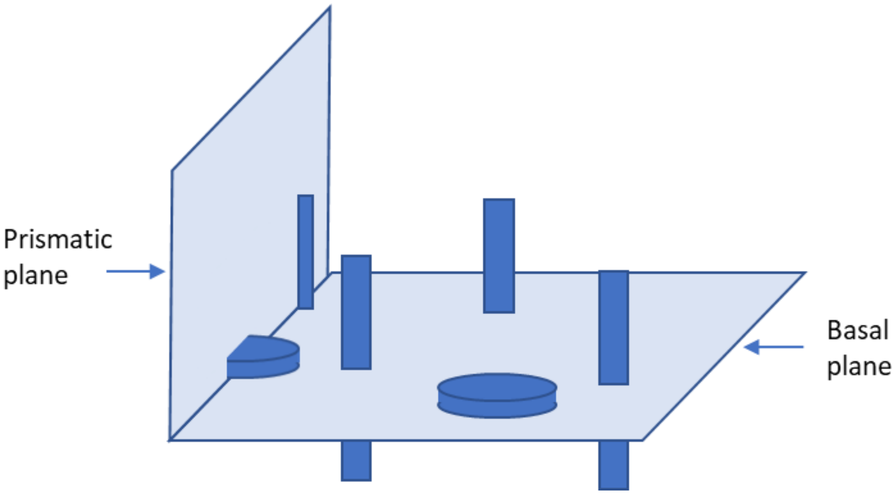

Fig. 5.1 Intersection of rods and plates on basal and prismatic planes.

5.2.1.1 Precipitates on {0001} basal plane

5.2.1.1.1 Rod precipitates

On basal plane, both rod and plate precipitates have circular shape intersections. For homogeneously distributed rods with length l and radius r, two simple cases can be considered: triangular and square arrangements as schematically shown in Fig. 5.2.

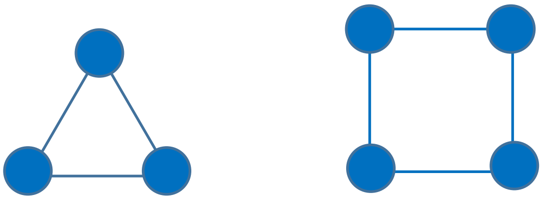

Fig. 5.2 Triangular and square arrangement of precipitate intersection on basal plane.

For triangular spacing, the average centre to centre distance between precipitates L and area density N_A on shear plane is related by:

$$N_a = \frac{2}{\sqrt{3}L^2} \qquad (5.1)$$

The area density of precipitates can also be estimated assuming the intersection of the shear plane with rods of radius r and length l:

$$N_a = N_v l' \qquad (5.2)$$

Where N_v is the number density of rods per unit volume which can be expressed as $\frac{f_v}{\pi r^2 l}$, f_v is the volume fraction of precipitates. l' is the probability of slip plane intersecting rods. In the current case, the long side of precipitates is perpendicular to the slip plane (Fig. 5.1), therefore $l' = l$, this eliminates the rod length l in N_a and the final expression of Eq. (5.2) becomes $N_a = N_v l' = \frac{f_v}{\pi r^2}$.

The combination of Eq. (5.1) and (5.2) leads to the particle surface to surface distance for triangular distribution:

$$L = r\sqrt{\frac{2\pi}{\sqrt{3} f_v}} - 2r \qquad (5.3)$$

When considering a square distribution, N_a becomes $\frac{1}{L^2}$, therefore:

$$L = r\sqrt{\frac{\pi}{f_v}} - 2r \qquad (5.4)$$

5.2.1.1.2 Plate precipitates

When precipitates have a plate shape of radius r and thickness t, the number density N_v becomes $\frac{f_v}{\pi r^2 t}$, and the probability of slip plane intersecting rods $t' = t$. As rods and plates have the same intersection shape and their geometry relationships with the basal plane are similar, the plate-shaped precipitates share the same expressions for particle spacing with rods as in Eq. (5.3) and (5.4).

5.2.1.2 Precipitates on $\{10\bar{1}0\}$ prismatic plane

5.2.1.2.1 Rod precipitates

As shown in Fig. 5.1, the rod precipitates are parallel to the prismatic plane, their intersections on the prismatic plane therefore have a near rectangular shape perpendicular to the basal plane. Their intersections on the prismatic plane are shown in Fig. 5.3. As seen, both arrangements have two sets of particle spacing values. Since the precipitation hardening should be dominated by the smaller particle spacings as they give higher stress increment according to Eq. (3.31), the effective particle spacing for square arrangement is considered L_{min} and L^* for triangular arrangement.

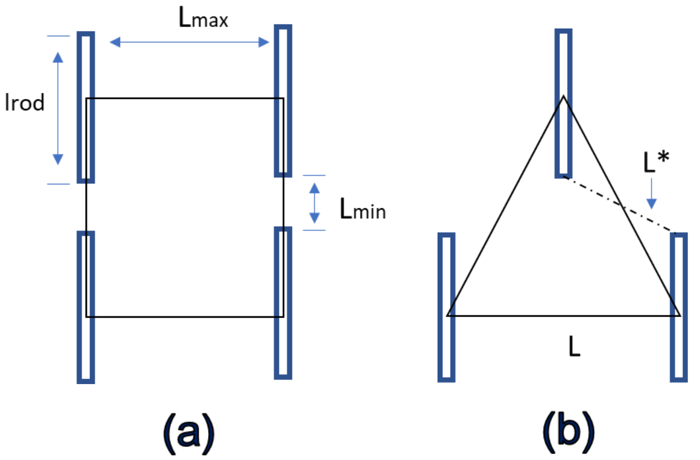

Fig. 5.3 Square and triangle arrangement of rod precipitate intersections on prismatic plane.

Considering a rod with length l and radius r intercepting a prismatic plane, the effective radius should have a value between 0 to r depending on the position of the precipitate respective to the intersecting plane, as shown in Fig. 5.4. Therefore, the mean intersect radius $\bar{r}$ is related to r by:

$$\bar{r} = \frac{1}{r}\int_0^r \sqrt{r^2 - x^2}\, dx = r\frac{\pi}{4} \qquad (5.5)$$

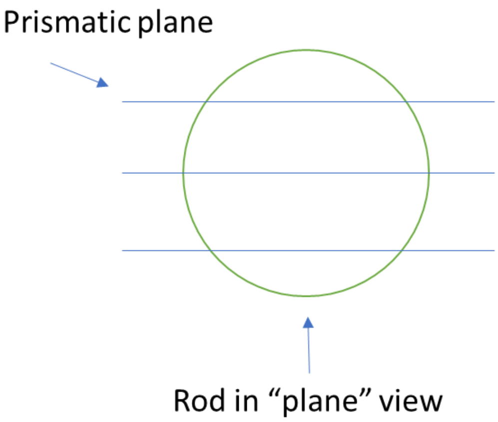

Fig. 5.4 Bottom view of rod intersection on prismatic plane.

The intersection volume of rods on prismatic plane has a thickness of $2r$. When a dislocation is bypassing the rods which are squarely distributed (Fig. 5.3(a)), the area density of precipitates on the slip plane is:

$$N_a = \frac{1}{(l+L_{min})(L_{max}+2\bar{r})} = N_v 2r \qquad (5.6)$$

With $(l + L_{min}) = (L_{max} + 2\bar{r})$, we can have the effective particle spacing for square arrangement:

$$L_{min} = \sqrt{\frac{\pi r l}{2f_v}} - l \qquad (5.7)$$

For triangular arrangement (Fig. 5.3(b)), N_a becomes $\frac{2}{\sqrt{3}L^2}$, and the centre to centre spacing L is therefore:

$$L = \sqrt{\frac{\pi r l}{\sqrt{3}f_v}} \qquad (5.8)$$

The effective particle spacing for triangular arrangement is then:

$$L^* = \sqrt{(L\frac{\sqrt{3}}{2} - l)^2 + (L\frac{1}{2} - 2\bar{r})^2} \qquad (5.9)$$

5.2.1.2.2 Plate precipitates

When the precipitates are plate-shaped, the intersection of precipitates on a prismatic plane has a rectangular shape parallel to the basal plane, similar to Fig. 5.3 with a 90° rotation. In this case, the long side of intersection is the effective radius $\bar{r}$ following Eq. (5.5) and the short side is the plate thickness t, the probability of rods intersecting a prismatic plane is still $2r$. For a square distribution, the relationship between L_{max} and L_{min} becomes $L_{max} + t = L_{min} + 2\bar{r}$, with:

$$N_a = \frac{1}{(L_{max}+t)(L_{min}+2\bar{r})} = N_v 2r \qquad (5.10)$$

We can then derive the effective particle spacing:

$$L_{min} = \sqrt{\frac{\pi r t}{2f_v}} - 2\bar{r} \qquad (5.11)$$

For triangular distribution, the centre to centre spacing becomes:

$$L = \sqrt{\frac{\pi r t}{\sqrt{3} f_v}} \qquad (5.12)$$

The effective particle spacing for triangular arrangement is then:

$$L^* = \sqrt{(L\frac{\sqrt{3}}{2} - 2\bar{r})^2 + (L\frac{1}{2} - t)^2} \qquad (5.12)$$

5.2.1.3 Influence of particle arrangement

On the basal plane, the difference between particle spacings for triangular and square arrangements in Eq. (5.3) and (5.4) is a factor that equals to $\sqrt{\frac{2}{\sqrt{3}}}$, which is close to 1, therefore particle arrangements on a basal plane only have s minor influence on the strengthening calculation. However, on a prismatic plane, square and triangular arrangements have a significant impact on the results due to the asymmetrical nature of the precipitate intersection on the prismatic plane. Fig. 5.5 compares the influence of the two arrangements on the particle spacing calculation. Here the precipitates in Mg-4.5Zn alloy aged at 200 ℃ for 12 h are selected as the example condition, where the radius of rod-shaped precipitates is fixed at 5 nm and the number density of precipitates is fixed at 1.35×10^{20} m^{-3} (Table 4.1). The difference between square and triangular arrangements is investigated in a way to calculate the smallest spacing in each arrangement (L_{min} for square and L^* for triangle as in Fig. 5.3) in relation to the length of particle. All values are divided by the particle centre to centre distance (L) to show the relative importance of particle shape and positioning.

As shown in Fig 5.5, the precipitate spacings calculated from square and triangular arrangements are close when the length-to-L ratio is close to 0. In this situation, the particle centre to centre distance is significantly larger than the rod length, so the influence from particle arrangement is minimum. As the rod goes longer, the L_{min} in square arrangement decreases fast and starts to go below 0 when the rod length is equal to the centre to centre distance. Here the two rods on the top and bottom position of the square grid (Fig. 5.3(a)) start to overlap. The L^* in triangular arrangement, on the other hand, decreases first then starts to increase after reaching a minimum value as the precipitate length increases. The minimum value of L^* is reached when the rod length is equal to the height of the triangle, i.e. $\frac{\sqrt{3}}{2}$ times of the centre to centre distance L, as the rod goes longer the tip to tip distance L^* will increase and is no longer the smallest spacing, the relevant distance becomes the side to side distance between rods which is equal to half of L (minimum value in the curve of triangle arrangement in Fig. 5.5), this is where the triangular spacing saturates.

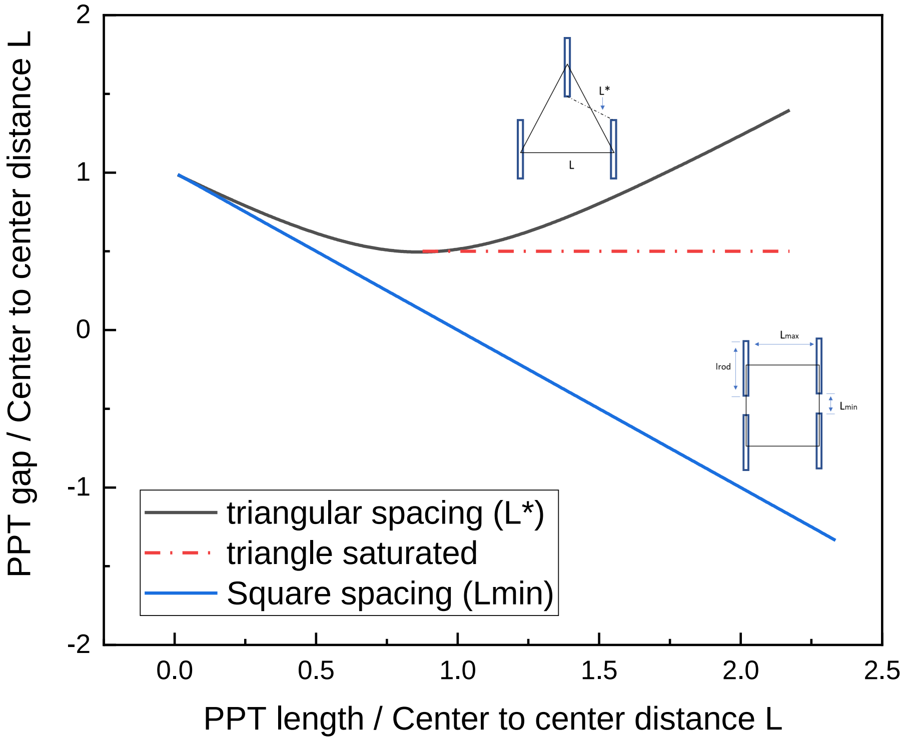

Fig. 5.5 The ratio between precipitate gap (PPT gap) and centre to centre spacing (L) vs The ratio between precipitate length (PPT length) and centre to centre spacing (L) for rod precipitates on prismatic plane.

From Fig. 5.5 it seems that the square arrangement tends to underestimate the spacing calculation especially when the rod is long and will fail when the rod length reaches the centre to centre distance L of particles. In this regard, the triangular arrangement is a better assumption as it provides more stable configurations. Therefore, in the following sections only the triangular arrangement is considered.

With the above information and Eq. (5.8), an upper limit $\frac{\sqrt{3}}{2}L = \frac{1}{2}\sqrt{\frac{\sqrt{3}\pi r l}{f_v}}$ can be determined for the triangular spacing to be saturated for rod-shaped precipitates. When

$l < \frac{1}{2}\sqrt{\frac{\sqrt{3}\pi r l}{f_v}}$, the smallest spacing L^*can be well described by Eq. (5.9). While when $l \geq \frac{1}{2}\sqrt{\frac{\sqrt{3}\pi r l}{f_v}}$, the smallest spacing becomes:

$$L^* = \frac{1}{2}L = \frac{1}{2}\sqrt{\frac{\pi r l}{\sqrt{3} f_v}} \qquad (5.13)$$

Similarly, for plate-shaped precipitates, the upper limit for $\bar{r} = \frac{\pi r}{4}$ becomes $\frac{1}{2}\sqrt{\frac{\sqrt{3}\pi r t}{f_v}}$. When $r \geq 2\sqrt{\frac{\sqrt{3} r t}{\pi f_v}}$, the saturated smallest spacing becomes:

$$L^* = \frac{1}{2}\sqrt{\frac{\pi r t}{\sqrt{3} f_v}} \qquad (5.14)$$

5.2.1.4 CRSS increment due to bypassing and shearing

5.2.1.4.1 On {0001} basal plane

For rod-shaped precipitates, the CRSS increment due to bypassed precipitates with triangular spacing can be obtained by taking Eq. (5.3) into Eq. (3.35):

$$\Delta\tau_{bp} = \frac{2\beta\mu b}{r\sqrt{\frac{2\pi}{\sqrt{3} f_v}} - 2r} \qquad (5.15)$$

Where β is the tension line constant, μ is the shear modulus and b is the Burgers vector of dislocation.

The CRSS increment due to shearing can also be achieved with Eq. (3.43) and (5.2):

$$\Delta\tau_{sh} = \mu\sqrt{\frac{k^3 f_v r}{2b\beta\pi}} \qquad (5.16)$$

Where k is a constant relating to the transition radius between shearing and bypassing.

Due to rods and plates having the same intersection shape and geometry relationships with the basal plane. Eq. (5.15) and (5.16) also apply for plate-shaped precipitates.

5.2.1.4.2 On $\{10\bar{1}0\}$ prismatic plane

For rod precipitates on prismatic planes, the CRSS increment due to bypassing for the triangular arrangement can be obtained with Eq. (3.35), (5.9) and (5.13):

When $l < \frac{1}{2}\sqrt{\frac{\sqrt{3}\pi r l}{f_v}}$:

$$\Delta\tau_{bp} = \frac{2\beta\mu b}{\sqrt{\left(\frac{\sqrt{3}}{2}\sqrt{\frac{\pi r l}{\sqrt{3} f_v}} - l\right)^2 + \left(\frac{1}{2}\sqrt{\frac{\pi r l}{\sqrt{3} f_v}} - \frac{\pi r}{2}\right)^2}} \qquad (5.17)$$

When $l \geq \frac{1}{2}\sqrt{\frac{\sqrt{3}\pi r l}{f_v}}$:

$$\Delta\tau_{bp} = \frac{4\beta\mu b}{\sqrt{\frac{\pi r l}{\sqrt{3} f_v}}} \qquad (5.18)$$

Since the shearing mechanism Eq. (3.43) assumes spherical particles while the rod intersection on prismatic plane is asymmetrical, to calculate the stress increment due to shearing, we can equivalent the intersecting area to a sphere shape with an effective intersect radius. Here the average intersection area of each precipitate can be calculated as:

$$\bar{S} = 2\bar{r}l = 2r\frac{\pi}{4}l \qquad (5.19)$$

And the effective intersect radius is:

$$\bar{r}^* = \sqrt{\frac{\bar{S}}{\pi}} = \sqrt{\frac{rl}{2}} \qquad (5.20)$$

With Eq. (5.6) and (5.17), we can then derive the CRSS increment for shearing by considering Eq. (3.43):

$$\Delta\tau_{sh} = \mu\sqrt{\frac{k^3 f_v}{2b\beta\pi}\sqrt{\frac{rl}{2}}} \qquad (5.21)$$

When precipitates have a plate shape, the CRSS increment due to bypassing for triangular arrangement becomes (Eq. (3.35), (5.12) and (5.14)):

When $r < 2\sqrt{\frac{\sqrt{3}rt}{\pi f_v}}$:

$$\Delta\tau_{bp} = \frac{2\beta\mu b}{\sqrt{\left(\frac{\sqrt{3}}{2}\sqrt{\frac{\pi rt}{\sqrt{3}f_v}}-\frac{\pi r}{2}\right)^2+\left(\frac{1}{2}\sqrt{\frac{\pi rt}{\sqrt{3}f_v}}-t\right)^2}} \qquad (5.22)$$

When $r \geq 2\sqrt{\frac{\sqrt{3}rt}{\pi f_v}}$:

$$\Delta\tau_{bp} = \frac{4\beta\mu b}{\sqrt{\frac{\pi rt}{\sqrt{3}f_v}}} \qquad (5.23)$$

The effective intersect radius becomes:

$$\bar{r}^* = \sqrt{\frac{\bar{S}}{\pi}} = \sqrt{\frac{rt}{2}} \qquad (5.24)$$

And the CRSS increment from shearing becomes:

$$\Delta\tau_{sh} = \mu\sqrt{\frac{k^3 f_v}{2b\beta\pi}\sqrt{\frac{rt}{2}}} \qquad (5.25)$$

5.2.2 Mechanical model for poly-dispersed precipitates

To follow the full strength evolution during ageing, the above models can further be extrapolated to poly-dispersed precipitates by taking into account precipitate size distributions provided by the precipitation model in Section 4.3.

5.2.2.1 On $\{0001\}$ basal plane

For triangular distributed rod-shaped precipitates, the area density of precipitates intersecting the shear plane is now the sum of all size classes in the precipitation model:

$$N_a = \frac{2}{\sqrt{3}L^2} = \sum_i N_{ai} = \sum_i N_i l_i' \qquad (5.26)$$

Where N_{ai}, N_i and l_i' are the area density, number density and probability of intersection in size class i.

This leads to the estimation of the average precipitate centre to centre spacing:

$$L = \sqrt{\frac{2}{\sqrt{3}\sum_i N_i l_i}} \qquad (5.27)$$

Where l_i is the precipitate length in size class i.

At each time step, we assume all precipitates larger than r_c are bypassed and smaller than r_c are sheared. The CRSS increment due to bypassing and shearing are then derived by considering Eq. (3.35) and Eq. (3.43):

$$\tau_{bp} = \frac{2\beta\mu b}{\sqrt{\frac{2}{\sqrt{3}\sum_i N_i l_i}} - 2\frac{\sum_{i>i_c} N_i r_i}{\sum_{i>i_c} N_i}} \qquad (5.28)$$

$$\tau_{sh} = \mu\sqrt{\frac{k^3 \sum_{i<i_c} N_i l_i}{2b\beta}}\left(\frac{\sum_{i<i_c} N_i r_i}{\sum_{i<i_c} N_i}\right)^{\frac{3}{2}} \qquad (5.29)$$

The shape and distribution of plate precipitates on the basal plane are the same as rod precipitates. For poly-dispersed plates, the rod length l can be simply replaced by the plate thickness t:

$$\tau_{bp} = \frac{2\beta\mu b}{\sqrt{\frac{2}{\sqrt{3}\sum_i N_i t_i}} - 2\frac{\sum_{i>i_c} N_i r_i}{\sum_{i>i_c} N_i}} \qquad (5.30)$$

$$\tau_{sh} = \mu\sqrt{\frac{k^3 \sum_{i<i_c} N_i t_i}{2b\beta}}\left(\frac{\sum_{i<i_c} N_i r_i}{\sum_{i<i_c} N_i}\right)^{\frac{3}{2}} \qquad (5.31)$$

5.2.2.2 On $\{10\bar{1}0\}$ prismatic plane

For triangular distributed rod-shaped precipitates on the prismatic plane, the effective intersect radius can be expressed as (Eq. (5.20)):

$$\bar{r_i}^* = \sqrt{\frac{\sum_i N_i r_i l_i}{2\sum_i N_i}} \qquad (5.32)$$

And the area density can be expressed as:

$$N_a = \sum_i N_i 2r_i \qquad (5.33)$$

This gives the CRSS increment due to shearing:

$$\tau_{sh} = \mu\sqrt{\frac{k^3 \sum_{i<i_c} N_i r_i}{b\beta}}\left(\frac{\sum_{i<i_c} N_i r_i l_i}{2\sum_{i<i_c} N_i}\right)^{\frac{3}{4}} \qquad (5.34)$$

And the centre to centre spacing is:

$$L = \sqrt{\frac{2}{\sqrt{3}\sum_i N_i 2r_i}} \qquad (5.35)$$

With Eq. (3.35), (5.9), (5.13) and (5.35) we have the CRSS increment due to bypassing:

When $\frac{\sum_{i>i_c} N_i l_i}{\sum_{i>i_c} N_i} < \sqrt{\frac{\sqrt{3}}{2\sum_i N_{i>i_c} 2r_i}}$:

$$\tau_{bp} = \frac{2\beta\mu b}{\sqrt{\left(\sqrt{\frac{\sqrt{3}}{2\sum_{i>i_c} N_i 2r_i}} - \frac{\sum_{i>i_c} N_i l_i}{\sum_{i>i_c} N_i}\right)^2 + \left(\sqrt{\frac{1}{2\sqrt{3}\sum_{i>i_c} N_i 2r_i}} - \frac{\pi \sum_{i>i_c} N_i r_i}{2\sum_{i>i_c} N_i}\right)^2}} \qquad (5.36)$$

When $\frac{\sum_{i>i_c} N_i l_i}{\sum_{i>i_c} N_i} \geq \sqrt{\frac{\sqrt{3}}{2\sum_{i>i_c} N_i 2r_i}}$:

$$\tau_{bp} = \frac{4\beta\mu b}{\sqrt{\frac{2}{\sqrt{3}\sum_{i>i_c} N_i 2r_i}}} \qquad (5.37)$$

For plate shape precipitates, the effective intersect radius becomes:

$$\bar{r}_i^{\,*} = \sqrt{\frac{\sum_i N_i r_i t_i}{2\sum_i N_i}} \qquad (5.38)$$

The area density and centre to centre spacing can be expressed the same as Eq. (5.33) and (5.35). The CRSS increment due to shearing is therefore:

$$\tau_{sh} = \mu\sqrt{\frac{k^3 \sum_{i<i_c} N_i r_i}{b\beta}}\left(\frac{\sum_{i<i_c} N_i r_i t_i}{2\sum_{i<i_c} N_i}\right)^{\frac{3}{4}} \qquad (5.39)$$

With Eq. (3.35), (5.12), (5.14) and (5.35) we have the CRSS increment due to bypassing:

When $\frac{\sum_{i>i_c} N_i r_i}{\sum_{i>i_c} N_i} < \frac{4}{\pi}\sqrt{\frac{\sqrt{3}}{2\sum_i N_{i>i_c} 2r_i}}$:

$$\tau_{bp} = \frac{2\beta\mu b}{\sqrt{\left(\sqrt{\frac{\sqrt{3}}{2\sum_i N_i 2r_i}} - \frac{\pi\sum_i N_i r_i}{2\sum_i N_i}\right)^2 + \left(\sqrt{\frac{1}{2\sqrt{3}\sum_i N_i 2r_i}} - \frac{\sum_i N_i t_i}{\sum_i N_i}\right)^2}} \qquad (5.40)$$

When $\frac{\sum_{i>i_c} N_i r_i}{\sum_{i>i_c} N_i} \geq \frac{4}{\pi}\sqrt{\frac{\sqrt{3}}{2\sum_i N_{i>i_c} 2r_i}}$, the CRSS increment is the same as Eq. (5.37).

5.2.3 Modelling data input

The parameters used in the model to calculate the strength evolution are summarized in Table 5.1. The precipitate size information is from the precipitation model in Section 4.3. Shearing of precipitates in Mg-Zn alloy is possible and has been reported by Wang *et al*. [180], in which the rod-shaped precipitates with a radius of ~ 5 nm are sheared by basal slip during micropillar compression. However, the study in [180] only accounts for single crystal material which is oriented favourably for basal slip where there is a strong localisation into a shear band. For poly-crystal materials, the amount of shear banding is lower as the deformation is disturbed by grain boundaries and multiple slip modes. As a result, precipitate shearing events due to largely concentrated stresses are less likely to occur when the precipitate radius is ~ 5 nm. Therefore, the transition radius r_c between shearing and bypassing in the current study is proposed between 0 to ~ 5nm, and the value of ~ 1.5 nm is selected as it gives the best fit to represent experimental results. In addition, the constant k can be determined using Eq. (3.44).

Finally, the mechanical model for poly-dispersed precipitates coupled with the precipitation model is incorporated in the PreciSo software, for relevant code see Appendix 8.2.2.

Table 5.1 Parameters used for strength model on slip planes.

Parameters	Value	Reference
β	0.21	[243]
μ (GPa)	17	[220, 224]
r_c (nm)	1.5	fitted
k	0.09	Eq. (3.44)
b (nm)	0.32	[10, 12]

5.2.4 Modelling results

5.2.4.1 CRSS increment

Fig 5.6 shows the evolution of CRSS increment on slip and prismatic planes when aged at 150 ℃ and 200 ℃. It is seen that, overall, the dominant strengthening effect is the bypassing mechanism of rod-shaped Mg_4Zn_7 phase, while shearing of rods and bypassing of plate-shaped $MgZn_2$ phase may take place at early or long ageing times. On the basal plane, when aged at 150 ℃ (Fig. 5.6(a)), the shearing of rod-shaped Mg_4Zn_7 phase seems to dominate the hardening before ~ 27 h, after that the bypassing mechanism gradually takes dominance as the precipitates grow larger. After ageing for ~ 84 h, the CRSS increment from bypassed rod-shaped Mg_4Zn_7 phase starts to drop and the bypassing of plate-shaped $MgZn_2$ phase becomes the dominant mechanism for longer ageing times. It should be noted that the CRSS increment value at peak-ageing (~ 84 h) is an overestimation as the precipitation model underestimated the mean precipitate radius and

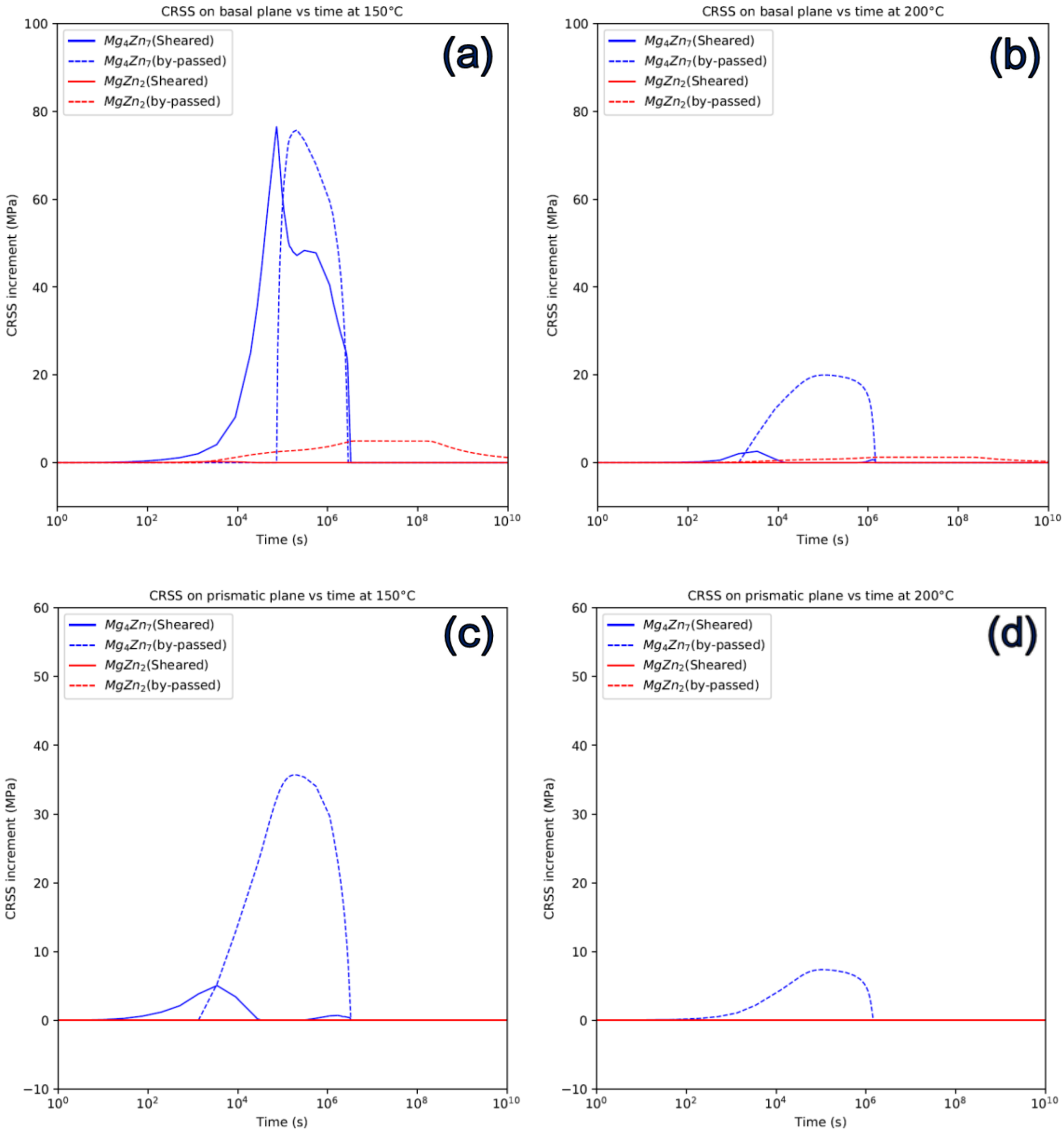

Fig. 5.6 The kinetics of CRSS increment on basal plane when aged at (a) 150 ℃ and (b) 200 ℃, and prismatic plane when aged at (c) 150 ℃ and (d) 200 ℃ in Mg-4.5 Zn alloy.

gives higher precipitate number density than the experimental results (Fig. 4.9). When aged at 200 ℃ (Fig. 5.6 (b)), due to the increased precipitate size, the shearing mechanism only slightly increased the CRSS before ~ 3 h and the bypassing mechanism dominates the strengthening at most ageing stages, the peak CRSS increment is shown as ~ 20 MPa. Bypassing of plate-shaped $MgZn_2$ phase still takes place at the longer ageing time but its strength contribution is small.

On prismatic planes (Fig. 5.6 (c) and (d)), the contribution from the shearing mechanism of plate-shaped $MgZn_2$ phase is almost negligible. The dominant mechanism is the bypassing of rod-shaped Mg_4Zn_7 phase and the total CRSS increment is lower than that on basal plane. This is due to the precipitate intersection area on prismatic plane being significantly larger than the one on basal plane. After peak-ageing, the CRSS increments on the prismatic plane at 150 ℃ and 200 ℃ are ~ 35 MPa and ~ 10 MPa respectively.

5.2.4.2 Comparison with experiments

To compare the strengthening predictions from the current model and experimental values, several extruded samples with different ageing conditions were deformed in tension along the extrusion direction. The obtained yield strengths are compared with the strength model on prismatic plane as it is believed to be the dominant slip mode in this situation [152, 189, 196]. Fig. 5.7 shows the stress-strain curves of extruded Mg-4.5Zn alloys aged at different ageing conditions. It is seen that the yield strength increases with ageing time from ~135 MPa in as-extruded condition to ~221 MPa in peak-aged condition at 150 ℃. And peak-ageing at 200 ℃ comes as the second highest yield strength with a value of ~206 MPa.

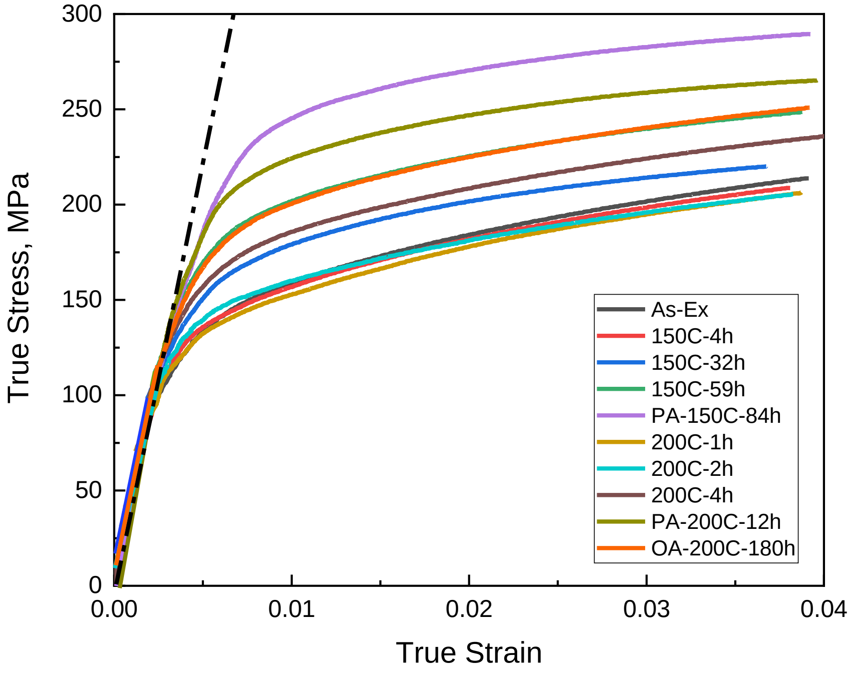

Fig. 5.7 True stress-strain curves in tension along extrusion direction of Mg-4.5Zn samples with different ageing conditions.

The calculation of yield strength from the mechanical model is by relating the resolved shear stress $\Delta\tau$ with the macroscopic stress increase $\Delta\sigma$ and with the Taylor factor M ($\Delta\sigma = M\Delta\tau$), M is related to the stress-based term $\frac{1}{m} = M$, where m is Schmid factor. For prismatic plane, M was measured as 2.22 from the EBSD maps of extruded material (Chapter 6).

The final stress increment is calculated as [201]:

$$\Delta\sigma_{total} = \Delta\sigma_{initial} + \Delta\sigma_{sol} + \Delta\sigma_p \qquad (5.41)$$

Where $\Delta\sigma_{initial}$ is the yield strength of the base material, it includes the forest dislocation contribution and the Hall-Petch effect which should be constant during the ageing process. $\Delta\sigma_{sol}$ is the solid solution strengthening of alloying element which is expressed as [121, 225]:

$$\sigma_{sol} = k_{Zn} X^{Zn_{at}^{2/3}} \qquad (5.42)$$

Where the scaling factor k_{Zn} for Zn has been proposed by Lagowski *et al.* [244] and Somekawa *et al.* [245]: ~30 MPa$/at.\%^{\frac{2}{3}}$.

$\Delta\sigma_p$ is the yield strength increment from precipitates considering both shearing and bypassing mechanisms and different precipitate species:

$$\Delta\sigma_p = \sqrt{(\sigma_{rod})^2 + (\sigma_{plate})^2} \qquad (5.43)$$

$$\Delta\sigma_{(rod\ or\ plate)} = \sqrt{(\sigma_{sh})^2 + (\sigma_{bp})^2} \qquad (5.44)$$

The yield strength of the non-aged sample is used to determine the yield strength of the base material as the yield strength at this condition should be only $\Delta\sigma_{initial} + \Delta\sigma_{sol} \approx 135$ MPa. From the initial Zn concentration using Eq. (5.42), the initial $\Delta\sigma_{sol} \approx 2$ MPa. Therefore $\Delta\sigma_{initial}$ is determined as ~133 MPa.

The yield strength evolutions from prismatic planes at 150 ℃ and 200 ℃ is compared with experimental results in Fig. 5.8. As shown, the predicted yield strength evolution is reasonably close to the experiment at 150 ℃, and the dominant strength contribution is from the bypassing mechanism of rod-shaped precipitates. The modelling kinetics is a bit faster than the experiment due to the high driving force (low surface energy) we chose for the precipitation model (Fig. 4.10). On the other hand, the modelling result at 200 ℃ significantly underestimated the yield strength increment. Two reasons can be considered here: Firstly, the precipitation model assumes a constant rod aspect ratio of ~ 25 which took from the average of all conditions, this might be reasonable for the sample aged at 150 ℃ (with an aspect ratio of ~ 29), but the sample peak-aged at 200 ℃ has a higher aspect ratio of ~ 37 according to the TEM results (Table 4.1), this makes the model underestimate the rod length and consequently overestimate the particle spacing as it is inversely proportional to the rod length (Fig. 5.5). Secondly, the final yield strength might also be contributed by the hardening of basal slip. It is reported that a quarter of the total strain could be attributed by basal slip in this case [189].

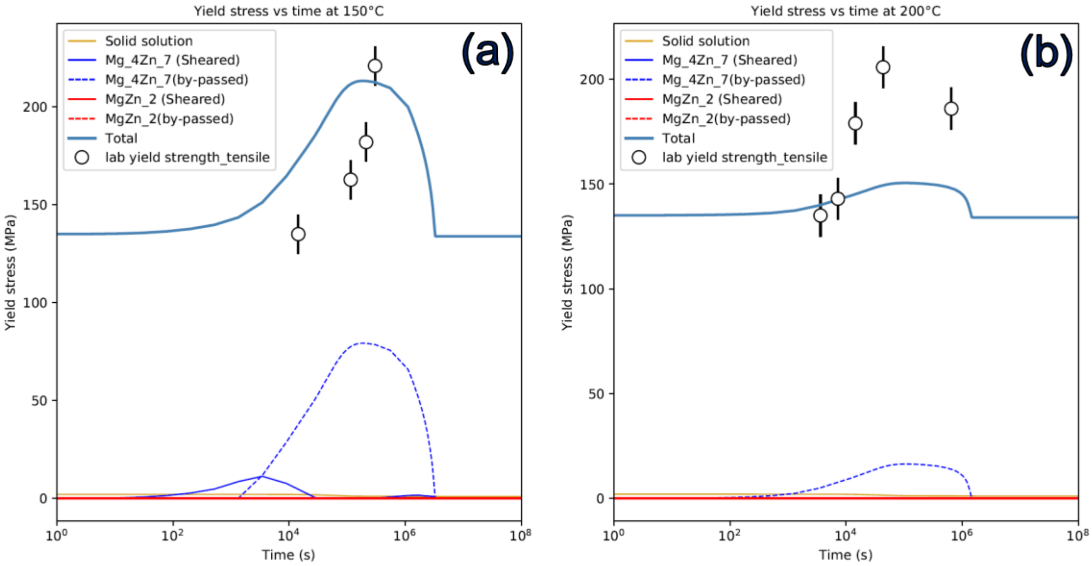

Fig. 5.8 Comparison between simulated kinetics of yield strength on prismatic plane and tensile test results at (a) 150 °C and (b) 200 °C from Fig. 5.7.

5.3 Discussion

5.3.1 Precipitation hardening on basal and prismatic plane

The current study shows that rod-shaped β_1' precipitates have a strong strengthening effect on both basal and prismatic slips. For basal slip, the rod precipitates are the most effective strengthener since there is a high probability of rod precipitates intersecting the basal plane, and the strengthening effect from precipitates is mainly influenced by the radius according to Eq. (5.15). The underestimated radius at 150 °C from Fig. 4.10 gives a much higher CRSS prediction than expected, this highlights the importance of precipitation driving force (surface energy) in effecting strength increment. If correcting the CRSS increment for peak-ageing condition at 150 °C with radius from TEM measurements, the result yields to ~30 MPa, which shows better agreement with the Orowan calculation from literature [12, 196, 210, 246] where the CRSS increment of basal slip in Mg-Zn alloys after ageing at 150 °C or 200 °C falls into ~20-50 MPa. However, the results from the bypassing mechanism in current study and [12, 196, 210, 246] show a higher prediction than what has been observed from experiments [180]. This indicates that Orowan bypassing alone is inadequate in determining the final strength increment and shearing might also play a role. The shearing of rod-shaped precipitates has widely been reported in many other alloys such as Ni [247] and Al [248] but has rarely been shown in Mg-Zn system. Recently, Wang *et al*. [180] observed the shearing of rod-shaped precipitates in Mg-Zn alloy using micropillar compression, it is proposed that the shearing of a particle is crystallographically dictated instead of strength driven. In the present case, basal dislocations have an ideal crystallographic matching to that of a low order plane in rod precipitates, therefore it should be able to shear. Though for poly-crystal material it might be harder to observe the shearing event as the shear on individual slip planes is too small, it is still likely to happen especially at early ageing stage when the precipitates are small. The shearing mechanism for rod precipitates in Mg-Zn alloy has been captured and proposed in the current model and shown in Fig. 5.6.

On prismatic planes, on the other hand, the strength increment is mostly contributed by the bypassing mechanism, as shearing is much harder to happen than that on the basal plane due to the large intersection of rods on prismatic planes. The CRSS increments at peak-ageing at 150 ℃ and 200 ℃ are ~35 MPa and ~10 MPa respectively. In this case, the strength increment is more sensitive to the rod length than the rod radius (Eq. (5.17) and (5.18)) as the rod length has a much higher value than the radius and directly affects the precipitate gap on prismatic plane. The underestimation of the CRSS increment on prismatic planes from the underrated radius in the precipitation model should thus be smaller. This has been proved by comparing the strength increment on prismatic plane with the tensile yield strength from experiment, good agreement is shown at 150 ℃, though at 200 ℃ there is still a large underestimation either due to the smaller aspect ratio we chose for the model or the increased activity from other slip modes.

The current study also reconfirmed the poor strengthening effect from plate-shaped β_2' precipitates on basal and prismatic planes. As shown in Fig. 5.6, plates only show minor strengthening effects on the basal plane at late ageing, this is due to the poor alignment of plates with the basal planes and their intersection probability on basal planes is low. While on prismatic planes the strengthening effect from plates is almost negligible. Though the plates have a good alignment with prismatic planes, the precipitate gap is large due to the extremely low number density (Fig. 4.10).

It should also be noted that all results are influenced by the precipitate size calculated from the previous precipitation model (Section 4.3) which suffers a set of assumptions as discussed in Section 4.4.3. And the solute effect on CRSS is ignored as it is reported to only have a minor influence [249, 250]. But, overall, the current model provides a means of estimates of approximate hardening increments as a function of ageing time and temperature in Mg-Zn alloys.

5.4 Conclusions

In this chapter, the hardening effect of precipitation on slip is discussed through a mechanical model coupled with a precipitation model. The main conclusions are summarized as follows:

1. A mechanical model is developed and coupled with a precipitation model to predict the strength evolution of Mg-Zn alloys during ageing. It is found that rod-shaped β_1' precipitate is the dominant strengthening phase while the strengthening effect from plate-shaped β_2' is very poor.
2. On the basal plane, the shearing mechanism dominates stress increment at early ageing stage, while bypassing mechanism dominates medium ageing stages. For a very long ageing time, the strength is dominated by plate-shaped precipitates.
3. On the prismatic plane, the dominant strengthening mechanism is the bypass of rod-shaped precipitates.
4. The yield strength evolution during ageing can be estimated by considering the hardening of the prismatic plane.

6. Influence of precipitates on twinning in Mg-Zn alloy

6.1 Introduction

Twinning on $\{10\bar{1}2\}$ planes plays a dominant role in determining the plasticity and strength when compressed along extrusion direction [11, 12, 152]. In this chapter, twinning behaviour and resultant mechanical properties under the influence of precipitation in Mg-Zn alloy is investigated. The strengthening of precipitation on twinning plane was first studied by measuring compression yield strengths of alloys with different ageing conditions and described by a strength model. Then the effect of ageing on twin strain contribution is studied by investigating twin fractions and sizes using EBSD analysis, followed by a discussion of the interaction mechanism between precipitates and twinning.

6.2 Results

6.2.1 Compressive deformation

Several compression tests were conducted in the current study with alloys treated at 150 ℃ and 200 ℃ from non-aged to over-aged conditions. Some representative compressive stress-strain curves of selected conditions are shown in Fig. 6.1. Clearly, ageing increased the yield strength of the alloys. The yield plateau (or yield elongation) is observed in all the samples. Notably, the length of the yield elongation decreased in aged samples compare to the non-aged samples. This is believed to be due to the reduced autocatalytic activity of twinning and subsequently lower twin aspect ratio in aged material [216]. The current result also shows that the yield elongation is inversely proportional to the yield strength in Mg-Zn alloys. Table 6.1 summarize the yield stresses of all tested conditions. It can be seen that yield strength increases with ageing time in both temperatures, the maximum strength increment (~ 70 MPa) was observed following peak-ageing at 150 ℃. During peak-ageing at 200 ^{o}C, the strength only increased moderately by ~ 40 MPa but further decreased following over-ageing at 200 ℃.

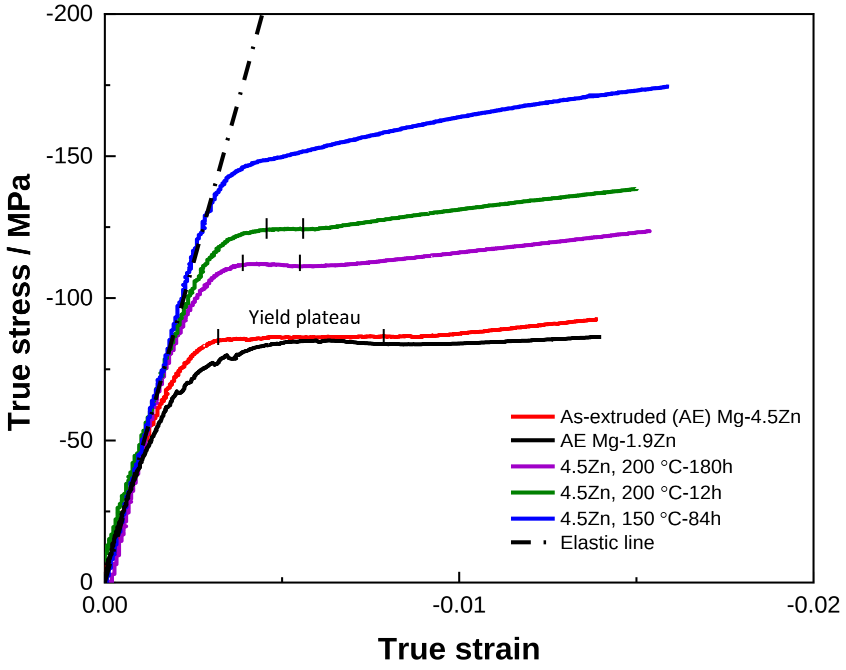

Fig. 6.1 True stress-strain curves in compression along extrusion direction of samples with selected ageing conditions. Tests were halted at an applied plastic train of 0.012

Table 6.1 The 0.2% yield stress of samples with different ageing conditions

Mg-Zn alloys	Conditions	0.2% yield stress, MPa
Mg-1.9Zn	As-extruded (non-aged)	-80 ± 5
Mg-4.5Zn	As-extruded (non-aged)	-85 ± 5
	150 ℃ - 4 h	-85 ± 5
	150 ℃ - 12 h	-85 ± 5
	150 ℃ - 32 h	-98 ± 5
	150 ℃ - 59 h	-125 ± 5
	150 ℃ - 84 h (peak-aged)	-151 ± 5
	200 ℃ - 1 h	-90 ± 5
	200 ℃ - 2 h	-108 ± 5
	200 ℃ - 4 h	-113 ± 5
	200 ℃ - 12 h (peak-aged)	-124 ± 5
	200 ℃ - 180 h (over-aged)	-112 ± 5

6.2.2 Mechanical model for poly-dispersed precipitates on twinning plane

The macroscopic yielding in textured wrought Mg alloys is determined by tensile twinning when compressed perpendicular to c-axis [152]. The evolution of yield strength during ageing can then be modelled by considering the precipitation strengthening on twinning plane. Here a strength model for poly-dispersed precipitates on twinning plane is developed and briefly shown here, for full description readers are referred to Appendix 8.2.2. The principal equation is based on the model proposed by Barnett *et al*. [220] as in Eq. (2.11), with an extra Taylor factor (inverse of Schmid factor m) to relate the yield strength with calculated CRSS:

$$\Delta\sigma_{bp} = \frac{M\tau_0\mu(n'b)^2}{4\pi\sqrt{1-v}\gamma_{twin}L_{twin}}\ln\frac{\bar{D}}{n'b} \qquad (6.1)$$

With:

$$\bar{D} = \frac{2}{L_{twin}^{-1}+(2r)^{-1}} \qquad (6.2)$$

$$n'b = b_0'(\frac{2r}{b})^{\frac{1}{3}} \qquad (6.3)$$

μ is shear modulus, v is Poisson’s ratio, L_{twin} is the particles spacing, γ_{twin} is coherent twin interface energy, $n'b$ is the magnitude of leading super dislocation burgers vector, $\bar{D}$ is the harmonic mean of L_{twin} and particle diameter d, b_0' is an empirical factor, M is Taylor factor.

For poly-dispersed rod precipitates, the key parameters to be determined are $n'b$, L_{twin} and $\bar{D}$. Assume a triangular distribution, and using the same strategy described in Section 5.2.2 and 5.2.4.2 by coupling the Orowan models for twinning and different size classes from the precipitation model, they are:

$$n'b = b_0'(\frac{2\sum_i N_i r_i}{b\sum_i N_i}\sqrt{\frac{1}{\cos\emptyset}})^{\frac{1}{3}} \qquad (6.4)$$

$$L_{twin} = \sqrt{\frac{2}{\sqrt{3}\sum_i N_i(2r_i\sin\emptyset+l_i\cos\emptyset)}} - \frac{2\sum_i N_i r_i}{\sum_i N_i}\sqrt{\frac{1}{\cos\emptyset}} \qquad (6.5)$$

$$\bar{D} = \frac{2}{\left(\sqrt{\frac{2}{\sqrt{3}\sum_i N_i(2r_i\sin\emptyset+l_i\cos\emptyset)}}-\frac{2\sum_i N_i r_i}{\sum_i N_i}\sqrt{\frac{1}{\cos\emptyset}}\right)^{-1}+\left(\frac{2\sum_i N_i r_i}{\sum_i N_i}\sqrt{\frac{1}{\cos\emptyset}}\right)^{-1}} \qquad (6.6)$$

ø is the angle between $\{10\bar{1}2\}$ twinning plane and $\{0001\}$ basal plane, which can be calculated using the lattice structural information. i is the number of each size class.

Bring Eq. (6.4) - (6.6) into Eq. 6.1, the strength increment in each time step can be calculated. The size information of precipitates is the same as calculated in Section 4.2. Parameters for twinning used in the current simulation are shown in Table 6.2 and the corresponding results are shown in Fig. 6.2. As depicted in Fig. 6.2, the simulated yield strength increment agrees well with the experiment results by considering twinning alone. The total yield strength appears to be dominated by the bypass mechanism between twin dislocation and precipitates, with a slight contribution from solid solution. It is also noticeable that the kinetics of modelling results at 150 ℃ is slightly more rapid than the experimental results, this is related to the relatively low surface energy we employed in the precipitation model in the absence of more accurate data (Fig. 4.10).

Table 6.2 Parameters used for twinning strength model.

Parameters	Value	Reference
$\mu\ (GPa)$	17	[220, 224]
v	0.33	[220]
$\gamma_{twin}\ (J/m^2)$	0.12	[220]
b for twin (nm)	0.049	[220]
$\tau_0\ (MPa)$	20	[220]
$b_0'\ (nm)$	0.22	[220]
sin $\emptyset$	0.684	This work
cos $\emptyset$	0.73	
M	2.38	EBSD

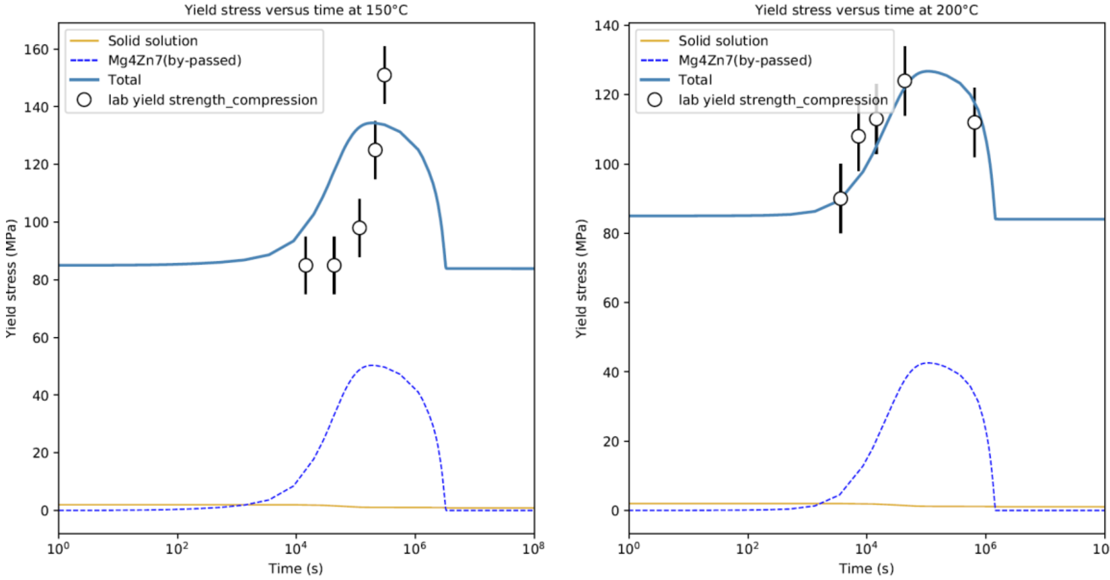

Fig. 6.2 Comparison between simulated kinetics of mechanical properties and compression test results.

There are few limitations to be considered in this model. Since the plate-shaped β_2' precipitates have poor hardening effects (Fig. 5. 6) due to their large radius and small number density (Fig. 4.10), only rod-shaped β_1' precipitates are considered in the current model. And the shearing of precipitates by twin dislocation is ignored since most results in literature [46, 180, 190, 195, 209, 210] show that the rod precipitates are unlikely to be sheared by twin dislocation. But overall the model gives reasonable predictions of the strength evolution during ageing in Mg-Zn alloys.

6.2.3 Influence of precipitates on twinning behaviour

The next question is how ageing effect the strain contribution of twinning at low-strain deformation. This is key information if one needs to simulate the hardening of stress-strain curves or to control the mechanical properties (e.g., yield asymmetry) that are related to twinning. To answer this, a proper understanding of twin fractions at different ageing conditions is required. The following section will thus focus on investigating twinning behaviour in alloys with different ageing conditions through EBSD and discuss the deterministic nature of twinning at low strains of deformation in age-hardened Mg-Zn alloy system.

The alloy used in the current study is a Mg-4.5Zn Alloy. As described in section 3.2, the alloys were homogenized and aged at different temperatures. The selected sample conditions for EBSD study are summarized in Table 6.3 (courtesy of Jun Wang and Mahmoud Reza Ghandehari Ferdowsi). Each EBSD map contains at least 1500 grains.

Table 6.3 Overview of the EBSD data collected for deformed Mg-Zn alloys.

Mg-Zn alloys	Conditions	Applied plastic strain	Scan step size	EBSD map size	Number of maps
Mg-1.9Zn	As-extruded	0.012	0.25 μm	~ 520 μm×420 μm	3
Mg-4.5Zn	As-extruded				7
	150 °C-84 h				4
	200 °C-12 h				4
	200 °C-180 h				3

6.2.3.1 Microstructure

6.2.3.1.1 Initial microstructure

The microstructures of extruded samples are presented in Fig. 6.3. It is shown that both Mg-1.9Zn and Mg-4.5Zn has an average grain size of ~ 20 μm (Fig. 6.3 (a) and (b)). In comparison with the extrusion direction (ED || X) inverse pole figure shown in the inset, the majority of grains are in blue or green colour showing the characteristic extrusion texture (see Fig. 6.3 (c)). The relevant distribution of inclination of c-axis to extrusion direction in a Mg-4.5Zn alloy is depicted in Fig. 6.4. As seen, more than 80% of grains are inclined with a c-axis misorientation spread of about 70-90^{o} from the extrusion direction, which is favourable for tensile twinning during compression along ED.

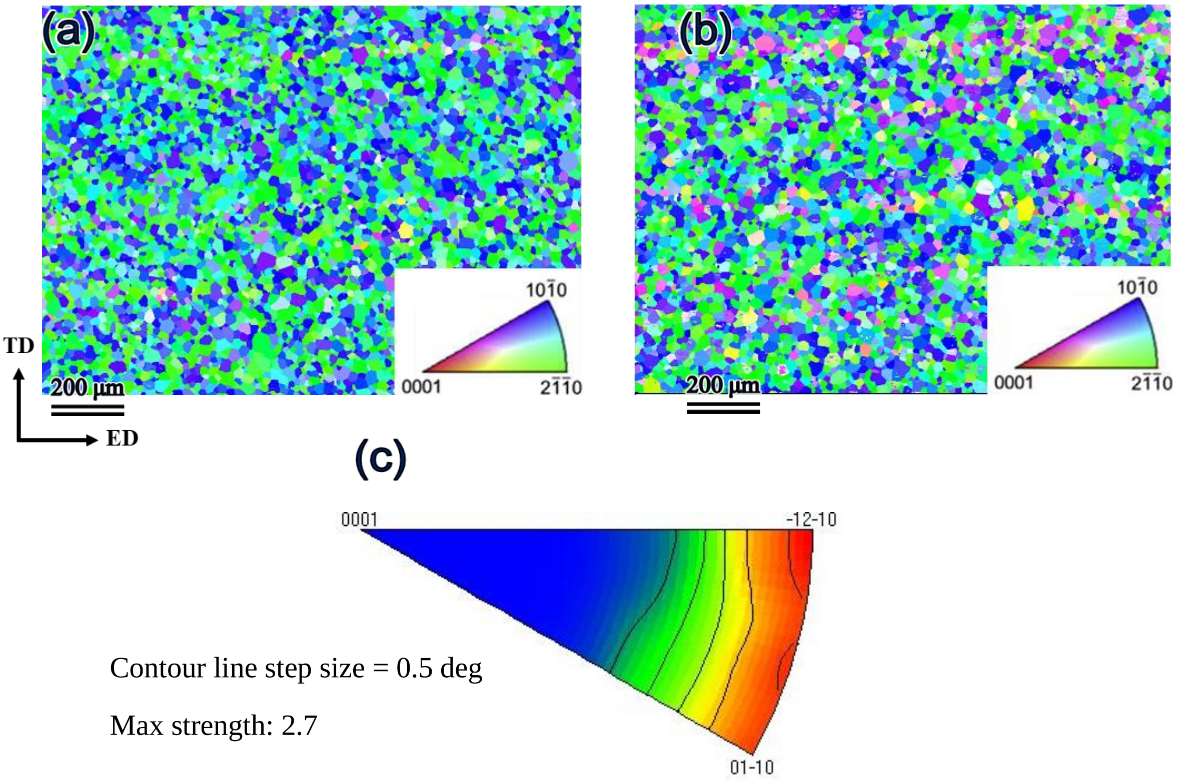

Contour line step size = 0.5 deg

Max strength: 2.7

Fig. 6.3 Microstructures of non-aged as-extruded (a) Mg-1.9Zn and (b) Mg-4.5Zn alloys. The microstructures are colour coded according to the extrusion direction IPF shown in the inset. The extrusion direction is shown in (c) the inverse pole figure of extruded Mg-4.5Zn alloy.

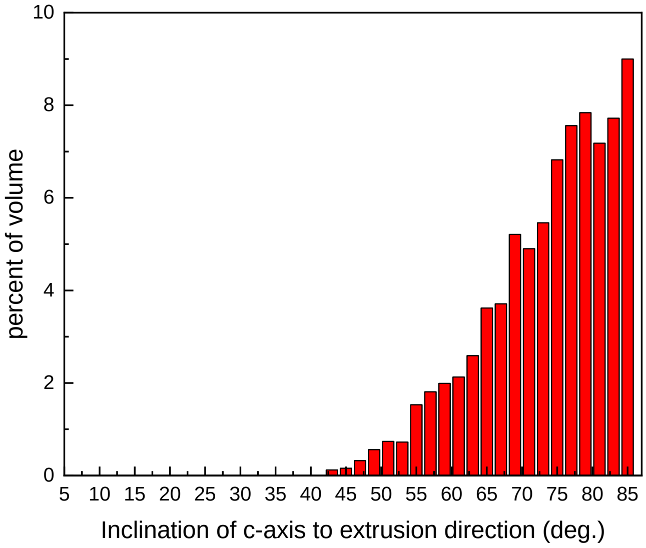

Fig. 6.4 The distribution of c-axis to the extrusion direction in extruded Mg-4.5Zn alloy.

6.2.3.1.2 Twinned microstructure

Fig. 6.5 shows the typical EBSD maps with tensile twins from different ageing conditions deformed to a compressive plastic strain of 0.012. The twins lead to the reorientation of c-axis by ~86.4°, which is identified by red-coloured lenticular regions in the EBSD maps.

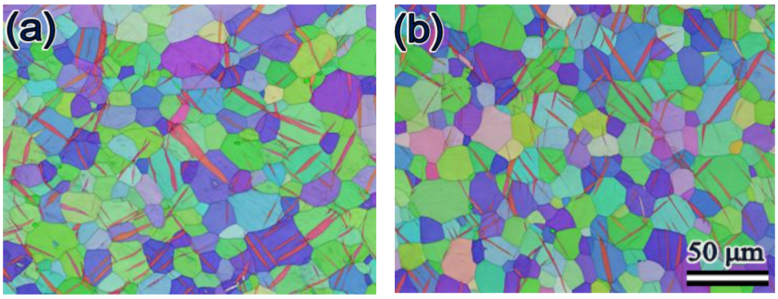

Fig. 6.5 Subsection of EBSD map of (a) extruded Mg-1.9Zn and (b) extruded Mg-4.5Zn, (c) Mg-4.5Zn aged at 150 °C for 84 h, (d) Mg-4.5Zn aged at 200 °C for 12 h and (e) Mg-4.5Zn aged at 200 °C for 180 h. Overlapped maps containing both band contrast and IPF map.

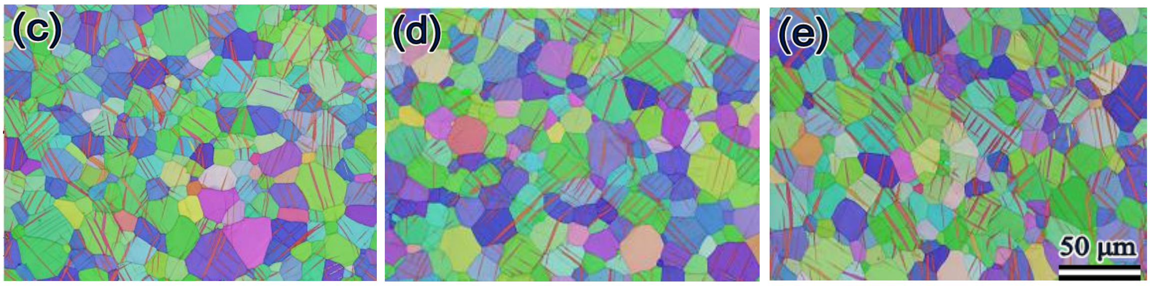

Fig. 6.5 Continued…

Qualitatively it can be seen that the twinned microstructure of the aged alloys (Fig. 6.5 (c) - (f)) show a larger number of thinner twins compared to the twins in as-extruded alloy (Fig. 6.5 (a) and (b)).

6.2.3.2 Twin fraction, aspect ratio and number density

The twin area fraction is calculated using two methodologies following the methods described by Barnett *et al*. [13]. The first method is the orientation analysis through HKL Channel 5 software, where the twin area fractions were obtained by calculating the fraction of twinned grains (coloured red in the extrusion direction, as seen in Fig. 6.5) with c-axis along the extrusion direction in a given map area.

An alternate approach is based on a stereological approach by applying point counting method on the band contrast images to calculate the total twin area fraction. According to the principles of point counting method, a grid of points is placed on the band contrast maps (Fig. 6.6) to determine the number of points intercepting the twin (h_{twin}) and to estimate the proportion of twinning area (P_{twin}), which is given by [251]:

$$P_{twin} \approx \frac{h_{twin}}{N} \tag{6.7}$$

where N is the total points employed. In addition, the twin number density is obtained by counting twin numbers manually from each band contrast map.

To obtain enough statistical significance, at least 1000 points need to be employed in one map [251]. Therefore, all maps in the current study contain more than 1300 points.

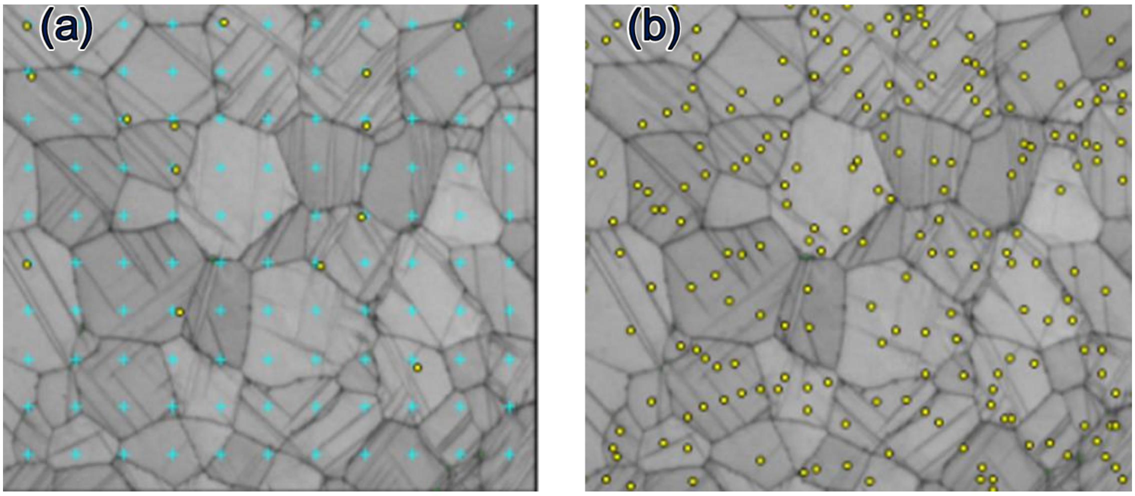

Fig. 6.6 Application of point counting method to band contrast images to determine (a) twin area fraction and (b) twin number density.

The calculated twin area fractions from these two methods are compared in Fig 6.7. Standard errors are evaluated from 3 to 7 maps measured at each condition. Clearly, the twin fractions from the EBSD measurements are underestimated. This is due to the thinner twins that are not indexed due to the relatively coarser step size employed during EBSD measurements. A summary of the average missing twin fractions is given in Table 6.4. Considering the error bars on the actual twin area fractions (Fig 6.7), it is estimated that approximately 0.02 fraction of twins were not indexed in all ageing conditions, except in the peak-aged conditions where the unindexed twin fraction was ~ 4%. In addition, a marginal decrease in twin area fraction is observed due to the increase in the Zn solute from 1.9 to 4.5 wt.%. It is shown that the missed percent of twins is highest in peak-aged samples (~ 50%), while the results in over-aged samples are comparable to that in extruded conditions (~ 25% to ~ 30%). The overall twin area fractions can be roughly divided into two groups, the extruded samples and aged samples. Aged samples exhibit an average increase of twin area fraction of ~ 0.03, which means the aged samples favour twinning in the current case. Specifically, in extruded samples, the twin area fraction in Mg-1.9Zn alloy seems slightly higher than that in Mg-4.5Zn alloy. This points to the solute effect in suppressing twinning. While in aged group, peak-ageing at 150 °C has higher twin area fractions than that of peak-ageing at 200 °C. From peak-ageing to over-ageing at 200 °C, an increase of twin area fraction is observed.

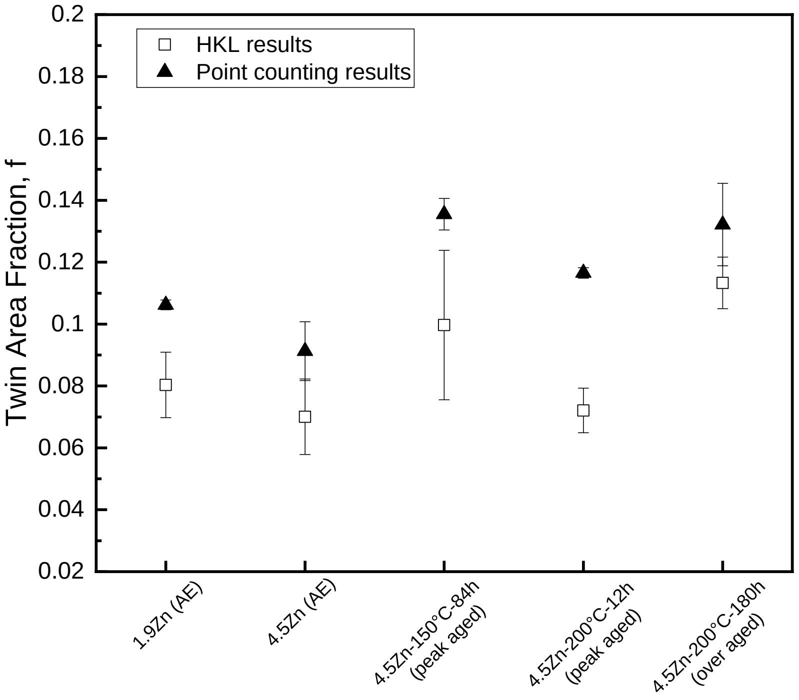

Fig. 6.7 Influence of different ageing conditions on twin area fraction. The blank square and solid triangle represent the results calculated from HKL and point counting method, respectively.

Table 6.4 The missed twin fraction identified by comparing HKL and point counting results for all tested conditions.

Mg-Zn alloys	Conditions	The missed twin fraction, f (missed percent, %)
Mg-1.9Zn	As-extruded	0.026 ± 0.011 (~ 30%)
Mg-4.5Zn	As-extruded	0.021 ± 0.019 (~ 25%)
	150 ℃ - 84 h (peak-aged)	0.039 ± 0.028 (~ 40%)
	200 ℃ - 12 h (peak-aged)	0.045 ± 0.0089 (~ 57%)
	200 ℃ - 180 h (over-aged)	0.023 ± 0.02 (~ 23%)

The number densities of twins are calculated by counting the number of twins in a band contrast map of extruded and aged samples. The total number of twins is then normalized to the measurement area. The twin aspect ratio is measured from EBSD measurements.

As defined by the Eshelby inclusion formalism [176, 216], the aspect ratio is defined by the thickness over the length of the twin. In the channel 5 software, the aspect ratio is obtained by dividing the lengths of minor to major axis of the ellipses fitted to the twins. A cut-off value of twin length > 15 μm is used to account only for the longer twins. These longer twins are most likely to comprise entire rather than fragmented twins and thus provide more reliable twin aspect ratio values. Note that there are approximately 2 - 4 % of thinner twins which are not indexed completely and hence have been omitted from the calculation. Therefore, the current twin aspect ratio is an overestimate.

The overall twin area fraction, aspect ratio and number density are summarized in Table 6.5 for the non-aged and different ageing conditions, results are compared with precipitate volume fraction and solute concentration. Fig. 6.8 shows the aspect ratio and number density of twins as a function of yield stress for the respective conditions.

Table 6.5 Calculated twin area fraction, twin aspect ratio and twin number density of alloys with different ageing conditions in comparison with precipitate volume fraction and solute concentration.

Mg alloy	Ageing conditions	precipitate volume fraction from TEM	Solute concentration from TEP (wt.%)	Twin fraction	Twin aspect ratio (q=t/l)	Twin number density (mm^{-2})
Mg-1.9Zn	As-extruded	0	~1.9	~0.106	~0.128	~ 4324
Mg-4.5Zn	As-extruded	0	~4.5	~0.091	~0.101	~4573
	150 ℃ - 84 h (peak-aged)	β_1': ~ 0.0093	~1.87	~0.135	~0.079	~ 8504
	200 ℃ - 12 h (peak-aged)	β_1': ~ 0.0051	~2.38	~0.116	~0.078	~8111
	200 ℃ - 180 h (over-aged)	β_1': ~ 0.0054 + β_2': ~0.0055	~2.19	~0.132	~0.093	~7667

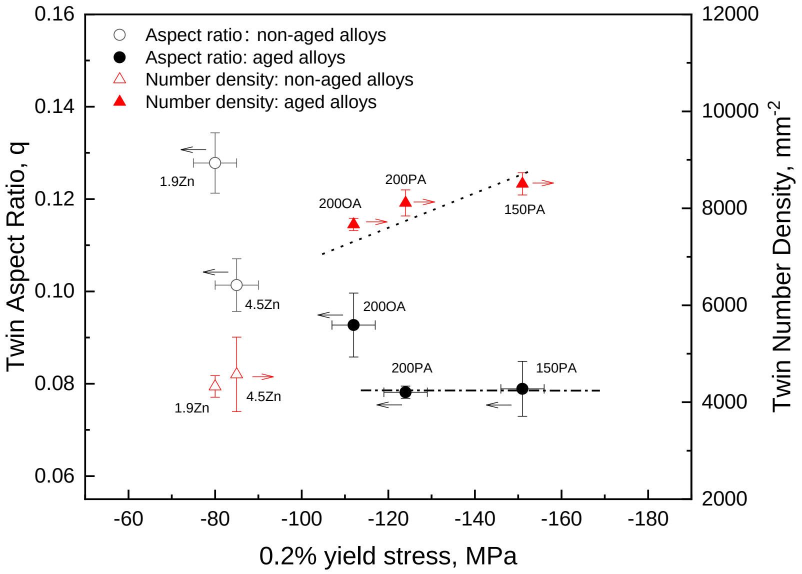

Fig. 6.8 Twin aspect ratio and twin number density against 0.2% yield stress in alloys with different ageing conditions. 200OA, 200PA and 150PA represent over-ageing at 200 °C, peak-ageing at 200 °C and peak-ageing at 150 °C, respectively.

Combining Fig. 6.7, Table 6.5 and Fig. 6.8, following observations can be made:

- Twin number density.

It is found that the influence of solute change on the twin number density is minor if comparing non-aged Mg-1.9Zn and Mg-4.5Zn sample, while ageing increased the twin number density by ~ 85% with the average value increasing from ~ 4500 mm^{-2} to ~ 8300 mm^{-2}. In aged group, the average value of twin number density linearly increases with the rise of measured yield stress.

- Twin aspect ratio.

A decrease in the twin aspect ratio is seen with the increase in solute concentration from 1.9wt.% to 4.5wt.% Zn. Also, when comparing non-aged Mg-1.9Zn alloy and Mg-4.5Zn alloy peak aged at 150 °C (they have close remaining Zn concentration), the twin aspect ratio significantly dropped with the presence of rod-shaped β_1' precipitates. These are the evidence that both solute and β_1' precipitates play a role in restricting twin lateral growth, which is probably due to increased lattice friction [176].

The twin aspect ratio is decreased in peak-aged and over-aged alloy by 20% and 5% respectively compared to that in non-aged Mg-4.5Zn alloy. Whereas in the aged group of alloys, the twin aspect ratio change is within the error except in the case of over-aged alloy.

- Twin fraction

Summarizing from the above information, ageing effects on twin fractions are proposed as follows. Firstly, a direct suppression effect of solute on twin fraction can be found when comparing non-aged Mg-1.9Zn and Mg-4.5Zn samples, this is mostly due to the reduced twin size (lower aspect ratio). Secondly, comparing non-aged Mg-1.9Zn alloy and Mg-4.5Zn alloy peak-aged at 150 ℃, the presence of precipitates increased twin fraction by greatly promoting the twin number density, despite the reduced twin aspect ratio. Thirdly, from peak-ageing to over-ageing at 200 ℃, the twin fraction increased with thickened twins and reduced twin number density.

6.2.3.4 Orientation effect

To investigate the effect of parent grain orientation on the twinning fraction, the parent grains in the deformed microstructure are partitioned into subsets based on the twin Schmid factor (SF). The EBSD maps are processed according to the process described by Barnett et. al. [13]. Firstly, the maps were cleaned following the standard cleaning procedures in Channel 5 software (removing spikes and performing one iteration of dilatation). The cleaned band contrast map and inverse pole figure (IPF) map colour coded according to ED and IPF are shown in Fig. 6.9 (a) and (b) respectively. A subset of twins is created by selecting all the twins with their c-axis oriented parallel to the extrusion direction within a spread of 50° (Fig. 6.9 (c)). The SF of the parent grain orientations corresponding to the selected twins were obtained by replacing the twins with the respective parent grain orientations using the subset functions in Channel 5 software. The obtained map of parent grain orientations is shown in Fig. 6.9 (d). The subset of separated twins (Fig. 6.9 (c)) was then reapplied to this map to obtain a twinned region filled with parent orientation (Fig. 6.9 (e)). From the orientations in Fig. 6.9 (e), the SF for twinning is calculated. Fig. 6.9 (f) shows the band contrast map by removing the regions of twinned part. This map reveals some twins that are not indexed and whose fractions are identified in Table. 6.4.

The area fractions of the indexed twins are then plotted for bins of SFs as shown in Fig. 6.10 for all tested conditions. The fraction of grains with SF less than 0.2 are ignored due to the strong texture in the current extruded alloy. It is clearly seen from the figure that

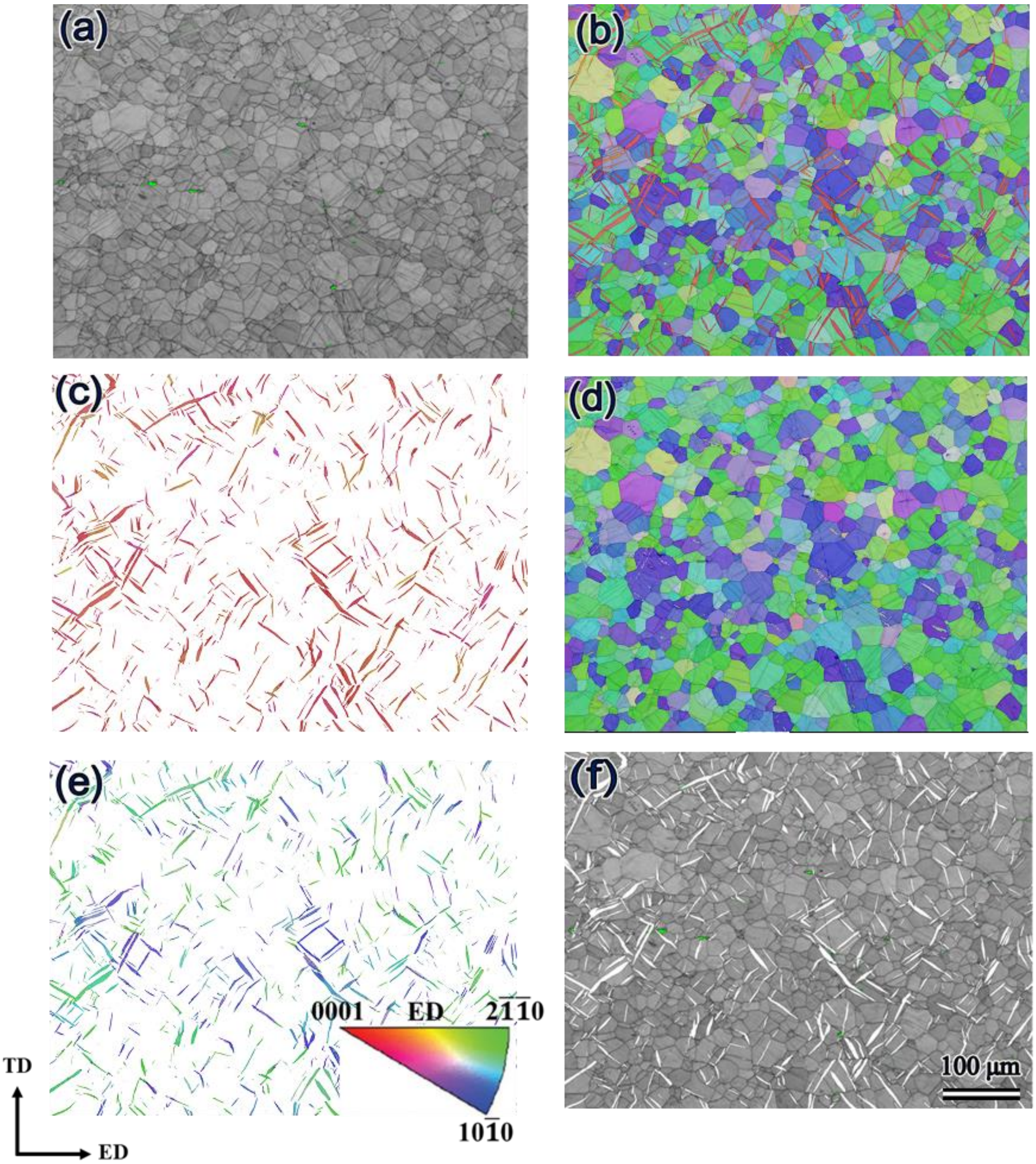

Fig. 6.9 The processing steps of EBSD data. (a) Default band contrast map, (b) EBSD data coloured based on the orientation, (c) twins extracted based on their orientation and morphology, (d) reconstructed map with the twinning area filled with parent orientation, (e) reapply the twin subset to obtain a twinning area composed of parent orientation and (f) extract the twinning area from band contrast map to highlight the unindexed twins.

the twin area fraction increased steadily with the increase in parent grain SF. This indicates that the twins are more probable in grains with high SF. However, twins were also formed in grains with low SF.

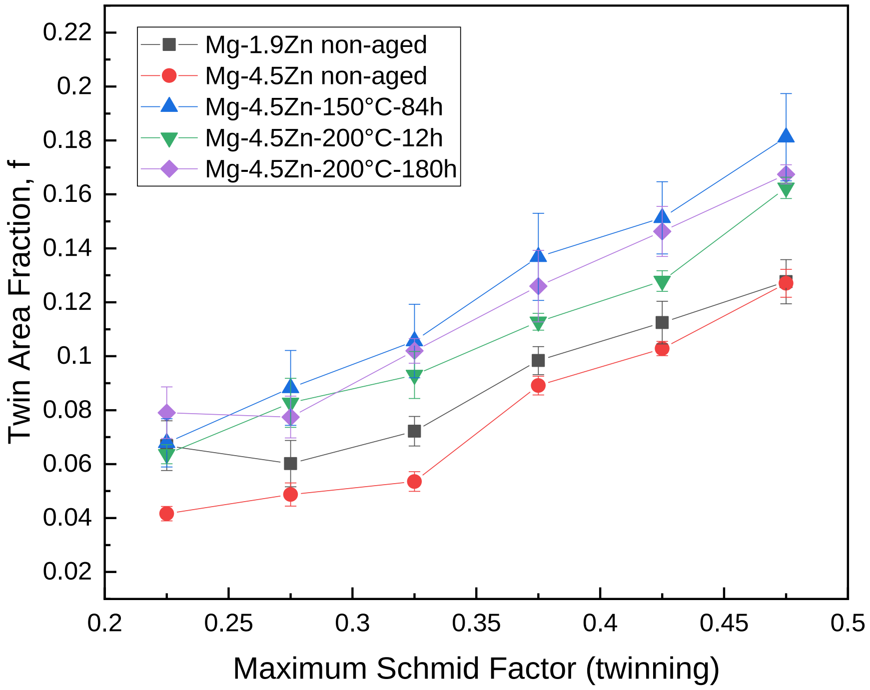

Fig. 6.10 Influence of maximum Schmid Factor for twinning on twin area fraction in samples with different ageing conditions

From the changes in the twin area fraction with SF data, the following observations were made:

- The mean twin fraction in non-aged Mg-4.5Zn alloy is lower than its counterpart Mg-1.9Zn alloy in all SF classes.
- The twin fractions in aged alloys are higher than that of non-aged alloys in all SF regions. This highlights the influence of precipitation in promoting twinning.
- The peak-aged condition at 150 °C exhibited a higher twin fraction amongst all the aged conditions followed by over-ageing and peak-ageing at 200 °C in high SF bins, while in lower SF bins the twin fraction for all aged conditions are comparable to each other.

6.2 Discussion

From the above results, we can see the direct influences of precipitates on the current aged alloys, which are: 1. Reduction in yield elongation with an increase in yield strength. 2. Reduced twin aspect ratio and 3. Increase in twin number density. These results are confirmed by various researchers [11, 197, 209, 216, 217, 252]. The current results further highlight the role of solute concentration and precipitates in the Mg matrix to explain variations in twin fractions. The following sections will discuss the mechanisms of how precipitation influences twinning behaviour during ageing.

6.2.1 Influence of precipitation on twin number density

Twin nucleation has a stochastic nature and is usually initiated at grain boundaries or pre-existing twin surfaces. However, it is widely reported in the literature that regions with high stress concentration have a higher probability for twins to nucleate [10, 213, 215]. The presence of precipitates in the aged alloys postpones plasticity to higher stresses. This evidently affects the propagation step more than the nucleation step so that once the stress for propagation is attained, there is a high number density of incipient nuclei available to propagate. To sum up, twin nucleation is a stress-stimulated process and therefore the twin number density is a direct result of the precipitate hardening effect. This explains the fact that twin number density has a strong relationship with yield strength but is not necessarily proportional to precipitate volume fraction.

6.2.2 Influence of precipitation on twin aspect ratio

The twin aspect ratio is influenced by two twinning processes: 1. twin propagation which determines the length of twin and 2. twin thickening which determines the thickness of twin. The current study shows that precipitation has little influence on twin length as most twins were observed to stop at grain boundaries or other twin boundaries (Fig. 6.5). But the observed lower twin aspect ratio after ageing may indicate that the average thickening rate for each twin has been lowered by precipitation.

Barnett *et al*. [176] have proposed a modified Elshelby approach to obtain the twin aspect ratio for a stable twin with imposed shear stress [176, 216] (in the case of plastic strain < 0.2):

$$\frac{1}{q} = \frac{2sG\beta'}{\tau - \tau_G^*} - \frac{11}{5} \tag{6.8}$$

Where G is shear modulus, s is twinning shear, q is the aspect ratio of twins, τ_G^* is friction stress for twin growth, τ is applied shear stress resolved on twin shear system and β' is a relaxation factor < 1, which reflects the relaxation of constraint placed on twin by surrounding matrix. Note that this equation is only applicable when the applied shear stress is substantially larger than the friction stress on twinning.

According to this approach, two factors that contribute to the lower twin aspect ratio are: 1. a higher value of friction stress for twin growth (higher τ_G^*) and 2. hardening of relaxation mechanisms (higher β'). Assuming no hardening of relaxation, Wang *et al.* [216] estimated the upper limit friction stress for peak-aged Mg-Zn alloy to be approximately 50 - 56 MPa, which is significantly higher than the value obtained for non-aged alloy (5 - 15 MPa). Consequently, thinner twins are expected in aged alloys. The current study further highlighted that the increase of solute and precipitate volume fraction will restrict twin growth as solute and coherent parts of precipitates could enhance the lattice friction stresses.

On the other hand, it is worth noting that twinning event causes high stresses at twin tips which can be relaxed by slip or continuous twinning. Since precipitation produces considerable hardening on both basal and prismatic slips (Section 5.2.4), the plastic relaxation mechanisms can be therefore hindered. And the decreased twin aspect ratio after ageing could be due to both increased friction stresses and hardening of relaxation mechanisms.

6.2.3 The evolution of twin fraction during ageing

From above the following observations can be made:

1. In non-aged group, when Zn solute concentration is increased from 1.9 wt.% to 4.5 wt.%, the twin aspect ratio decreased by ~ 21% because of increased lattice friction stress. While the twin number density only increased by ~ 5% due to the limited hardening effect from solid solution. This results in a lower total twin area fraction.

2. In the case of Mg-4.5Zn, after peak-ageing at 150 °C, the presence of β_1' precipitates greatly increased friction stress and/or hardened relaxation mechanisms which supersedes the effect of Zn solute depletion, leading to a reduction of twin aspect ratio by ~ 22%. However, the twin number density significantly increased by ~ 85% because of peak precipitation hardening. This led to an overall increase of twin area fraction by ~ 48%.
3. Increasing the peak-ageing temperature from 150 °C to 200 °C lowered the volume fraction of β_1' precipitates by ~ 45%. The decreased precipitate volume fraction has the tendency to increase the twin aspect ratio, such impact is competing with the restricting effect from the increased Zn solute (by ~ 27%) on twin aspect ratio. Eventually, the twin aspect ratios between the two temperatures fall in a similar range. But the larger precipitate size and decreased precipitate volume fraction at 200 °C led to a lower yield strength and hence the twin number density is decreased by ~ 5%. The overall twin area fraction is decreased by ~ 14% at this stage.
4. An interesting case is seen in over-aged condition at 200 °C, when compared with peak-ageing at 200 °C, where a large fraction of plate-shaped β_2' precipitates (comparable to the volume fraction of rod-shaped β_1' precipitates) has formed. The twin aspect ratio increased by ~ 19% with the increase in total precipitate volume fraction, which contradicts the phenomenon observed in peak-aged conditions where the twin aspect ratio decreases with the increased precipitate volume fraction. A possible explanation is that both precipitates have become relatively large and lost their coherency at this condition, and their effect on lattice friction stress has become minimum. The increased twin aspect ratio therefore mainly results from the solute depletion. Similarly, the coarsening of β_1' precipitates and the large size of β_2' precipitates has lowered stress and the twin number density (by ~ 5%). In the end, the overall twin area fraction increased by ~ 17%.

It is also interesting to note that the twin fractions in aged samples increased by almost similar amounts in all SF bins (Fig. 6.10). Twinning is more probable in the high SF region. However, due to the stochastic nature of twinning, it also activates in the low SF region [158]. The influence of precipitates on twinning fractions therefore can be best visualised by comparing the twin fractions in those two regions. The twin fractions in Fig.

6.10 are replotted by taking averages of twin fractions in the low SF class (0.225 – 0.275) and the high SF class (0.425 - 0.475). The results are presented in Fig. 6.11. As shown, the twin fraction in the low SF class increased from 0.05 ± 0.01 in non-aged samples to 0.08 ± 0.01 in aged samples, corresponding to a rise of ~ 60%. At the same time in the high SF class, the twin area fraction increased by 0.04 ± 0.02, corresponding to a more modest increment of ~ 33%.

It is known that grains with low SF for twinning have high SF for slip [13], therefore theoretically slip is more favourable to be initiated in these areas instead of twinning. However, current results show that twinning in areas with low SF for twinning proportionally increased more than those in high SF areas by the presence of precipitates. This indicates that slip is hardened more by precipitates than twinning in the present system. Twin fractions in the low SF class thus receive more promotion to accommodate deformation.

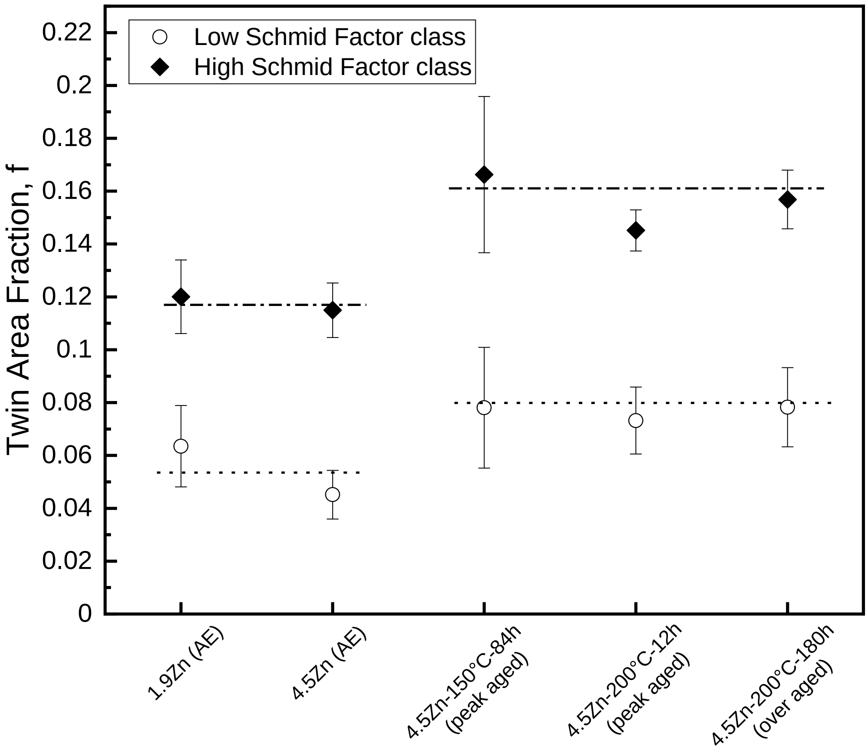

Fig. 6.11 Averaged twin area fraction in grain class with low Schmid Factor for twinning (0.225 – 0.275) and high Schmid Factor for twinning (0.425 - 0.475) in all tested conditions.

6.2.4 Influence of ageing on contribution of twinning strain

In the present case, for strain up to 0.015, the contribution of the twinning shear to the uniaxial strain ε_t can be given as [253]:

$$\varepsilon_t = m\,\gamma\,F \tag{6.9}$$

where m (= 0.45, estimated from EBSD data as in Fig. 6.5) is the average SF for twinning, γ (= 0.13) is the twinning shear and F is the twin fraction.

The calculated results for non-aged and aged Mg-4.5Zn are summarized in Fig. 6.12. Clearly, the non-aged alloy shows ~ 45% strain contribution. This is in close agreement with that reported in the case of AZ31 alloy deformed to a strain of 0.011 [13]. The rest of the strain can therefore be ascribed to basal and prismatic slip. The contribution of twinning strain increased to 58 – 65 % of total plastic strain in the current aged alloys. Such an increase in the contribution of twinning strain reconfirms the higher hardening of slip over twinning in aged Mg-Zn alloys [10, 195].

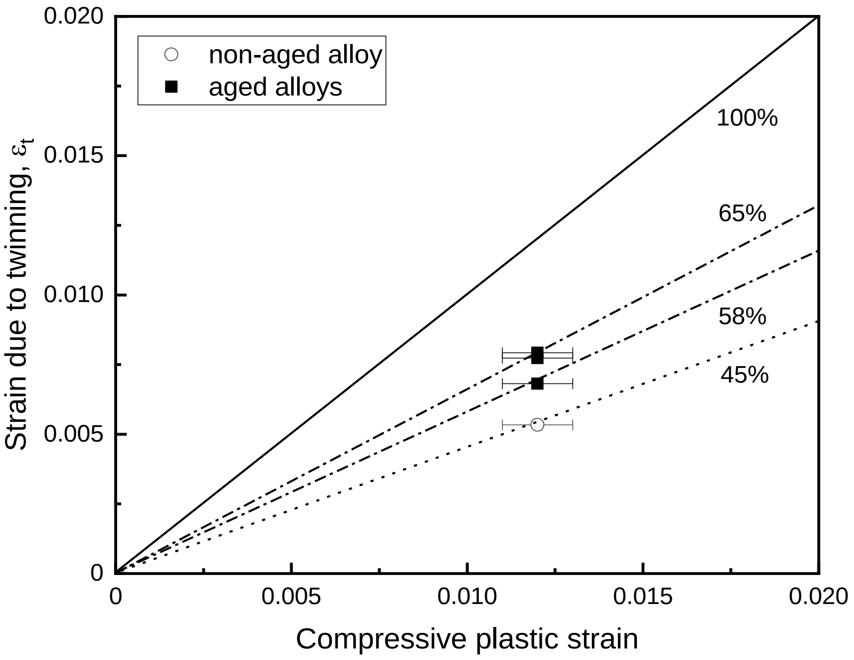

Fig. 6.12 Influence of ageing treatment on the contribution of twinning to the applied axial strain.

6.2.5 Influence of ageing on stress-strain response

From the results and the above discussion, it is evident that ageing not only hardens dislocations on the twinning plane, which led to a direct increase in 0.2% yield stress, but also increased twin fractions with higher twin number density and lower twin aspect ratio. One consequence is the reduced yield plateau in aged alloys. The values of yield elongations of samples with different ageing conditions are summarized in Table 6.6 from Fig.6.1. It shows that the yield elongation decreases with increased Zn solute and decreases after ageing.

Table 6.6 Values of yield elongations of samples with different conditions.

Mg alloy	Ageing conditions	Yield elongation
Mg-1.9Zn	As-extruded	~0.006
Mg-4.5Zn	As-extruded	~0.004
	150 ℃ - 84 h (peak-aged)	0
	200 ℃ - 12 h (peak-aged)	~0.001
	200 ℃ - 180 h (over-aged)	~0.002

Wang *et al*. [216] proposed that there are two criteria to be met for a distinct yield plateau: 1. An autocatalytic twin propagation. This means twins in one grain should be able to stimulate twinning in the neighbouring grain. 2. A considerable twin aspect ratio to provide a detectable level of strain. In the current study, the autocatalytic twin cascade can be indexed as connected twins on EBSD maps. Fig.6.13 shows the fraction of connected twins in comparison to the twin aspect ratio for samples with different Zn levels and ageing conditions. It is seen that, in non-aged group, the twin aspect ratio dropped while the fraction of connected twins has little change when increasing the Zn solute from 1.9 wt.% to 4.5 wt.%, this directly point to the fact that the decreased twin aspect ratio is responsible for the reduced yield elongation. After ageing, both the twin aspect ratio and fraction of connected twins decreased, which leads to a smaller contribution of initial twin cascade to the microscopic strain near yielding and consequently a smaller yield plateau is observed in all aged groups.

The importance of twin aspect ratio in effecting yield elongation has been discussed elsewhere [216]. This work further highlighted the role of connected twins in influencing yield elongation. When comparing peak-aged conditions at 150 ℃ and 200 ℃, where they have similar twin aspect ratios, the yield elongation of peak-aged sample at 150 ℃ almost disappeared while the peak-aged sample at 200 ℃ still shows a small yield elongation. This might relate to the lower fraction of connected twins in 150 ℃ peak-ageing condition. In the previous study [216], the number density of connected twins is approximately one twin per grain [254] and does not seem to be affected by ageing [216], the lower fraction of connected twins (which can propagate at constant stress) is mainly due to the increased strain contribution from randomly nucleated twins. Those random twins nucleate at higher stress and therefore reduce yield elongation caused by the initial twin cascade. Lastly, after over-ageing at 200 °C, both the twin aspect ratio and fraction of connected twins are increased due to the coarsening of precipitates and solute depletion, resulting in a larger yield plateau.

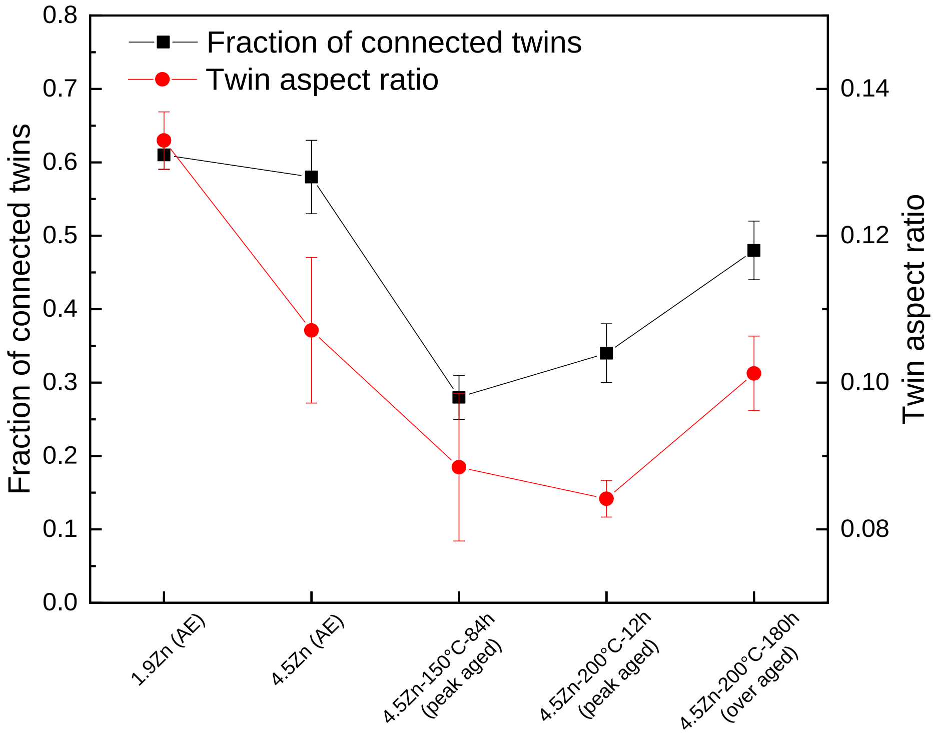

Fig. 6.13 Fraction of connected twins and twin aspect ratio for samples with different ageing conditions compressed to the plastic strain of 0.012.

6.3 Conclusions

In this chapter, the impact of precipitation on the hardening of twinning plane and twinning behaviour is investigated using a mechanical model and EBSD analysis. The main conclusion of this chapter is drawn as follows:

1. Ageing increased the yield strength and reduced the yield plateau in stress-strain curves. A mechanical model for poly-dispersed precipitates on the twinning plane is proposed and gives good prediction on strength evolution in compression along extrusion direction during ageing.
2. A method combined with EBSD analysis and point counting is employed to quantitatively study the influence of ageing conditions on twinning in a Mg-Zn alloy. Compared to the non-aged sample, aged samples show a simultaneous increment of compressive yield stress and twin fraction. Specifically, the peak-aged condition at 150 ℃ shows the maximum increase of 0.2% yield stress and twin fraction, whereas the over-aged condition at 200 ℃ shows the lowest increment of 0.2% yield stress but the second largest twin fraction.
3. Twins in aged samples have a smaller aspect ratio and higher number density compared to the non-aged ones. The current study reconfirms that the increase of solute and precipitates volume fraction have strong effects on twin growth but marginal effects on twin nucleation. The increased twin number density after ageing is believed to be due to the higher stress concentration caused by precipitation hardening.
4. The evolution of twin fraction during ageing is proposed. From non-ageing to peak-ageing conditions, the twin fraction increased with higher twin number density and lower twin aspect ratio. While from peak-ageing to over-ageing conditions, the twin fraction increased but with lower twin number density and higher twin aspect ratio, this is probably due to the coarsened precipitates having lower hardening effects. Twin fractions in all Maximum SF for Twinning bins are promoted by ageing, this increment is even higher in grains with low Maximum SF for twinning (0.225 to 0.35). It is therefore confirmed that the slip systems are hardened more by precipitates over twinning in the present system.

5. Ageing treatment increased the contribution of twinning to the applied axial strain, this reconfirms the stronger hardening of slip over twining in aged Mg-4.5Zn alloys.
6. Yield elongation is reduced after ageing. This is due to ageing decreased the twin aspect ratio and fraction of connected twins, the strain contribution from connected twins in aged alloys is thus lower than non-aged ones.

7. Contributions to original knowledge and future work

7.1 Contributions to original knowledge

In this thesis, a comprehensive study on the precipitation kinetics and strengthening on slip and twinning in Mg-Zn alloys through a combination of experiment and modelling was performed. A thorough theory link between heat treatment, microstructure and property for Mg-Zn alloys is established and can be used to guide Mg alloy design in terms of condition selection and property control. In what follows the key contributions to original knowledge from this thesis are highlighted.

- The microstructural evolutions of β_1' and β_2' precipitates in Mg-Zn alloys are characterized and described in detail through a combination of different techniques and a KWN-type precipitation model. A TTT diagram for these two precipitate species is proposed for the current system.

- Experimental and simulation results show that in Mg-Zn alloys the rod-shaped β_1' dominates the precipitation at early ageing stages, while plate-shaped β_2' starts to form after ~ 84 h at 150 ℃ and ~ 12 h at 200 ℃ and takes the dominance for the longer ageing time. The solid solubilities of Zn in Mg in the Mg-Zn alloys from this study at 150 ℃ and 200 ℃ were found to be lower than those in the Mg-Zn phase diagram in databases (THERMOCALC, PANDAT and KNOVEL).

- A mechanical model is developed and coupled with the precipitation model to predict the strength evolution of Mg-Zn alloys during ageing. The modelling results show that rod-shaped β_1' precipitate is the dominant strengthening phase while the strengthening effect from plate-shaped β_2' is very poor.
- For the precipitation hardening on basal plane, the shearing mechanism of rod-shaped precipitates dominates stress increment at early ageing stage, while bypass mechanism of rod-shaped precipitates dominates intermediate ageing stages. For a very long ageing time the strengthening is dominated by bypassed plate-shaped precipitates. For the precipitation hardening on prismatic plane, the dominant strengthening mechanism across all ageing stages is the bypass of rod-shaped precipitates. The yield strength evolution during ageing is reasonably predicted by considering the precipitation hardening on prismatic plane.

- Ageing increased the yield strength and reduced yield plateau in stress-strain curves of compression along extrusion direction. The decreased yield elongation is due to decreased twin aspect ratio and fraction of connected twins upon ageing, the strain contribution from connected twins in aged alloys is thus lower than non-aged ones.
- A mechanical model for precipitation hardening on twinning plane with poly-dispersed precipitate sizes is proposed and gives a good prediction on strength evolution in compression along extrusion direction during ageing. It is suggested that the bypassing of rod-shaped precipitates is the dominant strengthening mechanism.
- Compared to the non-aged sample, aged samples show a simultaneous increment of compressive yield stress and twin fraction. Specifically, the peak-aged condition at 150 ℃ shows the maximum increase of 0.2% yield stress and twin fraction, whereas the over-aged condition at 200 ℃ shows the lowest increment of 0.2% yield stress but second largest twin fraction.
- Twins in aged samples have smaller aspect ratios and higher number densities than those in the non-aged sample. The current study reconfirms that the increase of solute and precipitates volume fraction have strong effects on twin growth but marginal effects on twin nucleation. The increased twin number density after ageing is believed to be due to the higher stress levels caused by precipitation hardening, which favours a higher number density of nucleation sites.
- Twin fractions in all Maximum SF for Twinning bins are promoted by ageing. This increment is higher in grains with low Maximum SF for twinning (0.225 to 0.35). It is therefore further shown that the slip systems are hardened more by precipitates than twinning.

7.2 Recommendations for future work

While this study has revealed the precipitation kinetics of strengthening phases in Mg-Zn alloys and their impact on slip and twinning, it has also raised some additional questions and potential valuable work for a better understanding of this topic, some of them are outlined below:

- It is recommended to investigate the intrinsic influence of precipitates on lattice parameters and TEP signal in the current system.
- Experiments have shown that there is a possibility of the coexistence of Mg_4Zn_7 and $MgZn_2$ phases in one rod-shaped β_1' precipitate [68]. It is recommended to incorporate this situation into future precipitation models for a better understanding of precipitation kinetics in Mg-Zn alloys.
- It is recommended to consider different expressions of surface energy for different faces on rod-shaped and plate-shaped precipitates in future precipitation models.
- It is encouraged to quantitatively correlate the precipitate shape factor with different ageing conditions to provide better input for the precipitation model.
- It is highly recommended to perform a thorough microstructural investigation on the shearing of rod precipitates in polycrystal Mg-Zn alloys for a better understanding of strengthening mechanisms in this material.
- An analytical model to describe contributions from different deformation modes to yield strength is encouraged to be developed. Different precipitate parameters are encouraged to be applied to reveal the effect of precipitation on the relative importance of deformation modes to yield strength.
- The twin fractions obtained from EBSD data sets in the current study can be used for the development of models that describe the hardening mechanisms.
- Correlation of experimental data with crystal plasticity models to describe the relative activities between slip and twinning, in the presence of precipitates, is needed to better understand the increased twin fractions in grains unfavourably oriented for twinning.

8. Appendix

8.1 Strengthening model of poly-dispersed precipitates on twinning plane.

To calculate $n'b$, L_{twin} and $\overline{D}$ in Eq. (6.1), we equivalent the intersecting area of rods on the twinning plane to a sphere shape, the particle arrangement can be the same as in Fig. 5.2. And the effective radius is then:

$$\bar{r} = \sqrt{\frac{r^2}{\cos \emptyset}} = r\sqrt{\frac{1}{\cos \emptyset}} \qquad (8.1)$$

ø is the angle between $\{10\bar{1}2\}$ twinning plane and $\{0001\}$ basal plane. And the precipitate probability on twinning plane:

$$l' = 2r \sin \emptyset + l \cos \emptyset \qquad (8.2)$$

The angle relation can be expressed by the Mg lattice parameters a and c:

$$\cos \emptyset = \frac{\sqrt{3}a}{\sqrt{c^2+3a^2}} = 0.73$$

$$\sin \emptyset = \frac{c}{\sqrt{c^2+3a^2}} = 0.684 \qquad (8.3)$$

If we consider triangular distribution. N_a becomes:

$$N_a = \frac{2}{\sqrt{3}(L_{twin}+2r\sqrt{\frac{1}{\cos \emptyset}})^2} = \frac{f_v}{\pi r^2 l} l' \qquad (8.4)$$

Therefore particle spacing on twinning plane becomes

$$L_{twin} = \sqrt{\frac{2}{\sqrt{3}} \frac{\pi r^2 l}{f_v(2r \sin \emptyset + l \cos \emptyset)}} - 2r\sqrt{\frac{1}{\cos \emptyset}} \qquad (8.5)$$

For poly-dispersed precipitates. The effective radius becomes:

$$\bar{r} = \frac{\sum_i N_i r_i}{\sum_i N_i} \sqrt{\frac{1}{\cos \emptyset}} \qquad (8.6)$$

And the area density becomes:

$$N_a = \frac{2}{\sqrt{3}(L_{twin}+2\bar{r})^2} = \sum_i N_i(2r_i \sin \emptyset + l_i \cos \emptyset) \qquad (8.7)$$

We can then have the particle spacing:

$$L_{twin} = \sqrt{\frac{2}{\sqrt{3}\sum_i N_i(2r_i \sin\emptyset + l_i \cos\emptyset)}} - \frac{2\sum_i N_i r_i}{\sum_i N_i}\sqrt{\frac{1}{\cos\emptyset}} \qquad (8.8)$$

With:

$$n'b = b_0'(\frac{2\bar{r}}{b})^{\frac{1}{3}} = b_0'(\frac{2\sum_i N_i r_i}{b\sum_i N_i}\sqrt{\frac{1}{\cos\emptyset}})^{\frac{1}{3}} \qquad (8.9)$$

We can then have:

$$\bar{D} = \frac{2}{\left(\sqrt{\frac{2}{\sqrt{3}\sum_i N_i(2r_i \sin\emptyset + l_i \cos\emptyset)}} - \frac{2\sum_i N_i r_i}{\sum_i N_i}\sqrt{\frac{1}{\cos\emptyset}}\right)^{-1} + \left(\frac{2\sum_i N_i r_i}{\sum_i N_i}\sqrt{\frac{1}{\cos\emptyset}}\right)^{-1}} \qquad (8.10)$$

8.2 Modelling code in PreciSo

PreciSo is an open-source software developed by Perez and his colleagues [19, 109] that uses a model based on the classical nucleation, growth and coarsening theories, fully described in the review of Kampmann and Wagner [16]. In this work, Preciso is modified and used to follow the evolution of precipitation state in Mg-Zn alloys.

Full software files can be found at Arnaud Allera / Preciso · GitLab, and the author's contribution is in Files · hcp_mechanical · Arnaud Allera / Preciso · GitLab. The code written for this work is presented in the below sections.

8.2.1 Interface of precipitation model

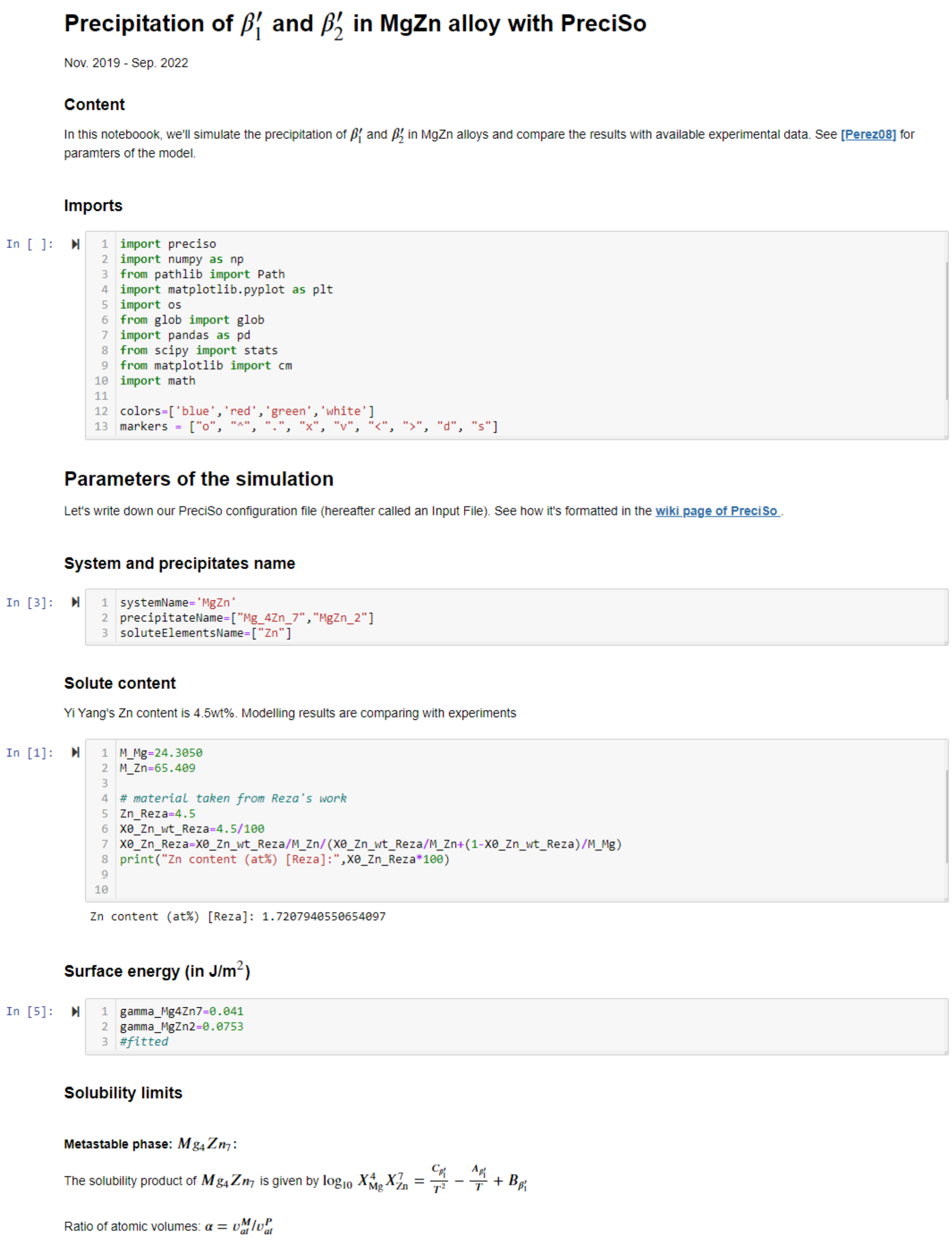

Precipitation of β_1' and β_2' in MgZn alloy with PreciSo

Nov. 2019 - Sep. 2022

Content

In this noteboook, we'll simulate the precipitation of β_1' and β_2' in MgZn alloys and compare the results with available experimental data. See [Perez08] for paramters of the model.

Imports

In [ ]:

```
import preciso
import numpy as np
from pathlib import Path
import matplotlib.pyplot as plt
import os
from glob import glob
import pandas as pd
from scipy import stats
from matplotlib import cm
import math

colors=['blue','red','green','white']
markers = ["o", "^", ".", "x", "v", "<", ">", "d", "s"]
```

Parameters of the simulation

Let's write down our PreciSo configuration file (hereafter called an Input File). See how it's formatted in the wiki page of PreciSo .

System and precipitates name

In [3]:

```
systemName='MgZn'
precipitateName=["Mg_4Zn_7","MgZn_2"]
soluteElementsName=["Zn"]
```

Solute content

Yi Yang's Zn content is 4.5wt%. Modelling results are comparing with experiments

In [1]:

```
M_Mg=24.3050
M_Zn=65.409

# material taken from Reza's work
Zn_Reza=4.5
X0_Zn_wt_Reza=4.5/100
X0_Zn_Reza=X0_Zn_wt_Reza/M_Zn/(X0_Zn_wt_Reza/M_Zn+(1-X0_Zn_wt_Reza)/M_Mg)
print("Zn content (at%) [Reza]:",X0_Zn_Reza*100)


```

```
Zn content (at%) [Reza]: 1.7207940550654097
```

Surface energy (in J/m^2)

In [5]:

```
gamma_Mg4Zn7=0.041
gamma_MgZn2=0.0753
#fitted
```

Solubility limits

Metastable phase: Mg_4Zn_7:

The solubility product of Mg_4Zn_7 is given by $\log_{10} X_{\mathrm{Mg}}^4 X_{\mathrm{Zn}}^7 = \frac{C_{\beta_1'}}{T^2} - \frac{A_{\beta_1'}}{T} + B_{\beta_1'}$

Ratio of atomic volumes: $\alpha = \upsilon_{at}^M / \upsilon_{at}^P$

In [6]:

```
V_Mg=2.3240889031550664e-29
V_Mg4Zn7=1.72406235e-29
alpha_Mg4Zn7=V_Mg/V_Mg4Zn7
print("alpha_Mg4Zn7=", alpha_Mg4Zn7)
```

```
alpha_Mg4Zn7= 1.348030657449869
```

In [ ]:

```
# At T=150 °C, we take the results from Yi Yang !
T1_Mg4Zn7=150+273.15



# At T=200 °C, we take the results from Reza
T2_Mg4Zn7=200+273.15


Xp_Zn_Mg4Zn7=7/11
Xp_Mg_Mg4Zn7=4/11


X1_Zn_Mg4Zn7=0.0059 #From TEP
R=5E-9 #from TEM
b=25 #shape factor of rods from TEM
k=1.38E-23 #Boltzmann constant
R0_T1=(4*b*gamma_Mg4Zn7*V_Mg4Zn7*11)/((3*b-2)*k*T1_Mg4Zn7)
X1_Mg_Mg4Zn7=1-X1_Zn_Mg4Zn7
K1_Mg4Zn7_R=X1_Zn_Mg4Zn7**(7)*X1_Mg_Mg4Zn7**(4)
K1_Mg4Zn7=K1_Mg4Zn7_R*math.exp(-R0_T1/R) #Gibbs-Thomson correction
print("Solute content at T1 (at%): ", X1_Zn_Mg4Zn7*100)
#print("Solute content at T1 (wt%): ", X1_Zn_wt)

#
X2_Zn_Mg4Zn7=0.008
R0_T2=(4*b*gamma_Mg4Zn7*V_Mg4Zn7*11)/((3*b-2)*k*T2_Mg4Zn7)
X2_Mg_Mg4Zn7=1-X2_Zn_Mg4Zn7
K2_Mg4Zn7_R=X2_Zn_Mg4Zn7**(7)*X2_Mg_Mg4Zn7**(4)
K2_Mg4Zn7=K2_Mg4Zn7_R*math.exp(-R0_T2/R) #Gibbs-Thomson correction
#X2_Zn_wt=(X2_Zn_Mg4Zn7*M_Zn/(X2_Zn_Mg4Zn7*M_Zn+(1-X2_Zn_Mg4Zn7)*M_Mg))*100
print("Solute content at T2 (at%): ",X2_Zn_Mg4Zn7*100)
#print("Solute content at T2 (wt%): ", X2_Zn_wt)

A_Mg4Zn7=np.log10(K1_Mg4Zn7/K2_Mg4Zn7)/(1/T2_Mg4Zn7-1/T1_Mg4Zn7)
B_Mg4Zn7=(T1_Mg4Zn7*np.log10(K1_Mg4Zn7)-T2_Mg4Zn7*np.log10(K2_Mg4Zn7))/(T1_Mg4Zn7-T2_Mg4Zn7)
C_Mg4Zn7=0
print(A_Mg4Zn7,B_Mg4Zn7)


X0_Zn=X0_Zn_Reza
X0_Mg=1-X0_Zn
Ks_Mg4Zn7=np.log10(X0_Mg**(4)*X0_Zn**(7))
Ts_Mg4Zn7=-273.15+A_Mg4Zn7/(B_Mg4Zn7-np.log10(X0_Mg**(4)*X0_Zn**(7)))

print("Solubility temperature (in °C): ",Ts_Mg4Zn7)
print("Solubility product at Ts: ",Ks_Mg4Zn7)



```

Metastable phase: $MgZn_2$**:**

The solubility product of $MgZn_2$ is given by $\log_{10} X_{\mathrm{Mg}}^{1} X_{\mathrm{Zn}}^{2} = \frac{C_{\beta_1'}}{T^2} - \frac{A_{\beta_1'}}{T} + B_{\beta_1'}$

Ratio of atomic volumes: $\alpha = \upsilon_{at}^{M}/\upsilon_{at}^{P}$

In [8]:

```

V_MgZn2=1.623153858333e-29

alpha_MgZn2=V_Mg/V_MgZn2

print("alpha_MgZn2=", alpha_MgZn2)
```

```
alpha_MgZn2= 1.4318352454535246
```

In [ ]:

```
# At T=150 °C, we take the results from Yi Yang !
T1_MgZn2=150+273.15


# At T=200 °C, we take the results from Reza
T2_MgZn2=200+273.15

Xp_Zn_MgZn2=2/3
Xp_Mg_MgZn2=1/3
```

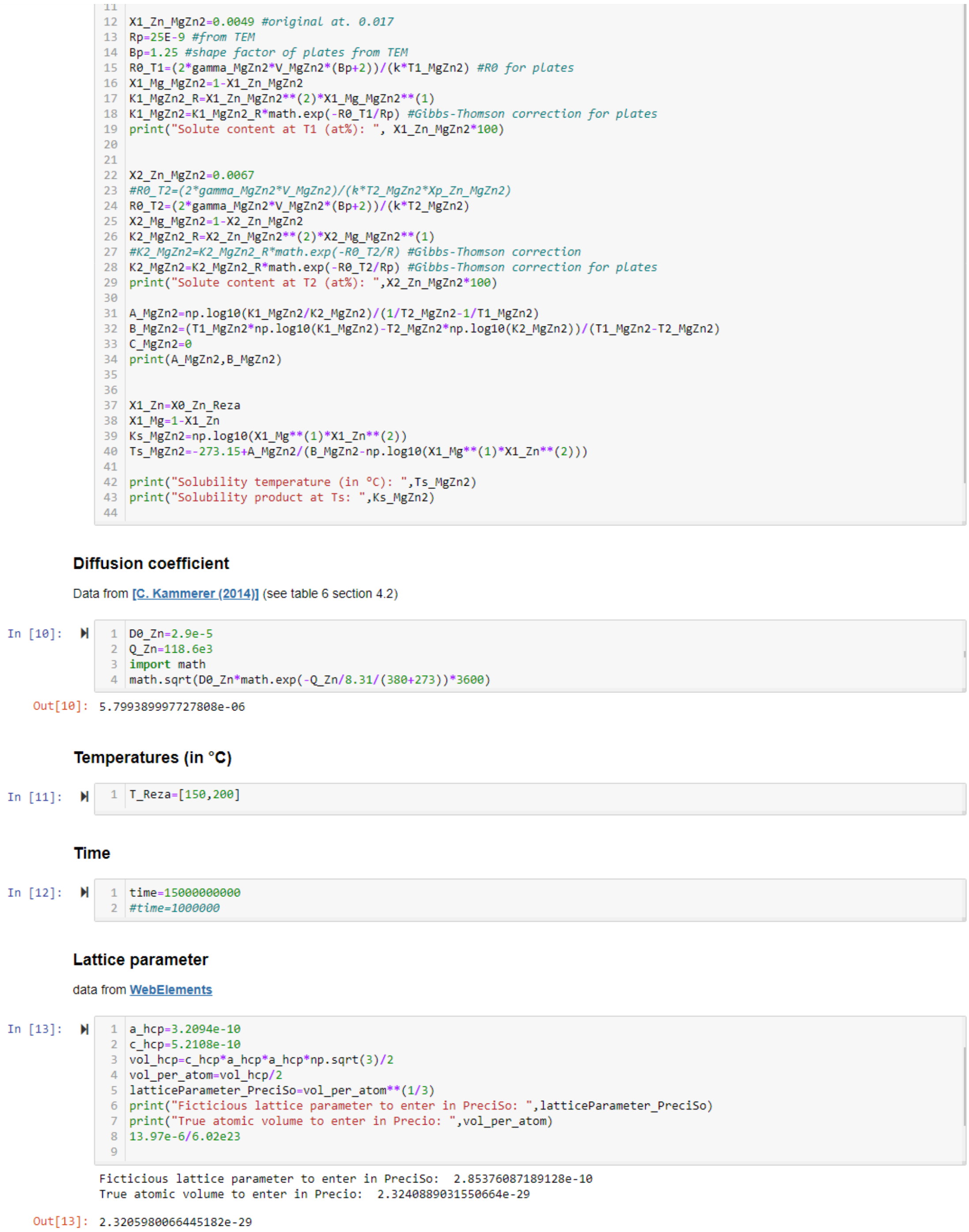

```
X1_Zn_MgZn2=0.0049 #original at. 0.017
Rp=25E-9 #from TEM
Bp=1.25 #shape factor of plates from TEM
R0_T1=(2*gamma_MgZn2*V_MgZn2*(Bp+2))/(k*T1_MgZn2) #R0 for plates
X1_Mg_MgZn2=1-X1_Zn_MgZn2
K1_MgZn2_R=X1_Zn_MgZn2**(2)*X1_Mg_MgZn2**(1)
K1_MgZn2=K1_MgZn2_R*math.exp(-R0_T1/Rp) #Gibbs-Thomson correction for plates
print("Solute content at T1 (at%): ", X1_Zn_MgZn2*100)


X2_Zn_MgZn2=0.0067
#R0_T2=(2*gamma_MgZn2*V_MgZn2)/(k*T2_MgZn2*Xp_Zn_MgZn2)
R0_T2=(2*gamma_MgZn2*V_MgZn2*(Bp+2))/(k*T2_MgZn2)
X2_Mg_MgZn2=1-X2_Zn_MgZn2
K2_MgZn2_R=X2_Zn_MgZn2**(2)*X2_Mg_MgZn2**(1)
#K2_MgZn2=K2_MgZn2_R*math.exp(-R0_T2/R) #Gibbs-Thomson correction
K2_MgZn2=K2_MgZn2_R*math.exp(-R0_T2/Rp) #Gibbs-Thomson correction for plates
print("Solute content at T2 (at%): ",X2_Zn_MgZn2*100)

A_MgZn2=np.log10(K1_MgZn2/K2_MgZn2)/(1/T2_MgZn2-1/T1_MgZn2)
B_MgZn2=(T1_MgZn2*np.log10(K1_MgZn2)-T2_MgZn2*np.log10(K2_MgZn2))/(T1_MgZn2-T2_MgZn2)
C_MgZn2=0
print(A_MgZn2,B_MgZn2)


X1_Zn=X0_Zn_Reza
X1_Mg=1-X1_Zn
Ks_MgZn2=np.log10(X1_Mg**(1)*X1_Zn**(2))
Ts_MgZn2=-273.15+A_MgZn2/(B_MgZn2-np.log10(X1_Mg**(1)*X1_Zn**(2)))

print("Solubility temperature (in °C): ",Ts_MgZn2)
print("Solubility product at Ts: ",Ks_MgZn2)

```

Diffusion coefficient

Data from [C. Kammerer (2014)] (see table 6 section 4.2)

In [10]:

```
D0_Zn=2.9e-5
Q_Zn=118.6e3
import math
math.sqrt(D0_Zn*math.exp(-Q_Zn/8.31/(380+273))*3600)
```

```
Out[10]: 5.799389997727808e-06
```

Temperatures (in °C)

In [11]:

```
T_Reza=[150,200]
```

Time

In [12]:

```
time=15000000000
#time=1000000
```

Lattice parameter

data from WebElements

In [13]:

```
a_hcp=3.2094e-10
c_hcp=5.2108e-10
vol_hcp=c_hcp*a_hcp*a_hcp*np.sqrt(3)/2
vol_per_atom=vol_hcp/2
latticeParameter_PreciSo=vol_per_atom**(1/3)
print("Ficticious lattice parameter to enter in PreciSo: ",latticeParameter_PreciSo)
print("True atomic volume to enter in Precio: ",vol_per_atom)
13.97e-6/6.02e23

```

```
Ficticious lattice parameter to enter in PreciSo:  2.85376087189128e-10
True atomic volume to enter in Precio:  2.3240889031550664e-29
```

```
Out[13]: 2.3205980066445182e-29
```

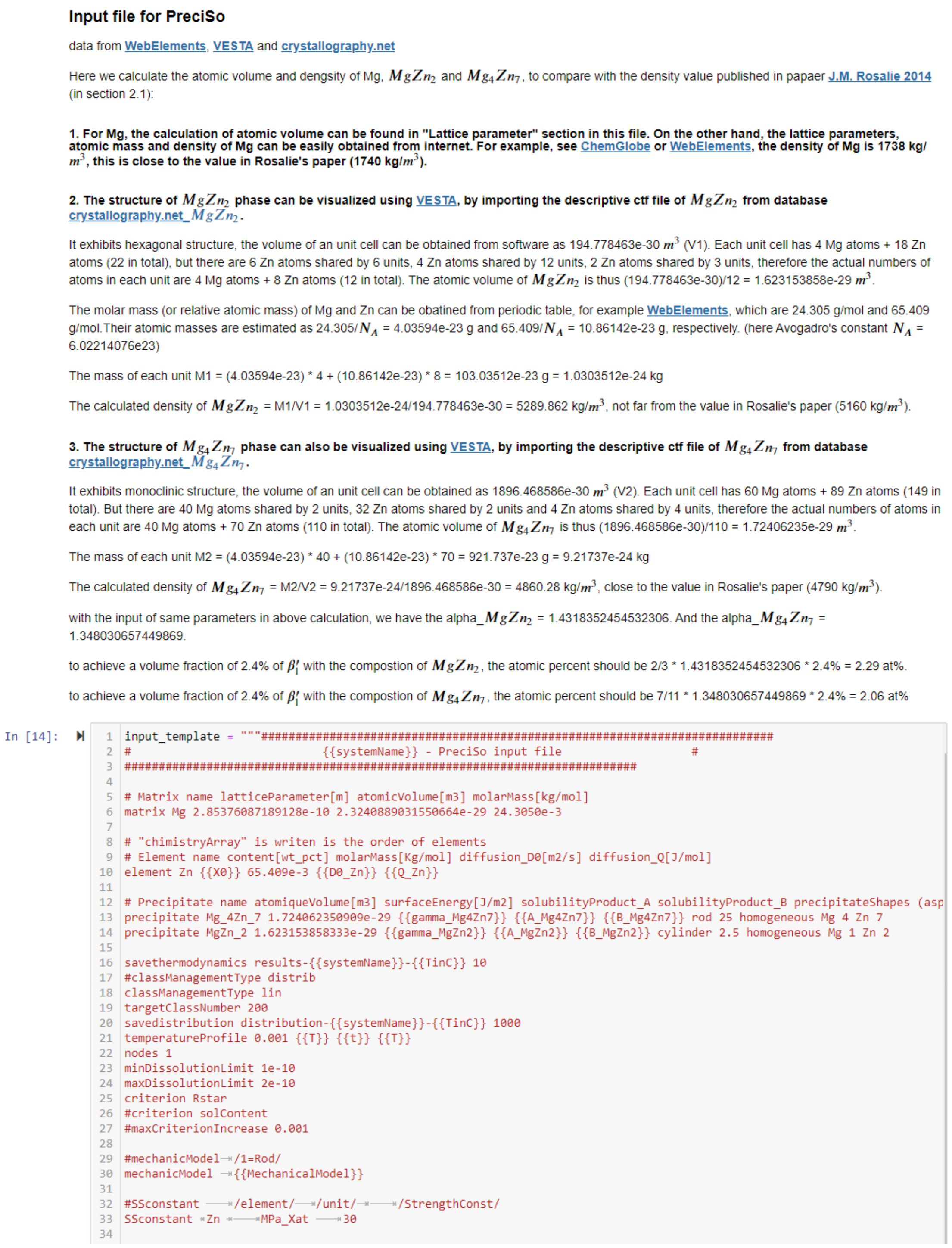

Input file for PreciSo

data from WebElements, VESTA and crystallography.net

Here we calculate the atomic volume and dengsity of Mg, $MgZn_2$ and Mg_4Zn_7, to compare with the density value published in papaer J.M. Rosalie 2014 (in section 2.1):

1. For Mg, the calculation of atomic volume can be found in "Lattice parameter" section in this file. On the other hand, the lattice parameters, atomic mass and density of Mg can be easily obtained from internet. For example, see ChemGlobe or WebElements, the density of Mg is 1738 kg/m^3, this is close to the value in Rosalie's paper (1740 kg/m^3).

2. The structure of $MgZn_2$ phase can be visualized using VESTA, by importing the descriptive ctf file of $MgZn_2$ from database crystallography.net_$MgZn_2$.

It exhibits hexagonal structure, the volume of an unit cell can be obtained from software as 194.778463e-30 m^3 (V1). Each unit cell has 4 Mg atoms + 18 Zn atoms (22 in total), but there are 6 Zn atoms shared by 6 units, 4 Zn atoms shared by 12 units, 2 Zn atoms shared by 3 units, therefore the actual numbers of atoms in each unit are 4 Mg atoms + 8 Zn atoms (12 in total). The atomic volume of $MgZn_2$ is thus (194.778463e-30)/12 = 1.623153858e-29 m^3.

The molar mass (or relative atomic mass) of Mg and Zn can be obatined from periodic table, for example WebElements, which are 24.305 g/mol and 65.409 g/mol.Their atomic masses are estimated as 24.305/N_A = 4.03594e-23 g and 65.409/N_A = 10.86142e-23 g, respectively. (here Avogadro's constant N_A = 6.02214076e23)

The mass of each unit M1 = (4.03594e-23) * 4 + (10.86142e-23) * 8 = 103.03512e-23 g = 1.0303512e-24 kg

The calculated density of $MgZn_2$ = M1/V1 = 1.0303512e-24/194.778463e-30 = 5289.862 kg/m^3, not far from the value in Rosalie's paper (5160 kg/m^3).

3. The structure of Mg_4Zn_7 phase can also be visualized using VESTA, by importing the descriptive ctf file of Mg_4Zn_7 from database crystallography.net_Mg_4Zn_7.

It exhibits monoclinic structure, the volume of an unit cell can be obtained as 1896.468586e-30 m^3 (V2). Each unit cell has 60 Mg atoms + 89 Zn atoms (149 in total). But there are 40 Mg atoms shared by 2 units, 32 Zn atoms shared by 2 units and 4 Zn atoms shared by 4 units, therefore the actual numbers of atoms in each unit are 40 Mg atoms + 70 Zn atoms (110 in total). The atomic volume of Mg_4Zn_7 is thus (1896.468586e-30)/110 = 1.72406235e-29 m^3.

The mass of each unit M2 = (4.03594e-23) * 40 + (10.86142e-23) * 70 = 921.737e-23 g = 9.21737e-24 kg

The calculated density of Mg_4Zn_7 = M2/V2 = 9.21737e-24/1896.468586e-30 = 4860.28 kg/m^3, close to the value in Rosalie's paper (4790 kg/m^3).

with the input of same parameters in above calculation, we have the alpha_$MgZn_2$ = 1.4318352454532306. And the alpha_Mg_4Zn_7 = 1.348030657449869.

to achieve a volume fraction of 2.4% of β_1' with the compostion of $MgZn_2$, the atomic percent should be 2/3 * 1.4318352454532306 * 2.4% = 2.29 at%.

to achieve a volume fraction of 2.4% of β_1' with the compostion of Mg_4Zn_7, the atomic percent should be 7/11 * 1.348030657449869 * 2.4% = 2.06 at%

In [14]:

```
input_template = """###########################################################################
#                            {{systemName}} - PreciSo input file                  #
###########################################################################

# Matrix name latticeParameter[m] atomicVolume[m3] molarMass[kg/mol]
matrix Mg 2.85376087189128e-10 2.3240889031550664e-29 24.3050e-3

# "chimistryArray" is writen is the order of elements
# Element name content[wt_pct] molarMass[Kg/mol] diffusion_D0[m2/s] diffusion_Q[J/mol]
element Zn {{X0}} 65.409e-3 {{D0_Zn}} {{Q_Zn}}

# Precipitate name atomiqueVolume[m3] surfaceEnergy[J/m2] solubilityProduct_A solubilityProduct_B precipitateShapes (asp
precipitate Mg_4Zn_7 1.724062350909e-29 {{gamma_Mg4Zn7}} {{A_Mg4Zn7}} {{B_Mg4Zn7}} rod 25 homogeneous Mg 4 Zn 7
precipitate MgZn_2 1.623153858333e-29 {{gamma_MgZn2}} {{A_MgZn2}} {{B_MgZn2}} cylinder 2.5 homogeneous Mg 1 Zn 2

savethermodynamics results-{{systemName}}-{{TinC}} 10
#classManagementType distrib
classManagementType lin
targetClassNumber 200
savedistribution distribution-{{systemName}}-{{TinC}} 1000
temperatureProfile 0.001 {{T}} {{t}} {{T}}
nodes 1
minDissolutionLimit 1e-10
maxDissolutionLimit 2e-10
criterion Rstar
#criterion solContent
#maxCriterionIncrease 0.001

#mechanicModel	/1=Rod/
mechanicModel 	{{MechanicalModel}}

#SSconstant 		/element/	/unit/		/StrengthConst/
SSconstant 	Zn 		MPa_Xat 	30

```

```

#precipitateConstants	/Name/	/critialRad/	/arrangement/	/youngModulus/	/poissCoef/	/hard1/	/hard2/	/hard3/	/k_s
precipitateConstants	Mg_4Zn_7	1.5e-009	triangularPath	210e9		0.3		0	0	0	{{k}}
precipitateConstants	MgZn_2	1.5e-009	triangularPath	210e9		0.3		0	0	0	{{k}}
#0.0291

#dislocations	/initialDensity/	/strength/	/betaff/
dislocations	0			0.5 {{beta}}

#cristalloConstants	/sigma_0/	/M/	/a0/		/lattice (a) (c)/
cristalloConstant	133000000	2.22	3.2e-010	hcp 3.2094e-10 5.2108e-10

grainSize 40.1254e-6 0 0 0
young 273 44e9
poisson 273 0.33

"""
```

Run PreciSo at various temperatures

Simulation for Mg4Zn7

Yi's simulation

In [15]:

```python
results_Reza=[]
T=T_Reza
MechanicalModel=8
for i in range(len(T)):

        # Key - Values to be inserted in the template
        values = {"systemName":systemName,
          "X0":Zn_Reza,
          "T":T[i]+273.15,
          "t":time,
          "TinC":T[i],
          "D0_Zn":D0_Zn,
          "Q_Zn":Q_Zn,
          "gamma_Mg4Zn7":gamma_Mg4Zn7,
          "gamma_MgZn2":gamma_MgZn2,
          "A_Mg4Zn7":A_Mg4Zn7,
          "B_Mg4Zn7":B_Mg4Zn7,
          "A_MgZn2":A_MgZn2,
          "B_MgZn2":B_MgZn2,
          "beta":0.21, # 0.2-0.5
          "k":0,# k is claculated from critical radius
          "MechanicalModel":MechanicalModel}
        #No. of MechanicalModel:
        # 0: ModelAlex_fcc_plates
        # 1: Model_fcc_rod1
        # 2: Model_fcc_rod2
        # 3: Model_fcc_rod3
        # 4: Model_fcc_rod4
        # 5: ModelFisk_fcc_plates
        # 6: ModelAlex_fcc_sphere
        # 7: ModelYi_hcp_basal
        # 8: ModelYi_hcp_prismatic
        # 9: ModelYi_hcp_twinning

        # fill the template
        input_file = preciso.fillTemplate(input_template, values)

        # save the input file
        input_fileName=Path(systemName+'-'+str(T[i])+'.essai.input')
        print("Input file name: "+str(input_fileName))
        with open(input_fileName, 'w') as f:
            f.write(input_file)
        #print(input_fileName)
        # run PreciSo
        results_Reza.append(preciso.runSimulation(input_fileName, debug= False, temp=False))

```

```
Input file name: MgZn-150.essai.input
Input file name: MgZn-200.essai.input
```

Results

All results are stored in convenient pandas DataFrames.

Radii_Yi

```python
T=T_Reza
fig=plt.figure(figsize=(9*len(T),7))
for i in range(len(T)):
    ax=fig.add_subplot(1,len(T),i+1)
    maximum=0
    data=results_Reza[i].precipitation[0]
    for j in range(len(precipitateName)):
        precipitateNameLabel=precipitateName[j]
        plt.loglog(data['t[s]'], data["rmean_"+precipitateName[j]+"[m]"], color=colors[j],
               label="$\\langle r^{{"+precipitateNameLabel + "}}\\rangle$ simulations ("+str(T[i])+" °C)",linewidth=2)
        plt.loglog(data['t[s]'], data["r*_"+precipitateName[j]+"[m]"], color=colors[i], ls='dashed',
               label="${{r^*}}^{{"+precipitateNameLabel+"}}$ simulations ("+str(T[i])+" °C)",linewidth=2)
        maximum=max(maximum,1.5*max(data["rmean_"+precipitateName[j]+"[m]"]))

    plt.grid(True,which="both",ls="-", color="grey")
    plt.ylim([0,maximum])

    dataPath=str(os.getcwd())+'/Radii-Reza-'+str(T[i])+'/'
    ls = sorted(glob(dataPath + '*.txt'))
    markers = ["o", "^", ".", "x", "v", "<", ">", "d", "s","o", "^", ".", "x", "v", "<", ">", "d", "s"]

    for j, file in enumerate(ls):
        label = os.path.splitext(os.path.split(file)[1])[0]
        dataToPlot=pd.read_csv(file,sep='\t',header =0)
        color = colors[j]
        plt.scatter(dataToPlot["t[s]"], dataToPlot["r[m]"], color=color, label=label, marker=markers[j], s=50)

    plt.ylabel('Radius (m)')
    plt.xlabel('Time (s)')
    plt.title('Mean radius versus time at '+str(T[i])+'°C')
    plt.legend(bbox_to_anchor=(0.55, .95), loc=1, borderaxespad=0.,fontsize=13)
    plt.savefig('RadiiVsTime-'+str(T[i])+'.pdf')

```

Volume fraction_Yi

```python
T=T_Reza
fig=plt.figure(figsize=(7*len(T),7))
for i in range(len(T)):
    ax=fig.add_subplot(1,len(T),i+1)
    maximum=0
    data=results_Reza[i].precipitation[0]
    sumfv=0
    for j in range(len(precipitateName)):
        precipitateNameLabel=precipitateName[j]
        precipitateNameLabel=precipitateNameLabel.replace("gamma","\\gamma")
        plt.semilogx(data['t[s]'], data["fv_"+precipitateName[j]], color=colors[j],
                 label="${{f_v^{{"+ precipitateNameLabel + "}}}}$")
        plt.ylabel('Volume fraction')
        sumfv=sumfv+data["fv_"+precipitateName[j]]
        maximum=max(maximum,1.1*max(data["fv_"+precipitateName[j]]))

    plt.ylim([-0.002,0.018])
    plt.xlim([10,10e7])

    dataPath=str(os.getcwd())+'/Fv-Yi-mg4zn7-'+str(T[i])+'/'
    ls = sorted(glob(dataPath + '*.txt'))
    markers = ["o", "^", ".", "x", "v", "<", ">", "d", "s"]
    for j, file in enumerate(ls):
        label = os.path.splitext(os.path.split(file)[1])[0]
        dataToPlot=pd.read_csv(file,sep='\t',header =0)
        if len(ls) == 1:
            color = 'blue'
        else:
            color=cm.jet(j*1./(len(ls)-1))
        plt.scatter(dataToPlot["t[s]"], dataToPlot["fv"], color=color, label=label, marker=markers[j], s=50)


    plt.xlabel('Time (s)')
    plt.title('Volume fraction versus time at '+str(T[i])+'°C')
    plt.legend(loc='best')
    plt.savefig('VolFractionVsTime-'+str(T[i])+'.pdf')

```

Precipitate number density_Yi

In [ ]:

```python
fig=plt.figure(figsize=(7*len(T),7))
T=T_Reza
for i in range(len(T)):
    ax=fig.add_subplot(1,len(T),i+1)
    maximum=0
    data=results_Reza[i].precipitation[0]
    for j in range(len(precipitateName)):
        precipitateNameLabel=precipitateName[j]
        precipitateNameLabel=precipitateNameLabel.replace("gamma","\\gamma")
        plt.loglog(data['t[s]'], data["N_"+precipitateName[j]], color=colors[j],
                 label="$N^{{"+precipitateNameLabel+"}}$")
        plt.ylabel('Number density')

        maximum=max(maximum,1.1*max(data["N_"+precipitateName[j]]))



    dataPath=str(os.getcwd())+'/N-Reza-'+str(T[i])+'/'
    ls = sorted(glob(dataPath + '*.txt'))
    markers = ["o", "^", ".", "x", "v", "<", ">", "d", "s"]
    for j, file in enumerate(ls):
        label = os.path.splitext(os.path.split(file)[1])[0]
        dataToPlot=pd.read_csv(file,sep='\t',header =0)
        color = colors[j]
        maximum=max(maximum,1.1*max(dataToPlot["N"]))
        plt.scatter(dataToPlot["t[s]"], dataToPlot["N"], color=color, label=label, marker=markers[j], s=50)

    plt.ylim([0,maximum])
    plt.xlabel('Time (s)')
    plt.title('Number density versus time at '+str(T[i])+'°C')
    plt.legend(loc='best')
    plt.savefig('NumberDensityVsTime-'+str(T[i])+'.pdf')

```

Solute concentration_Yi

In [ ]:

```python
fig=plt.figure(figsize=(7*len(T),7))
T=T_Reza
for i in range(len(T)):
    ax=fig.add_subplot(1,len(T),i+1)
    maximum=0
    data=results_Reza[i].precipitation[0]
    for j in range(len(soluteElementsName)):
        plt.loglog(data['t[s]'], data["X_"+soluteElementsName[j]], color=colors[i],
               label="$X_\mathrm{{"+soluteElementsName[j]+"}}$")
        plt.ylabel('Zn concentration (at.)')

        maximum=max(maximum,1.1*max(data["X_"+soluteElementsName[j]]))

    plt.ylim([-4,0.02])

    dataPath=str(os.getcwd())+'/Concentration-'+str(T[i])+'/'
    ls = sorted(glob(dataPath + '*.txt'))
    for j, file in enumerate(ls):
        label = os.path.splitext(os.path.split(file)[1])[0]
        dataToPlot=pd.read_csv(file,sep='\t',header =0)
        if len(ls) == 1:
            color = 'blue'
        else:
            color=cm.jet(j*1./(len(ls)-1))
        plt.scatter(dataToPlot["t[s]"], dataToPlot["fv"], color=color, label=label, marker=markers[j], s=50)


    plt.xlabel('Time (s)')
    plt.title('Solute Concentration versus time at '+str(T[i])+'°C')
    plt.legend(loc='best')
    plt.savefig('SoluteConcentration-'+str(T[i])+'.pdf')
```

Mechanics

In [ ]:

```python
fig=plt.figure(figsize=(7*len(T),7))
for i in range(len(T)):
    ax=fig.add_subplot(1,len(T),i+1)
    maximum=0
    data=results_Reza[i].mechanics[0]
    plt.semilogx(data['t[s]'], data['SigmaSS[MPa]'], color='goldenrod', label='Solid solution',linewidth=1)

    for j in range(len(precipitateName)):
        precipitateNameLabel=precipitateName[j]
        precipitateNameLabel=precipitateNameLabel.replace("betasec","\\beta''")
        precipitateNameLabel=precipitateNameLabel.replace("TypeB","Type-B")
        plt.semilogx(data['t[s]'],data["sigma"+precipitateName[j]+"_sh[MPa]"], color=colors[j],label=precipitateNameLabe
        plt.semilogx(data['t[s]'],data["sigma"+precipitateName[j]+"_bp[MPa]"], color=colors[j],label=precipitateNameLabe

    plt.semilogx(data['t[s]'],data["sigmaFlowMicro[MPa]"], color="steelblue", label='Total',linewidth=2)

    if MechanicalModel == 7:
        dataPath=str(os.getcwd())+'/MechanicsBasal-'+str(T[i])+'/'
    elif MechanicalModel == 8:
        dataPath=str(os.getcwd())+'/MechanicsPri-'+str(T[i])+'/'
    elif MechanicalModel == 9:
        dataPath=str(os.getcwd())+'/MechanicsTwin-'+str(T[i])+'/'
    else:
        dataPath=str(os.getcwd())+'/Mechanics-'+str(T[i])+'/'

    ls = sorted(glob(dataPath + '*.txt'))
    markers = ["o", "^", ".", "x", "v", "<", ">", "d", "s"]
    for j, file in enumerate(ls):
        label = os.path.splitext(os.path.split(file)[1])[0]
        dataToPlot=pd.read_csv(file,sep='\t',header =0)
        if len(ls) == 1:
            color = 'black'
        else:
            color=cm.jet(i*1./(len(ls)-1))
        plt.errorbar(dataToPlot["t[s]"], dataToPlot["sigma_y[MPa]"], color=color, label=label,
                     marker=markers[j], yerr=10,markersize=10,fmt='o',markerfacecolor='white')#//error

    plt.xlim((1,1e8))
    plt.ylabel('Yield stress (MPa)',fontsize=10)
    plt.xlabel('Time (s)',fontsize=10)
    plt.title('Yield stress vs time at '+str(T[i])+'°C',fontsize=10)
    plt.legend(loc=2,fontsize=10)
    plt.xticks(fontsize=10)
    plt.yticks(fontsize=10)

    print('Saving figure: Mechanics-'+str(T[i])+'.pdf...')
    plt.savefig('Mechanics-'+str(T[i])+'.pdf', dpi=96)
```

TTT diagram

Temperatures (in °C) and time (in s)

In [ ]:

```python
Tmin=100
Tmax=250
TStep=10
T=np.arange(Tmin,Tmax+TStep,TStep)
initialTime=1
finalTime=1e9
timeInter=np.logspace(np.log10(initialTime),np.log10(finalTime),100)
time=finalTime
```

Run PreciSo at all temperatures

In [ ]:

```
results=[]
for i in range(len(T)):

        # Key - Values to be inserted in the template
        values = {"systemName":systemName,
          "X0":Zn_Reza,
          "T":T[i]+273.15,
          "t":time,
          "TinC":T[i],
          "D0_Zn":D0_Zn,
          "Q_Zn":Q_Zn,
          "gamma_Mg4Zn7":gamma_Mg4Zn7,
          "gamma_MgZn2":gamma_MgZn2,
          "A_Mg4Zn7":A_Mg4Zn7,
          "B_Mg4Zn7":B_Mg4Zn7,
          "A_MgZn2":A_MgZn2,
          "B_MgZn2":B_MgZn2,
          "beta":0.25, # 0.2-0.5
          "k":0,#
          "MechanicalModel":MechanicalModel}

        # fill the template
        input_file = preciso.fillTemplate(input_template, values)

        # save the input file
        input_fileName=Path(systemName+'-'+str(T[i])+'.TTT.input')
        print("Input file name: "+str(input_fileName))
        with open(input_fileName, 'w') as f:
            f.write(input_file)
        print(input_fileName)
        # run PreciSo
        results.append(preciso.runSimulation(input_fileName, debug= False, temp=False))# temp=False preciso write in cur
```

Treat the results

In [ ]:

```
from scipy import interpolate
t_m=[]
t_50=[]
t_p=[]
temp=[]
sigma=[]

for i in range(len(T)):
    data= results[i].precipitation[0]
    data_mech=results[i].mechanics[0]
    for j in range(len(precipitateName)):
        fv=[]
        t=[]
        fv=data["fv_"+precipitateName[j]].tolist()
        t=data['t[s]'].tolist()
        fv_max=max(fv)
        if fv_max != 0:
            max_index = fv.index(fv_max)
            fv=fv[0:max_index]
            t=t[0:max_index]
            f = interpolate.interp1d(fv,t)
            t_m.append([])
            t_50.append([])
            t_p.append([])
            t_m[j].append(f(0.2*fv_max))
            t_50[j].append(f(0.5*fv_max))
            t_p[j].append(f(0.8*fv_max))
        else:
            t_m[j].append(0)
            t_50[j].append(0)
            t_p[j].append(0)

    temp.append(T[i])
    g=interpolate.interp1d(data['t[s]'],data_mech["sigmaFlowMicro[MPa]"])
    sigma.append(g(timeInter))

tempInter=np.arange(Tmin,Tmax,1)

f=interpolate.interp2d(timeInter,T,sigma)
sigmaInter=f(timeInter,tempInter)
```

TTT diagram

```python
f=plt.figure(figsize=(10,7))
fig, ax = plt.subplots()
ax.set_xscale('log')
ax.fontsize=14
ax.autoscale('tight')

for j in range(len(precipitateName)):
    label_m=precipitateName[j]+' (20%)'
    label_50=precipitateName[j]+' (50%)'
    label_p=precipitateName[j]+' (80%)'
    plt.semilogx(t_m[j],temp, color=colors[j], label=label_m,linewidth=1,linestyle='--')
    plt.semilogx(t_50[j],temp, color=colors[j], label=label_50,linewidth=2)
    plt.semilogx(t_p[j],temp, color=colors[j], label=label_p,linewidth=1,linestyle='--')


dataPath=str(os.getcwd())+'/TTT/'
ls = sorted(glob(dataPath + '*.txt'))
for k, file in enumerate(ls):
        label = os.path.splitext(os.path.split(file)[1])[0]
        print(label)
        j=0
        if ("betasec" in label) == True:
            j=0
        if ("typeB" in label) == True:
            j=1
        label=label.replace("betasec","$\\beta''$")
        label=label.replace("typeB","Type-B")
        data=pd.read_csv(file,sep='\t',header =0)
        print(data["temperature[°C]"])
        plt.scatter(data['t[s]'],data["temperature[°C]"], color=colors[k], label=label, marker=markers[k], s=50)


plt.legend(loc=2,fontsize=10)
plt.xlim([initialTime,finalTime])
plt.ylim([np.asarray(temp).min(),np.asarray(temp).max()])
plt.text(40, 510, '10%',color='white',fontsize=14)
plt.text(600, 575, '50%',color='white',fontsize=14)
plt.text(300000, 510, '90%',color='white',fontsize=14)
plt.ylabel('Temperature (°C)',fontsize=14)
plt.xlabel('Time (s)',fontsize=14)
plt.savefig('TTT.pdf')
```

8.2.2 Mechanical model for alloys with hcp structure

```cpp
void Mechanical::ModelYi_hcp_basal(Matrix const& _matrix, vector<Element> const&
_Elements, vector<Precipitate> const& _Precipitates, double _currentTime, double
_dt)
{
    if (structure != 2) { error.Fatal("In model 7 just 'hcp' structure is
considered"); }
    //###################################################################
    //###                 (Yi's model_basal slip)                     ###
    //###################################################################

    //-------------------- load constant ---------------------
    currentYoung = GetYoung();
    currentPoisson = GetPoisson();
    currentShearModulus = currentYoung / (2 * (1 + currentPoisson));
    //----------- compute SS & dislo contributions  ---------
    double sigmaDisloTemp = ComputeDisloContributionModel1();
    double sigmaSSTemp = ComputeSScontributionModel1(_Elements);

    //-------------- precipitate contribution --------------
    //initialization
    double sigmaGrainTemp=0.;
    double sigmaPreciTemp = 0., sigmaBp = 0., sigmaSh = 0., LjNj_bp = 0., LjNj_sh
= 0., RjNj_bp = 0., RjNj_sh = 0., TjNj_bp = 0., TjNj_sh = 0., sumNj = 0.;
    double aspectRatio = 0., Nj = 0., Rj = 0., Lj = 0., Tj = 0, sigmaTempI =
0.;//,shearConstantStrength=0.;
    double fv_bp_temp = 0., meanR_bp_temp = 0., meanL_BP_temp = 0., Nj_bp, Nj_sh,
distanceBetweenPPT_temp = 0.;
    double distancePPTsh_temp = 1e300, distancePPTbp_temp = 1e300,
distancePPTall_temp = 1e300;
```

```
    vector<double> sigmaPreciItemp; sigmaPreciItemp.clear();
    int yesShear = 0, yesByPass = 0;


    //tension line
    //double tensionLine = tensionLineConstant * currentShearModulus *
burgersNorm * burgersNorm;
    //-------------- initialisation for precipitate constants ---------------
    //stress contribution for each precipitates
    for (size_t i = 0; i < _Precipitates.size(); i++) { //different precipitate
kinds, e.g. b'1 and b'2
        //----------------------------------------
        yesShear = 0; yesByPass = 0;
        //read transition radius and compute shearConstantStrength
        // If a null value of k is in input, k is calculated via the critical
radius
        if (shearConstantStrength[i] == 0) {
            shearConstantStrength[i] = 2 * tensionLineConstant * burgersNorm /
transitionRadius[i];

        }
        //read transition radius and compute shearConstantStrength

        sigmaBp = 0., sigmaSh = 0., LjNj_bp = 0., LjNj_sh = 0., RjNj_bp = 0.,
RjNj_sh = 0., TjNj_bp = 0., TjNj_sh = 0., sumNj = 0., Nj = 0., Rj = 0., Lj = 0.;
        fv_bp_temp = 0.; meanR_bp_temp = 0.; meanL_BP_temp = 0.; Nj_bp = 0.;
Nj_sh = 0.; Tj = 0.; // re-initialize after loop

        if (_Precipitates[i].GetShapeIndex() == 2) // rod
        {
            aspectRatio = _Precipitates[i].GetAspectRatio();
            for (size_t j = 0; j < _Precipitates[i].GetNumberOfClass(); j++) {
                Nj = _Precipitates[i].GetNumber(j);
                Rj = _Precipitates[i].GetRadius(j);
                Lj = Rj * aspectRatio;
                if (Rj >= transitionRadius[i]) {
                    //by passing
                    LjNj_bp += Lj * Nj;
                    RjNj_bp = RjNj_bp + Rj * Nj;
                    Nj_bp += Nj;
                    yesByPass = 1;
                }
                else {
                    //shearing
                    LjNj_sh = LjNj_sh + Lj * Nj;
                    RjNj_sh = RjNj_sh + Rj * Nj;
                    Nj_sh += Nj;
                    yesShear = 1;
                }
            }
            if (PathStructure[i] == 2) //triangularPath
            {
                //compute sigmaBp and sigmaSh for this precipitate (triangular
path)
                if (yesByPass == 1) {
                    sigmaBp = 2.0 * taylorFactor * tensionLineConstant *
currentShearModulus * burgersNorm / (sqrt(2.0 / (sqrt(3.0) * LjNj_bp)) - 2.0 *
RjNj_bp / Nj_bp); // Eq.114 in [236]
                }
                else { sigmaBp = 0; }
                if (yesShear == 1) {
```

```
          sigmaSh = taylorFactor * currentShearModulus * sqrt(LjNj_sh *
shearConstantStrength[i] * shearConstantStrength[i] * shearConstantStrength[i] /
(2.0 * tensionLineConstant * burgersNorm)) * pow(RjNj_sh / Nj_sh, 1.5); // Eq.
115
        }
        else { sigmaSh = 0; }
      }
      else if (PathStructure[i] == 1) //squarePath)(regularpath)
      {
        // compute sigmaBp and sigmaSh for this precipitate(square path)
        if (yesByPass == 1) {
          sigmaBp = 2.0 * taylorFactor * tensionLineConstant *
currentShearModulus * burgersNorm / (sqrt(1.0 / LjNj_bp) - 2.0 * RjNj_bp /
Nj_bp); // Eq.118 in [236]
        }
        else { sigmaBp = 0; }
        if (yesShear == 1) {
          sigmaSh = taylorFactor * currentShearModulus * sqrt(LjNj_sh *
shearConstantStrength[i] * shearConstantStrength[i] * shearConstantStrength[i] /
(2.0 * tensionLineConstant * burgersNorm)) * pow(RjNj_sh / Nj_sh, 1.5); // Eq.115
in [236]
        }
        else { sigmaSh = 0; }
      }
      else {
        error.Fatal("only 'triangularpath' and 'squarepath' are
implemented");
      }
    }

    else if (_Precipitates[i].GetShapeIndex() == 3) // plate
    {
      aspectRatio = _Precipitates[i].GetAspectRatio();
      for (size_t j = 0; j < _Precipitates[i].GetNumberOfClass(); j++) {
        Nj = _Precipitates[i].GetNumber(j);
        Rj = _Precipitates[i].GetRadius(j);
        Tj = 2*Rj/aspectRatio;
        if (Rj >= transitionRadius[i]) {
          //by passing
          TjNj_bp += Tj * Nj;
          RjNj_bp = RjNj_bp + Rj * Nj;
          Nj_bp += Nj;
          yesByPass = 1;
        }
        else {
          //shearing
          TjNj_sh = TjNj_sh + Tj * Nj;
          RjNj_sh = RjNj_sh + Rj * Nj;
          Nj_sh += Nj;
          yesShear = 1;
        }
      }
      if (PathStructure[i] == 2) //triangularPath
      {
        //compute sigmaBp and sigmaSh for this precipitate (triangular
path)
        if (yesByPass == 1) {
          sigmaBp = 2.0 * taylorFactor * tensionLineConstant *
currentShearModulus * burgersNorm / (sqrt(2.0 / (sqrt(3.0) * TjNj_bp)) - 2.0 *
RjNj_bp / Nj_bp); // Eq.165 in [236]
        }
        else { sigmaBp = 0; }
```

```
                if (yesShear == 1) {
                    sigmaSh = taylorFactor * currentShearModulus * sqrt(TjNj_sh *
shearConstantStrength[i] * shearConstantStrength[i] * shearConstantStrength[i] /
(2.0 * tensionLineConstant * burgersNorm)) * pow(RjNj_sh / Nj_sh, 1.5); // Eq.164
                }
                else { sigmaSh = 0; }
            }
            else if (PathStructure[i] == 1) //squarePath)(regularpath)
            {
                // compute sigmaBp and sigmaSh for this precipitate(square path)
                if (yesByPass == 1) {
                    sigmaBp = 2.0 * taylorFactor * tensionLineConstant *
currentShearModulus * burgersNorm / (sqrt(1.0 / TjNj_bp) - 2.0 * RjNj_bp /
Nj_bp); // Eq.166 in [236]
                }
                else { sigmaBp = 0; }
                if (yesShear == 1) {
                    sigmaSh = taylorFactor * currentShearModulus * sqrt(TjNj_sh *
shearConstantStrength[i] * shearConstantStrength[i] * shearConstantStrength[i] /
(2.0 * tensionLineConstant * burgersNorm)) * pow(RjNj_sh / Nj_sh, 1.5); // Eq.164
in [236]
                }
                else { sigmaSh = 0; }
            }
            else {
                error.Fatal("only 'triangularpath' and 'squarepath' are
implemented");
            }
        }
        else
            {
                error.Fatal("only 'rod' and 'plate' are implemented"); // error
            }


        //computation of sigmaPreciI and total "sigmaPrecipitates (that is the
quadratic sum of each precipitates contribution)
        sigmaTempI = sqrt(sigmaSh * sigmaSh + sigmaBp * sigmaBp);
        sigmaPreciItemp.push_back(sigmaTempI);
        sigmaPreciTemp = sigmaPreciTemp + sigmaTempI * sigmaTempI;

        //update attribut of class for precipitates
        dsigmaPreciI[i] = (sigmaTempI - sigmaPreciI[i]) / _dt;
        sigmaPreciI[i] = sigmaTempI;
        sigmaPreciIsh[i] = sigmaSh;
        sigmaPreciIbp[i] = sigmaBp;


    }
    sigmaPreciTemp = sqrt(sigmaPreciTemp);

    //-------------------- final stress ---------------------
    double sigmaFlowMicroTemp = initialYield + sigmaSSTemp + sqrt(sigmaDisloTemp
* sigmaDisloTemp + sigmaPreciTemp * sigmaPreciTemp);

    //#######################################################
    //###        update all global stress variables       ###
    //#######################################################
    dsigmaGrain = (sigmaGrainTemp - sigmaGrain) / _dt;
    dsigmaDislo = (sigmaDisloTemp - sigmaDislo) / _dt;     dsigmaSS =
(sigmaSSTemp - sigmaSS) / _dt;
```

```
    dsigmaPreci = (sigmaPreciTemp - sigmaPreci) / _dt;     dsigmaFlowMicro =
(sigmaFlowMicroTemp - sigmaFlowMicro) / _dt;
    sigmaDislo = sigmaDisloTemp;                       sigmaSS = sigmaSSTemp;
    sigmaPreci = sigmaPreciTemp;                       sigmaFlowMicro =
sigmaFlowMicroTemp;
    sigmaGrain = sigmaGrainTemp;
    //#######################################################
}


void Mechanical::ModelYi_hcp_prismatic(Matrix const& _matrix, vector<Element>
const& _Elements, vector<Precipitate> const& _Precipitates, double _currentTime,
double _dt)
{
    if (structure != 2) { error.Fatal("In model 8 just 'hcp' structure is
considered"); }
    //###################################################################
    //###                (Yi's model_prismatic slip)                  ###
    //###################################################################

    //------------------- load constant ---------------------
    currentYoung = GetYoung();
    currentPoisson = GetPoisson();
    currentShearModulus = currentYoung / (2.0 * (1.0 + currentPoisson));
    //----------- compute SS & dislo contributions  ---------
    double sigmaDisloTemp = ComputeDisloContributionModel1();
    double sigmaSSTemp = ComputeSScontributionModel1(_Elements);

    //-------------- precipitate contribution --------------
    //initialization
    double sigmaGrainTemp=0.;
    double sigmaPreciTemp = 0., sigmaBp = 0., sigmaSh = 0., LjNj_bp = 0., LjNj_sh
= 0., RjNj_bp = 0., RjNj_sh = 0., TjNj_bp = 0., TjNj_sh = 0., sumNj = 0., Rj_e =
0.;
    double aspectRatio = 0., Nj = 0., Rj = 0., Lj = 0., Tj = 0, sigmaTempI = 0.,
Lc = 0., Ltemp = 0., Rc = 0., Rtemp = 0., TjRjNj_sh = 0., LjRjNj_sh =
0.;//,shearConstantStrength=0.;
    double fv_bp_temp = 0., meanR_bp_temp = 0., meanL_BP_temp = 0., Nj_bp, Nj_sh,
distanceBetweenPPT_temp = 0.;
    double distancePPTsh_temp = 1e300, distancePPTbp_temp = 1e300,
distancePPTall_temp = 1e300;

    vector<double> sigmaPreciItemp; sigmaPreciItemp.clear();
    int yesShear = 0, yesByPass = 0;

//tension line
    //double tensionLine = tensionLineConstant * currentShearModulus *
burgersNorm * burgersNorm;
    //-------------- initialisation for precipitate constants ---------------
    //stress contribution for each precipitates
    for (size_t i = 0; i < _Precipitates.size(); i++) { //different precipitate
kinds, e.g. b'1 and b'2
        //------------------------------------------
        yesShear = 0; yesByPass = 0;
        //read transition radius and compute shearConstantStrength
        // If a null value of k is in input, k is calculated via the critical
radius
        if (shearConstantStrength[i] == 0) {
            shearConstantStrength[i] = 2 * tensionLineConstant * burgersNorm /
transitionRadius[i];

        }
```

```
        //read transition radius and compute shearConstantStrength

        sigmaBp = 0., sigmaSh = 0., LjNj_bp = 0., LjNj_sh = 0., RjNj_bp = 0.,
RjNj_sh = 0., TjNj_bp = 0., TjNj_sh = 0., sumNj = 0., Nj = 0., Rj = 0., Lj = 0.;
        fv_bp_temp = 0.; meanR_bp_temp = 0.; meanL_BP_temp = 0.; Nj_bp = 0.;
Nj_sh = 0.; Tj = 0.; Rj_e = 0.; Ltemp=0., Lc=0., Rc = 0., Rtemp = 0., TjRjNj_sh =
0., LjRjNj_sh = 0.;// re-initialize after loop

        if (_Precipitates[i].GetShapeIndex() == 2) // rod
        {
            aspectRatio = _Precipitates[i].GetAspectRatio();
            for (size_t j = 0; j < _Precipitates[i].GetNumberOfClass(); j++) {
                Nj = _Precipitates[i].GetNumber(j);
                Rj = _Precipitates[i].GetRadius(j);
                Lj = Rj * aspectRatio;
                Rj_e = sqrt(Rj*Lj/2);
                if (Rj_e >= transitionRadius[i]) {
                    //by passing
                    LjNj_bp += Lj * Nj;
                    RjNj_bp = RjNj_bp + Rj * Nj;
                    Nj_bp += Nj;
                    yesByPass = 1;
                }
                else {
                    //shearing
                    LjNj_sh = LjNj_sh + Lj * Nj;
                    RjNj_sh = RjNj_sh + Rj * Nj;
                    LjRjNj_sh += Lj * Rj * Nj;
                    Nj_sh += Nj;
                    yesShear = 1;
                }
            }
            if (PathStructure[i] == 2) //triangularPath
            {
                //compute sigmaBp and sigmaSh for this precipitate (triangular
path)
                if (yesByPass == 1 && Rj > 0) {
                    Lc = (sqrt(3) / 2.0) * sqrt(2.0 / (sqrt(3.0) * 2.0 *
RjNj_bp));//critical length that changes expression for stress increment
calculation
                    Ltemp = LjNj_bp / Nj_bp;
                    if (Ltemp < Lc) {
                        sigmaBp = 2.0 * taylorFactor * tensionLineConstant *
currentShearModulus * burgersNorm / sqrt((sqrt(sqrt(3.0) / (4.0 * RjNj_bp)) -
LjNj_bp / Nj_bp) * (sqrt(sqrt(3.0) / (4.0 * RjNj_bp)) - LjNj_bp / Nj_bp) +
(sqrt(1 / (4.0 * sqrt(3.0) * RjNj_bp)) - (M_PI / 2.0) * (RjNj_bp / Nj_bp)) *
(sqrt(1 / (4.0 * sqrt(3.0) * RjNj_bp)) - (M_PI / 2.0) * (RjNj_bp / Nj_bp))); //
Eq.124 in [236]
                    }
                    else {
                        sigmaBp = 4.0 * taylorFactor * tensionLineConstant *
currentShearModulus * burgersNorm / sqrt(2.0 / (sqrt(3.0) * 2.0 *
RjNj_bp));//Eq.125 in [236]
                    }

                }
                else { sigmaBp = 0; }
                if (yesShear == 1 && Rj > 0) {
                    sigmaSh = taylorFactor * currentShearModulus * sqrt(RjNj_sh *
shearConstantStrength[i] * shearConstantStrength[i] * shearConstantStrength[i] /
(tensionLineConstant * burgersNorm)) * pow(LjRjNj_sh / (2.0 * Nj_sh), 3.0 / 4.0);
// Eq.126
```

```
                }
                else { sigmaSh = 0; }
            }
            else if (PathStructure[i] == 1) //squarePath)(regularpath)
            {
                // compute sigmaBp and sigmaSh for this precipitate(square path)
                if (yesByPass == 1) {
                    sigmaBp = 2.0 * taylorFactor * tensionLineConstant *
currentShearModulus * burgersNorm / (sqrt(1.0 / (2.0 * RjNj_bp)) - LjNj_bp /
Nj_bp); // Eq.128 in [236]
                }
                else { sigmaBp = 0; }
                if (yesShear == 1) {
                    sigmaSh = taylorFactor * currentShearModulus * sqrt(RjNj_sh *
shearConstantStrength[i] * shearConstantStrength[i] * shearConstantStrength[i] /
(tensionLineConstant * burgersNorm)) * pow(LjRjNj_sh / (2.0 * Nj_sh), 3.0 / 4.0);
// Eq.126 in [236]
                }
                else { sigmaSh = 0; }
            }
            else {
                error.Fatal("only 'triangularpath' and 'squarepath' are
implemented");
            }
        }

        else if (_Precipitates[i].GetShapeIndex() == 3) // plate
        {
            aspectRatio =
_Precipitates[i].AspectRatioFromRodFunction(_Precipitates[i].MeanRadius());
            for (size_t j = 0; j < _Precipitates[i].GetNumberOfClass(); j++) {
                Nj = _Precipitates[i].GetNumber(j);
                Rj = _Precipitates[i].GetRadius(j);
                Tj = 2*Rj/aspectRatio;
                Rj_e = sqrt(Rj*Tj/2);
                if (Rj_e >= transitionRadius[i]) {
                    //by passing
                    TjNj_bp += Tj * Nj;
                    RjNj_bp = RjNj_bp + Rj * Nj;
                    Nj_bp += Nj;
                    yesByPass = 1;
                }
                else {
                    //shearing
                    TjNj_sh = TjNj_sh + Tj * Nj;
                    RjNj_sh = RjNj_sh + Rj * Nj;
                    TjRjNj_sh += Tj * Rj * Nj;
                    Nj_sh += Nj;
                    yesShear = 1;
                }
            }
            if (PathStructure[i] == 2) //triangularPath
            {
                //compute sigmaBp and sigmaSh for this precipitate (triangular
path)
                if (yesByPass == 1 && Rj > 0) {
                    Rc = (sqrt(3) / 2.0) * sqrt(2.0 / (sqrt(3.0) * 2.0 *
RjNj_bp)); // critical radius that changes expression for stress increment
calculation
                    Rtemp = (M_PI / 2.0) * (RjNj_bp / Nj_bp);
                    if (Rtemp < Rc) {
```

```
                        sigmaBp = 2.0 * taylorFactor * tensionLineConstant *
currentShearModulus * burgersNorm / sqrt((sqrt(sqrt(3.0) / 4.0 * RjNj_bp) - (M_PI
/ 2.0) * (RjNj_bp / Nj_bp)) * (sqrt(sqrt(3.0) / 4.0 * RjNj_bp) - (M_PI / 2.0) *
(RjNj_bp / Nj_bp)) + (sqrt(1.0 / (4.0 * sqrt(3.0) * RjNj_bp)) - TjNj_bp / Nj_bp)
* (sqrt(1.0 / (4.0 * sqrt(3) * RjNj_bp)) - TjNj_bp / Nj_bp)); // Eq.170 in [236]
                    }
                    else {
                        sigmaBp = 4.0 * taylorFactor * tensionLineConstant *
currentShearModulus * burgersNorm / sqrt(2.0 / (sqrt(3.0) * 2.0 * RjNj_bp));//
Eq. 171 in [236]
                    }

                }
                else { sigmaBp = 0; }
                if (yesShear == 1 && Rj > 0 && Tj > 0) {
                    sigmaSh = taylorFactor * currentShearModulus * sqrt(RjNj_sh *
shearConstantStrength[i] * shearConstantStrength[i] * shearConstantStrength[i] /
(tensionLineConstant * burgersNorm)) * pow(TjRjNj_sh / (2.0 * Nj_sh), 3.0 /
4.0);// Eq.172 in [236]
                }
                else { sigmaSh = 0; }
            }
            else if (PathStructure[i] == 1) //squarePath)(regularpath)
            {
                // compute sigmaBp and sigmaSh for this precipitate(square path)
                if (yesByPass == 1) {
                    sigmaBp = 2.0 * taylorFactor * tensionLineConstant *
currentShearModulus * burgersNorm / (sqrt(1.0 / (2.0 * RjNj_bp)) - (M_PI / 2.0) *
(RjNj_bp / Nj_bp)); // Eq.174 in [236]
                }
                else { sigmaBp = 0; }
                if (yesShear == 1 && Rj > 0) {
                    sigmaSh = taylorFactor * currentShearModulus * sqrt(RjNj_sh *
shearConstantStrength[i] * shearConstantStrength[i] * shearConstantStrength[i] /
(tensionLineConstant * burgersNorm)) * pow(TjRjNj_sh / (2.0 * Nj_sh), 3.0 /
4.0);// Eq.172 in [236]
                }
                else { sigmaSh = 0; }
            }
            else {
                error.Fatal("only 'triangularpath' and 'squarepath' are
implemented");
            }
        }
        else
        {
            error.Fatal("only 'rod' and 'plate' are implemented"); // error
        }
//computation of sigmaPreciI and total "sigmaPrecipitates (that is the quadratic
sum of each precipitates contribution)
        sigmaTempI = sqrt(sigmaSh * sigmaSh + sigmaBp * sigmaBp);
        sigmaPreciItemp.push_back(sigmaTempI);
        sigmaPreciTemp = sigmaPreciTemp + sigmaTempI * sigmaTempI;

        //update attribut of class for precipitates
        dsigmaPreciI[i] = (sigmaTempI - sigmaPreciI[i]) / _dt;
        sigmaPreciI[i] = sigmaTempI;
        sigmaPreciIsh[i] = sigmaSh;
        sigmaPreciIbp[i] = sigmaBp;


    }
```

```
    sigmaPreciTemp = sqrt(sigmaPreciTemp);

    //-------------------- final stress ---------------------
    double sigmaFlowMicroTemp = initialYield + sigmaSSTemp + sqrt(sigmaDisloTemp
* sigmaDisloTemp + sigmaPreciTemp * sigmaPreciTemp);

    //#######################################################
    //###        update all global stress variables       ###
    //#######################################################
    dsigmaGrain = (sigmaGrainTemp - sigmaGrain) / _dt;
    dsigmaDislo = (sigmaDisloTemp - sigmaDislo) / _dt;     dsigmaSS =
(sigmaSSTemp - sigmaSS) / _dt;
    dsigmaPreci = (sigmaPreciTemp - sigmaPreci) / _dt;     dsigmaFlowMicro =
(sigmaFlowMicroTemp - sigmaFlowMicro) / _dt;
    sigmaDislo = sigmaDisloTemp;                       sigmaSS = sigmaSSTemp;
    sigmaPreci = sigmaPreciTemp;                       sigmaFlowMicro =
sigmaFlowMicroTemp;
    sigmaGrain = sigmaGrainTemp;
    //#######################################################
}

void Mechanical::ModelYi_hcp_twinning(Matrix const& _matrix, vector<Element>
const& _Elements, vector<Precipitate> const& _Precipitates, double _currentTime,
double _dt)
{
       if (structure != 2) { error.Fatal("In model 9 just 'hcp' structure is
considered"); }
       //####################################################################
       //###                   (Yi's model_twinning)                      ###
    //###                    Barnet et al.2018                        ###
       //####################################################################

       //------------------- load constant ---------------------
       currentYoung = GetYoung();
       currentPoisson = GetPoisson();
       currentShearModulus = currentYoung / (2 * (1 + currentPoisson));
       //----------- compute SS & dislo contributions  ---------
       double sigmaDisloTemp = ComputeDisloContributionModel1();
       double sigmaSSTemp = ComputeSScontributionModel1(_Elements);

       //-------------- precipitate contribution --------------
       //initialization
    double sigmaGrainTemp = 0.;
       double sigmaPreciTemp = 0., sigmaBp = 0., sigmaSh = 0., LjNj_bp = 0.,
RjNj_bp = 0., TjNj_bp = 0., sumNj = 0., TjRjNj_bp = 0., Lprime_rod = 0.,
Dprime_plate = 0., Rj_e = 0.;
       double aspectRatio = 0., Nj = 0., Rj = 0., Lj = 0., Tj = 0, sigmaTempI =
0.;//,shearConstantStrength=0.;
       double fv_bp_temp = 0., meanR_bp_temp = 0., meanL_BP_temp = 0., Nj_bp,
Nj_sh, distanceBetweenPPT_temp = 0.;
       double distancePPTsh_temp = 1e300, distancePPTbp_temp = 1e300,
distancePPTall_temp = 1e300;
       double distancetwinbp = 1e300, harmoD = 0., nb = 0., Ltwin = 0.,
TwinSurfaceEnergy = 0.12, ShearModule = 1.7e10, Poisson = 0.33, burgerstwin =
4.9e-11, b0 = 2.2e-10, Tau0 = 25000000.0;
    double sinPhi = 0., cosPhi = 0., LOG = 0;//sinPhi = 0.684, cosPhi = 0.73,

       vector<double> sigmaPreciItemp; sigmaPreciItemp.clear();
       int yesByPass = 0, yesShear = 0;
    sinPhi = sqrt(3) * aParameter / sqrt(cParameter * cParameter + 3 * aParameter
* aParameter); //Eq.110 in [236]
```

```
    cosPhi = cParameter / sqrt(cParameter * cParameter + 3 * aParameter *
aParameter); //Eq.111 in [236]

       //tension line
       //double tensionLine = tensionLineConstant * currentShearModulus *
burgersNorm * burgersNorm;
       //-------------- initialisation for precipitate constants ---------------
       //stress contribution for each precipitates
       for (size_t i = 0; i < _Precipitates.size(); i++) { //different
precipitate kinds, e.g. b'1 and b'2
              //----------------------------------------
        yesByPass = 1, yesShear = 0;
              //read transition radius and compute shearConstantStrength
              // If a null value of k is in input, k is calculated via the
critical radius
              if (shearConstantStrength[i] == 0) {
                     shearConstantStrength[i] = 2 * tensionLineConstant *
burgersNorm / transitionRadius[i];

              }
              //read transition radius and compute shearConstantStrength

              sigmaBp = 0., sigmaSh = 0., LjNj_bp = 0., RjNj_bp = 0., TjNj_bp =
0., sumNj = 0., Nj = 0., Rj = 0., Lj = 0., Rj_e = 0., LOG = 0.;
              fv_bp_temp = 0.; meanR_bp_temp = 0.; meanL_BP_temp = 0.; Nj_bp =
0.; Nj_sh = 0.; Tj = 0.; nb = 0., Ltwin = 0., harmoD = 0., TjRjNj_bp = 0.,
Lprime_rod = 0., Dprime_plate = 0.;// re-initialize after loop

              if (_Precipitates[i].GetShapeIndex() == 2) // rod
              {
                     aspectRatio = _Precipitates[i].GetAspectRatio();
                     for (size_t j = 0; j < _Precipitates[i].GetNumberOfClass();
j++) {
                            Nj = _Precipitates[i].GetNumber(j);
                            Rj = _Precipitates[i].GetRadius(j);
                if (2 * Rj >= burgerstwin * (1.25 * TwinSurfaceEnergy / (b0 *
Tau0)) * (1.25 * TwinSurfaceEnergy / (b0 * Tau0)) * (1.25 * TwinSurfaceEnergy /
(b0 * Tau0))) {
                    Rj = burgerstwin * (1.25 * TwinSurfaceEnergy / (b0 * Tau0)) *
(1.25 * TwinSurfaceEnergy / (b0 * Tau0)) * (1.25 * TwinSurfaceEnergy / (b0 *
Tau0)) - 0.000000001;
                }
                            Lj = Rj * aspectRatio;
                    //by passing
                    LjNj_bp += Lj * Nj;
                    RjNj_bp = RjNj_bp + Rj * Nj;
                    Lprime_rod += Nj * (2.0 * sinPhi * Rj + cosPhi * Lj);
                    Nj_bp += Nj;
                //}
                     }
            nb = b0* pow((2.0 * RjNj_bp / (burgerstwin * Nj_bp)) * sqrt(1.0 /
cosPhi), 1.0 / 3.0); // Eq.130
                     if (PathStructure[i] == 2) //triangularPath
                     {
                if (yesByPass == 1 && Rj > 0) {
                    //compute sigmaBp and sigmaSh for this precipitate
(triangular path)
                    Ltwin = sqrt(2.0 / (sqrt(3.0) * Lprime_rod)) - (2.0 * RjNj_bp
/ Nj_bp) * sqrt(1.0 / cosPhi); // Eq.132 in [236]
                    harmoD = 2.0 / (1.0 / Ltwin + 1.0 / ((2.0 * RjNj_bp / Nj_bp)
* sqrt(1.0 / cosPhi))); // Eq.133 in [236]
                    if (log(harmoD / nb) >= 0)
```

```
                    {
                        LOG = log(harmoD / nb);
                    }
                    else {
                        LOG = 0;
                    }
                    sigmaBp = (taylorFactor * Tau0 * ShearModule * nb * nb / (4 *
M_PI * sqrt(1 - Poisson) * TwinSurfaceEnergy * Ltwin)) * LOG; // Eq.99 in [236]
                    if (_currentTime > 1e5) {
                        sigmaBp = sigmaBp;
                }
                }
                else { sigmaBp = 0; }
                     }
                     else if (PathStructure[i] == 1) //squarePath)(regularpath)
                     {
                if (yesByPass == 1 && Rj > 0) {
                    Ltwin = sqrt(1 / Lprime_rod) - (2.0 * RjNj_bp / Nj_bp) *
sqrt(1.0 / cosPhi); // Eq.135 in [236]
                    harmoD = 2.0 / (1.0 / Ltwin + 1.0 / ((2.0 * RjNj_bp / Nj_bp)
* sqrt(1.0 / cosPhi))); // Eq.136 in [236]
                    if (log(harmoD / nb) >= 0)
                    {
                        LOG = log(harmoD / nb);
                    }
                    else {
                        LOG = 0;
                    }
                    sigmaBp = (taylorFactor * Tau0 * ShearModule * nb * nb / (4 *
M_PI * sqrt(1 - Poisson) * TwinSurfaceEnergy * Ltwin)) * LOG; // Eq.99 in [236]
                }
                else { sigmaBp = 0; }
                     }
                     else {
                            error.Fatal("only 'triangularpath' and 'squarepath'
are implemented");
                     }
              }
else
              {

            sigmaBp = 0;
              }


              //computation of sigmaPreciI and total "sigmaPrecipitates (that is
the quadratic sum of each precipitates contribution)
        sigmaTempI = sqrt(sigmaSh * sigmaSh + sigmaBp * sigmaBp);
        sigmaPreciItemp.push_back(sigmaTempI);
        sigmaPreciTemp = sigmaPreciTemp + sigmaTempI * sigmaTempI;

              //update attribut of class for precipitates
              dsigmaPreciI[i] = (sigmaTempI - sigmaPreciI[i]) / _dt;
              sigmaPreciI[i] = sigmaTempI;
        sigmaPreciIsh[i] = sigmaSh;
              sigmaPreciIbp[i] = sigmaBp;


       }
       sigmaPreciTemp = sqrt(sigmaPreciTemp);

       //-------------------- final stress ---------------------
```

```
       double sigmaFlowMicroTemp = initialYield + sigmaSSTemp +
sqrt(sigmaDisloTemp * sigmaDisloTemp + sigmaPreciTemp * sigmaPreciTemp);

       //########################################################
       //###        update all global stress variables       ###
       //########################################################
       dsigmaGrain = (sigmaGrainTemp - sigmaGrain) / _dt;
       dsigmaDislo = (sigmaDisloTemp - sigmaDislo) / _dt;     dsigmaSS =
(sigmaSSTemp - sigmaSS) / _dt;
       dsigmaPreci = (sigmaPreciTemp - sigmaPreci) / _dt;     dsigmaFlowMicro =
(sigmaFlowMicroTemp - sigmaFlowMicro) / _dt;
       sigmaDislo = sigmaDisloTemp;                       sigmaSS = sigmaSSTemp;
       sigmaPreci = sigmaPreciTemp;                       sigmaFlowMicro =
sigmaFlowMicroTemp;
       sigmaGrain = sigmaGrainTemp;
       //########################################################
}
```

Reference

1. M. Easton, A. Beer, M. Barnett, C. Davies, G. Dunlop, Y. Durandet, S. Blacket, T. Hilditch, P. Beggs, *Magnesium alloy applications in automotive structures.* Jom, 2008. **60**(11): 57.
2. J. Hirsch, T. Al-Samman, *Superior light metals by texture engineering: Optimized aluminum and magnesium alloys for automotive applications.* Acta Materialia, 2013. **61**(3): 818-843.
3. W.J. Joost, P.E. Krajewski, *Towards magnesium alloys for high-volume automotive applications.* Scripta Materialia, 2017. **128**: 107-112.
4. S. Zhang, X. Zhang, C. Zhao, J. Li, Y. Song, C. Xie, H. Tao, Y. Zhang, Y. He, Y. Jiang, Y. Bian, *Research on an Mg–Zn alloy as a degradable biomaterial.* Acta Biomaterialia, 2010. **6**(2): 626-640.
5. C. Bettles, M.J.J. Gibson, *Current wrought magnesium alloys: strengths and weaknesses.* 2005. **57**(5): 46-49.
6. C. EduPack, *The Cambridge Engineering Selector.* Granta Design, Rustat House, 2007.
7. A. Ardell, *Precipitation hardening.* Metallurgical Transactions A, 1985. **16**(12): 2131-2165.
8. J. Clark, L. Zabdyr, Z. Moser, *Phase diagrams of binary magnesium alloys.* ASM International, Materials Park, OH, 1988: 353-364.
9. J.F. Nie, *Effects of precipitate shape and orientation on dispersion strengthening in magnesium alloys.* Scripta Materialia, 2003. **48**(8): 1009-1015.
10. J.D. Robson, N. Stanford, M.R. Barnett, *Effect of precipitate shape on slip and twinning in magnesium alloys.* Acta Materialia, 2011. **59**(5): 1945-1956.
11. M. Barnett, N. Stanford, P. Cizek, A. Beer, Z. Xuebin, Z. Keshavarz, *Deformation mechanisms in Mg alloys and the challenge of extending room-temperature plasticity*. Jom, 2009. **61**(8): 19-24.
12. J.D. Robson, N. Stanford, M.R. Barnett, *Effect of precipitate shape and habit on mechanical asymmetry in magnesium alloys.* Metallurgical and Materials Transactions A, 2013. **44**(7): 2984-2995.
13. M.R. Barnett, A. Ghaderi, J.D. Robson, *Contribution of Twinning to Low Strain Deformation in a Mg Alloy.* Metallurgical and Materials Transactions A, 2013. **45**(8): 3213-3221.

14. D.A. Porter, K.E. Easterling, *Phase transformations in metals and alloys (revised reprint)*. 2009: CRC press.

15. W.D. Callister, D.G. Rethwisch, *Materials science and engineering: an introduction*. Vol. 9. 2018: Wiley New York.

16. R. Wagner, R. Kampmann, *Chapter 9: Homogeneous Second Phase Precipitations, Volume 5; Vol. ed.: P. Haasen: Phase Transformations in Materials of Materials Science and Technology—A Comprehensive Treatment, Ser. eds.: RW Cahn, P. Haasen, and EJ Krämer*. 1991, VCH, Weinheim.

17. J. Nie, *Precipitation and hardening in magnesium alloys.* Metallurgical and Materials Transactions A, 2012. **43**(11): 3891-3939.

18. M. Perez, M. Dumont, D.J.A.m. Acevedo-Reyes, *Implementation of classical nucleation and growth theories for precipitation.* 2008. **56**(9): 2119-2132.

19. M. Pereza, M. Dumontb, D. Acevedo-Reyesc, *Corrigendum to ''Implementation of classical nucleation and growth theories for precipitation"[Acta Materialia 56 (2008) 2119–2132].* Acta Materialia, 2009. **57**: 1318-1318.

20. C. Zener, *Theory of growth of spherical precipitates from solid solution.* Journal of applied physics, 1949. **20**(10): 950-953.

21. M. Perez, *Gibbs–Thomson effects in phase transformations.* Scripta Materialia, 2005. **52**(8): 709-712.

22. A. Baldan, *Review progress in Ostwald ripening theories and their applications to nickel-base superalloys Part I: Ostwald ripening theories.* Journal of materials science, 2002. **37**(11): 2171-2202.

23. K. Russell, *Precipitate coarsening and grain growth in steels.* Massachusetts Institute of Technology, 2003. **77**: 1.

24. G. Greenwood, *The growth of dispersed precipitates in solutions.* Acta metallurgica, 1956. **4**(3): 243-248.

25. C. Wagner, *Theory of precipitate change by redissolution.* Z. Elektrochem, 1961. **65**: 581-591.

26. I.M. Lifshitz, V.V. Slyozov, *The kinetics of precipitation from supersaturated solid solutions.* Journal of physics & chemistry of solids, 1961. **19**(1-2): 35-50.

27. C. Sigli, F. De Geuser, A. Deschamps, J. Lépinoux, M. Perez, *Recent advances in the metallurgy of aluminum alloys. Part II: Age hardening.* Comptes Rendus Physique, 2018. **19**(8): 688-709.

28. J. Cahn, G. Kalonji. *Symmetry in solid state transformation morphologies*. in *Proceedings of an international conference on solidsolid phase transformations. Warrendale (PA): The Metallurgical Society of AIME*. 1982.

29. A. Ardell, R.B. Nicholson, *On the modulated structure of aged Ni-Al alloys: with an Appendix On the elastic interaction between inclusions by JD Eshelby.* Acta metallurgica, 1966. **14**(10): 1295-1309.

30. M. Doi, T. Miyazaki, T. Wakatsuki, *The effects of elastic interaction energy on the γ' precipitate morphology of continuously cooled nickel-base alloys.* Materials Science & Engineering, 1985. **74**(2): 139-145.

31. U. Glatzel, M. Feller-Kniepmeier, *Calculations of internal stresses in the γ/γ' microstructure of a nickel-base superalloy with high volume fraction of γ'-phase.* Scripta metallurgica, 1989. **23**(11): 1839-1844.

32. M. Kaufman, P. Voorhees, W.C. Johnson, F. Biancaniello, *An elastically induced morphological instability of a misfitting precipitate.* Metallurgical Transactions A, 1989. **20**(10): 2171-2175.

33. T. Miyazaki, H. Imamura, T. Kozakai, *The formation of "γ' precipitate doublets" in Ni-Al alloys and their energetic stability.* Materials Science & Engineering, 1982. **54**(1): 9-15.

34. A. Khachaturyan, *Theory of structural transformations in solids Wiley*. New York. transforms, 1983. **16**.

35. W. Johnson, P. Voorhees. *Elastically-induced precipitate shape transitions in coherent solids*. in *Solid state phenomena*. 1992. Trans Tech Publ.

36. A. Khachaturyan, S. Semenovskaya, J. Morris Jr, *Theoretical analysis of strain-induced shape changes in cubic precipitates during coarsening.* Acta Metallurgica, 1988. **36**(6): 1563-1572.

37. M. Thompson, C. Su, P.W. Voorhees, *The equilibrium shape of a misfitting precipitate.* Acta metallurgica et materialia, 1994. **42**(6): 2107-2122.

38. P.W. Voorhees, G. McFadden, W. Johnson, *On the morphological development of second-phase particles in elastically-stressed solids.* Acta Metallurgica et Materialia, 1992. **40**(11): 2979-2992.

39. Q. Wang, Z. Li, S. Pang, X. Li, C. Dong, P.K. Liaw, *Coherent precipitation and strengthening in compositionally complex alloys: a review.* Entropy, 2018. **20**(11): 878.

40. J.B. Clark, *Age hardening in a Mg-9 wt.% Al alloy.* Acta Metallurgica, 1968. **16**(2): 141-152.

41. P. Paufler, *P. Villars, LD Calvert. Pearson's handbook of crystallographic data for intermetallic phases. American Society for Metals. Metals Park. Ohio. 1986. Vols. 1–3. 3258 pp, US $495.00 ISBN 0-87170-217-7.* Crystal Research and Technology, 1987. **22**(11): 1436-1436.

42. J.F. Nie, K. Oh-ishi, X. Gao, K. Hono, *Solute segregation and precipitation in a creep-resistant Mg–Gd–Zn alloy.* Acta Materialia, 2008. **56**(20): 6061-6076.

43. Y.M. Zhu, A.J. Morton, J.F. Nie, *The 18R and 14H long-period stacking ordered structures in Mg–Y–Zn alloys.* Acta Materialia, 2010. **58**(8): 2936-2947.

44. C.R. Hutchinson, J. Nie, S. Gorsse, *Modeling the precipitation processes and strengthening mechanisms in a Mg-Al-(Zn) AZ91 alloy.* Metallurgical and Materials Transactions A, 2005. **36**(8): 2093-2105.

45. S. Agnew, R. Mulay, F. Polesak Iii, C. Calhoun, J. Bhattacharyya, B. Clausen, *In situ neutron diffraction and polycrystal plasticity modeling of a Mg–Y–Nd–Zr alloy: effects of precipitation on individual deformation mechanisms.* Acta Materialia, 2013. **61**(10): 3769-3780.

46. J. Clark, *Transmission electron microscopy study of age hardening in a Mg-5 wt.% Zn alloy.* Acta Metallurgica, 1965. **13**(12): 1281-1289.

47. A. Crawley, B. Lagowski, *Effect of two-step ageing on the precipitate structure in magnesium alloy AZ91.* Metallurgical Transactions, 1974. **5**(4): 949-951.

48. J. Nie, X. Xiao, C. Luo, B.C. Muddle, *Characterisation of precipitate phases in magnesium alloys using electron microdiffraction.* Micron, 2001. **32**(8): 857-863.

49. J. Buha, *Reduced temperature (22–100° C) ageing of an Mg–Zn alloy.* Materials Science and Engineering: A, 2008. **492**(1-2): 11-19.

50. J. Buha, *The effect of micro-alloying addition of Cr on age hardening of an Mg–Zn alloy.* Materials Science and Engineering: A, 2008. **492**(1-2): 293-299.

51. J. Buha, *The effect of Ba on the microstructure and age hardening of an Mg–Zn alloy.* Materials Science and Engineering: A, 2008. **491**(1-2): 70-79.

52. O.B.M. Hardouin Duparc, *The Preston of the Guinier-Preston Zones. Guinier.* Metallurgical and Materials Transactions B, 2010. **41**(5): 925-934.

53. Z.R. Zeng, Y.M. Zhu, M.Z. Bian, S.W. Xu, C.H.J. Davies, N. Birbilis, J.F. Nie, *Annealing strengthening in a dilute Mg–Zn–Ca sheet alloy.* Scripta Materialia, 2015. **107**: 127-130.

54. T. Bhattacharjee, C.L. Mendis, K. Oh-ishi, T. Ohkubo, K. Hono, *The effect of Ag and Ca additions on the age hardening response of Mg–Zn alloys.* Materials Science and Engineering: A, 2013. **575**: 231-240.

55. J. Buha, T. Ohkubo, *Natural ageing in Mg-Zn (-Cu) alloys.* Metallurgical and materials transactions A, 2008. **39**(9): 2259.

56. D. Wang, M. Amsler, V.I. Hegde, J.E. Saal, A. Issa, B.-C. Zhou, X. Zeng, C. Wolverton, *Crystal structure, energetics, and phase stability of strengthening precipitates in Mg alloys: A first-principles study.* Acta Materialia, 2018. **158**: 65-78.

57. L. Binjiang, P. Jian, T. Xiaoshan, P. Fusheng, *Effects of Extruding Temperature on Microstructure and Mechanical Properties of Mg-2.0 Zn-0.3 Zr-0.9 Y Alloy.* Rare Metal Materials and Engineering, 2013. **42**(4): 841-844.

58. J. Chun, J. Byrne, A. Bornemann, *The inhibition of deformation twinning by precipitates in a magnesium-zinc alloy.* Philosophical Magazine, 1969. **20**(164): 291-300.

59. L. Wei, G. Dunlop, H. Westengen, *Precipitation hardening of Mg-Zn and Mg-Zn-RE alloys.* Metallurgical and Materials Transactions A, 1995. **26**(7): 1705-1716.

60. J. Gallot, R. Graf, *Nouvelles observations aux rayons x et au microscope electronique sur la phase transitoire appraissant dans lalliage magnesiumzinc a 6 (de zinc.* Comptes Rendus Hebdomadaires Des Seances De L Academie Des Sciences, 1965. **261**(3): 728-&.

61. J. Gallot, A. Guinier, K. Lal, R. Graf, *EPrecipitation hardeningtude aux rayons x des phenomenes de precipitation dans un alliage magnesium-zinc a 6 percent de zinc.* Comptes Rendus Hebdomadaires Des Seances De L Academie Des Sciences, 1964. **258**(10): 2818-&.

62. L. Sturkey, J. Clark, *Mechanism of age-hardening in magnesium zinc alloys.* Journal of the Institute of Metals, 1959. **88**(4): 177-181.

63. J. Chun, J. Byrne, *Precipitate strengthening mechanisms in magnesium zinc alloy single crystals.* Journal of Materials Science, 1969. **4**(10): 861-872.

64. X. Gao, J.F. Nie, *Characterization of strengthening precipitate phases in a Mg–Zn alloy.* Scripta Materialia, 2007. **56**(8): 645-648.

65. A. Singh, A. Tsai, *Structural characteristics of β1' precipitates in Mg–Zn-based alloys.* Scripta Materialia, 2007. **57**(10): 941-944.

66. A. Singh, J.M. Rosalie, H. Somekawa, T. Mukai, *The structure of precipitates in Mg–Zn–Y alloys.* Philosophical Magazine Letters, 2010. **90**(9): 641-651.

67. J.M. Rosalie, H. Somekawa, A. Singh, T. Mukai, *Structural relationships among MgZn2 and Mg4Zn7 phases and transition structures in Mg-Zn-Y alloys.* Philosophical Magazine, 2010. **90**(24): 3355-3374.

68. J.M. Rosalie, H. Somekawa, A. Singh, T. Mukai, *Orientation relationships between icosahedral clusters in hexagonal MgZn2 and monoclinic Mg4Zn7 phases in Mg-Zn (-Y) alloys.* Philosophical Magazine, 2011. **91**(19-21): 2634-2644.

69. J.M. Rosalie, B.R. Pauw, *Form-free size distributions from complementary stereological TEM/SAXS on precipitates in a Mg–Zn alloy.* Acta materialia, 2014. **66**: 150-162.

70. X. Gao, J.F. Nie, *Structure and thermal stability of primary intermetallic particles in an Mg–Zn casting alloy.* Scripta Materialia, 2007. **57**(7): 655-658.

71. P. Blanco-Rodriguez, J. Rodriguez-Aseguinolaza, E. Risueno, M. Tello, *Thermophysical characterization of Mg–51% Zn eutectic metal alloy: a phase change material for thermal energy storage in direct steam generation applications.* Energy, 2014. **72**: 414-420.

72. N.C. Verissimo, C. Brito, C.R. Afonso, J.E. Spinelli, N. Cheung, A. Garcia, *Microstructure characterization of a directionally solidified Mg-12wt.% Zn alloy: Equiaxed dendrites, eutectic mixture and type/morphology of intermetallics.* Materials Chemistry and Physics, 2018. **204**: 105-131.

73. L. Wei, G. Dunlop, H. Westengen, *Precipitation hardening of Mg-Zn and Mg-Zn-RE alloys.* Metallurgical & Materials Transactions A, 1995. **26**(7): 1705-1716.

74. M. Karlík, A. Bigot, B. Jouffrey, P. Auger, S. Belliot, *HREM, FIM and tomographic atom probe investigation of Guinier–Preston zones in an Al–1.54 at% Cu alloy.* Ultramicroscopy, 2004. **98**(2-4): 219-230.

75. K.E. Knipling, R.A. Karnesky, C.P. Lee, D.C. Dunand, D.N. Seidman, *Precipitation evolution in Al–0.1 Sc, Al–0.1 Zr and Al–0.1 Sc–0.1 Zr (at.%) alloys during isochronal ageing.* Acta Materialia, 2010. **58**(15): 5184-5195.

76. J.M. Rosalie, H. Somekawa, A. Singh, T. Mukai, *The effect of size and distribution of rod-shaped β1′ precipitates on the strength and ductility of a Mg–Zn alloy.* Materials Science and Engineering: A, 2012. **539**: 230-237.

77. J.M. Rosalie, H. Somekawa, A. Singh, T. Mukai, *Effect of precipitation on strength and ductility in a Mg–Zn–Y alloy.* Journal of alloys & compounds, 2013. **550**: 114-123.

78. C. LIU, M. SK, X. Qiang, C. Jianghua, T. FD, Z. Xiaodong, Z.H. W, *MALLADI SK, XU Qiang, CHEN Jiang-hua, TICHELAAR FD, ZHUGE Xiao-dong, ZANDBERGEN H W. In-situ STEM imageing of growth and phase change of individual CuAlX precipitates in Al alloy [J].* Scientific Reports, 2017. **7**(1): 2184.

79. F. De Geuser, A. Deschamps, *Precipitate characterisation in metallic systems by small-angle X-ray or neutron scattering.* Comptes Rendus Physique, 2012. **13**(3): 246-256.

80. A. Deschamps, F. De Geuser, *Quantitative characterization of precipitate microstructures in metallic alloys using small-angle scattering.* Metallurgical & Materials Transactions A, 2013. **44**(1): 77-86.

81. E. Gumbmann, F. De Geuser, C. Sigli, A. Deschamps, *Influence of Mg, Ag and Zn minor solute additions on the precipitation kinetics and strengthening of an Al-Cu-Li alloy.* Acta Materialia, 2017. **133**: 172-185.

82. T. Dorin, A. Deschamps, F. De Geuser, W. Lefebvre, C. Sigli, *Quantitative description of the T1 formation kinetics in an Al–Cu–Li alloy using differential scanning calorimetry, small-angle X-ray scattering and transmission electron microscopy.* Philosophical magazine, 2014. **94**(10): 1012-1030.

83. S. Esmaeili, D. Lloyd, *Modeling of precipitation hardening in pre-aged AlMgSi (Cu) alloys.* Acta materialia, 2005. **53**(20): 5257-5271.

84. J. Jain, P. Cizek, W. Poole, M. Barnett, *Precipitate characteristics and their effect on the prismatic-slip-dominated deformation behaviour of an Mg–6 Zn alloy.* Acta materialia, 2013. **61**(11): 4091-4102.

85. N. Mo, I. McCarroll, Q. Tan, A. Ceguerra, Y. Liu, J. Cairney, H. Dieringa, Y. Huang, B. Jiang, F. Pan, *Understanding solid solution strengthening at elevated temperatures in a creep-resistant Mg–Gd–Ca alloy.* Acta Materialia, 2019. **181**: 185-199.

86. D.-H. Ping, K. Hono, J. Nie, *Atom probe characterization of plate-like precipitates in a Mg–RE–Zn–Zr casting alloy.* Scripta Materialia, 2003. **48**(8): 1017-1022.

87. T. Honma, T. Ohkubo, K. Hono, S. Kamado, *Chemistry of nanoscale precipitates in Mg–2.1 Gd–0.6 Y–0.2 Zr (at.%) alloy investigated by the atom probe technique.* Materials Science and Engineering: A, 2005. **395**(1-2): 301-306.
88. K. Oh-Ishi, C. Mendis, T. Ohkubo, K. Hono, *Effect of laser power and specimen temperature on atom probe analyses of magnesium alloys.* Ultramicroscopy, 2011. **111**(6): 715-718.
89. T. Honma, T. Ohkubo, K. Hono, S.J.M.S. Kamado, E. A, *Chemistry of nanoscale precipitates in Mg–2.1 Gd–0.6 Y–0.2 Zr (at.%) alloy investigated by the atom probe technique.* 2005. **395**(1-2): 301-306.
90. M. Perez, F. Perrard, V. Massardier, X. Kleber, A. Deschamps, H. De Monestrol, P. Pareige, G. Covarel, *Low-temperature solubility of copper in iron: experimental study using thermoelectric power, small angle X-ray scattering and tomographic atom probe.* Philosophical Magazine, 2005. **85**(20): 2197-2210.
91. M. Perez, V. Massardier, X. Kleber, *Thermoelectric power applied to metallurgy: principle and recent applications.* International journal of materials research, 2009. **100**(10): 1461-1465.
92. J. Pelletier, G. Vigier, J. Merlin, P. Merle, F. Fouquet, R. Borrelly, *Precipitation effects on thermopower in Al-Cu alloys.* Acta Metallurgica, 1984. **32**(7): 1069-1078.
93. G. Raynaud, P. Guyot, *Coherent precipitation effect on thermo-power of Al-Cu alloys.* Acta Metallurgica, 1988. **36**(1): 143-147.
94. W. Pearson, *Lattice spacings and structures of metals and alloys.* Vols. I & II, 1958.
95. Á. Filep, M. Sepsi. *Determination of solid solution composition in Al alloys by electrical transport properties measurement and XRD method*. in *IOP Conference Series: Materials Science and Engineering*. 2018. IOP Publishing.
96. C.L. Mendis, C.J. Bettles, M. Gibson, C. Hutchinson, *An enhanced age hardening response in Mg–Sn based alloys containing Zn.* Materials Science and Engineering: A, 2006. **435**: 163-171.
97. M. Akhlaghi, T. Steiner, S.R. Meka, A. Leineweber, E.J. Mittemeijer, *Lattice-parameter change induced by accommodation of precipitate/matrix misfit; misfitting nitrides in ferrite.* Acta Materialia, 2015. **98**: 254-262.

98. M. Akhlaghi, T. Steiner, S.R. Meka, E.J. Mittemeijer, *Misfit-induced changes of lattice parameters in two-phase systems: coherent/incoherent precipitates in a matrix.* Journal of Applied Crystallography, 2016. **49**(1): 69-77.

99. R. Wagner, R. Kampmann, P.W. Voorhees, *Homogeneous second-phase precipitation.* Phase transformations in materials, 2001: 309-407.

100. A. Deschamps, C. Hutchinson, *Precipitation kinetics in metallic alloys: Experiments and modeling.* Acta Materialia, 2021. **220**: 117338.

101. O. Myhr, Ø. Grong, *Modelling of non-isothermal transformations in alloys containing a particle distribution.* Acta Materialia, 2000. **48**(7): 1605-1615.

102. P. Maugis, M. Gouné, *Kinetics of vanadium carbonitride precipitation in steel: A computer model.* Acta materialia, 2005. **53**(12): 3359-3367.

103. C. Zhang, W. Cao, S.-L. Chen, J. Zhu, F. Zhang, A. Luo, R. Schmid-Fetzer, *Precipitation simulation of AZ91 alloy.* JOM, 2014. **66**(3): 389-396.

104. L. Rougier, A. Jacot, C.-A. Gandin, P.D. Napoli, P.-Y. Théry, D. Ponsen, V. Jaquet, *Numerical simulation of precipitation in multicomponent Ni-base alloys.* Acta Materialia, 2013. **61**(17): 6396-6405.

105. I.N. Khan, M.J. Starink, J.L. Yan, *A model for precipitation kinetics and strengthening in Al–Cu–Mg alloys.* Materials Science and Engineering: A, 2008. **472**(1): 66-74.

106. J.D. Robson, M.J. Jones, P.B. Prangnell, *Extension of the N-model to predict competing homogeneous and heterogeneous precipitation in Al-Sc alloys.* Acta Materialia, 2003. **51**(5): 1453-1468.

107. H. Aaronson, J. Lee, *The kinetic equations of solid: Solid nucleation theory and comparisons with experimental observations.* Lectures on the theory of phase transformations, 1999. **2**: 165-225.

108. R. Kampmann, R. Wagner, *Kinetics of Precipitation in Metastable Binary Alloys: Theory and Application to Copper--1. 9 at.% Titanium and Nickel--14 at.% Aluminium(Alloys).* Decomposition of alloys: the early stages, 1983: 91-103.

109. M. Perez, M. Dumont, D. Acevedo-Reyes, *Implementation of classical nucleation and growth theories for precipitation.* Acta Materialia, 2008. **56**(9): 2119-2132.

110. E. Kozeschnik, B. Buchmayr, *MatCalc–A simulation tool for multicomponent thermodynamics, Diffusion and Phase Transformation Kinetics*, in *Mathematical modelling of weld phenomena*. 2001, . 349-361.

111. W. Cao, S.L. Chen, F. Zhang, K. Wu, Y. Yang, Y.A. Chang, R. Schmid-Fetzer, W.A. Oates, *PANDAT software with PanEngine, PanOptimizer and PanPrecipitation for multi-component phase diagram calculation and materials property simulation.* Calphad, 2009. **33**(2): 328-342.

112. A. Graux, S. Cazottes, D. De Castro, D. San Martín, C. Capdevila, J.M. Cabrera, S. Molas, S. Schreiber, D. Mirković, F. Danoix, *Precipitation and grain growth modelling in Ti-Nb microalloyed steels.* Materialia, 2019. **5**: 100233.

113. O. Myhr, Ø. Grong, S. Andersen, *Modelling of the age hardening behaviour of Al–Mg–Si alloys.* Acta Materialia, 2001. **49**(1): 65-75.

114. M. Nicolas, A. Deschamps, *Characterisation and modelling of precipitate evolution in an Al–Zn–Mg alloy during non-isothermal heat treatments.* Acta Materialia, 2003. **51**(20): 6077-6094.

115. S. Samaras, *Modelling of microstructure evolution during precipitation processes: a population balance approach of the KWN model.* Modelling Simulation in Materials Science and Engineering, 2006. **14**(8): 1271.

116. A. Eivani, H. Ahmed, J. Zhou, J. Duszczyk, *An experimental and theoretical investigation of the formation of Zr-containing dispersoids in Al–4.5 Zn–1Mg aluminum alloy.* Materials Science and Engineering: A, 2010. **527**(9): 2418-2430.

117. S. Samaras, *Modelling of microstructure evolution during precipitation processes: a population balance approach of the KWN model.* Modelling and Simulation in Materials Science and Engineering, 2006. **14**(8): 1271.

118. S. Celotto, *TEM study of continuous precipitation in Mg–9 wt%Al–1 wt%Zn alloy.* Acta Materialia, 2000. **48**(8): 1775-1787.

119. J.D. Robson, *Modeling competitive continuous and discontinuous precipitation.* Acta Materialia, 2013. **61**(20): 7781-7790.

120. S. Celotto, T.J. Bastow, *Study of precipitation in aged binary Mg–Al and ternary Mg–Al–Zn alloys using 27Al NMR spectroscopy.* Acta Materialia, 2001. **49**(1): 41-51.

121. D. Bardel, M. Perez, D. Nelias, A. Deschamps, C.R. Hutchinson, D. Maisonnette, T. Chaise, J. Garnier, F. Bourlier, *Coupled precipitation and yield strength modelling for non-isothermal treatments of a 6061 aluminium alloy.* Acta Materialia, 2014. **62**: 129-140.

122. R. CHEN, Q. XU, B. LIU, *Modelling investigation of precipitation kinetics and strengthening for needle/rod-shaped precipitates inal-mg-si alloys.* Acta Metall Sin, 2016. **52**(8): 987-999.

123. M. Paliwal, I.-H. Jung, *Precipitation kinetic model and its applications to Mg alloys.* Calphad, 2019. **64**: 196-204.

124. J. Robson, C. Paa-Rai, *The interaction of grain refinement and ageing in magnesium–zinc–zirconium (ZK) alloys.* Acta Materialia, 2015. **95**: 10-19.

125. V. Vaithyanathan, C. Wolverton, L.Q. Chen, *Multiscale modeling of precipitate microstructure evolution.* Physical review letters, 2002. **88**(12): 125503.

126. V. Vaithyanathan, C. Wolverton, L. Chen, *Multiscale modeling of θ′ precipitation in Al–Cu binary alloys.* Acta Materialia, 2004. **52**(10): 2973-2987.

127. J. Zhu, T. Wang, A. Ardell, S. Zhou, Z. Liu, L.J.A.m. Chen, *Three-dimensional phase-field simulations of coarsening kinetics of γ′ particles in binary Ni–Al alloys.* 2004. **52**(9): 2837-2845.

128. Y. Song, B. Radhakrishnan, S. Gorti, R. Acharya, *Precipitate growth kinetics under inhomogeneous concentration fields using a phase-field model.* Physical Review Materials, 2021. **5**(5): 053401.

129. C.O. Yenusah, Y. Ji, Y. Liu, T.W. Stone, M.F. Horstemeyer, L.-Q. Chen, L. Chen, *Three-dimensional Phase-field simulation of γ "precipitation kinetics in Inconel 625 during heat treatment.* Computational Materials Science, 2021. **187**: 110123.

130. E. Clouet, L. Laé, T. Épicier, W. Lefebvre, M. Nastar, A. Deschamps, *Complex precipitation pathways in multicomponent alloys.* Nature materials, 2006. **5**(6): 482-488.

131. E. Clouet, M. Nastar, C. Sigli, *Nucleation of Al 3 Zr and Al 3 Sc in aluminum alloys: From kinetic Monte Carlo simulations to classical theory.* Physical Review B, 2004. **69**(6): 064109.

132. E. Clouet, M. Nastar, A. Barbu, C. Sigli, G. Martin, *Precipitation in Al-Zr-Sc alloys: A comparison between kinetic Monte Carlo, cluster dynamics and classical nucleation theory.* Solid-Solid Phase Transformations in Inorganic Materials, 2005.

133. C.S. Roberts, *Magnesium and its Alloys*. 1960: Wiley.

134. S.R. Kada, *Deformation of magnesium alloys during laboratory scale in-situ x-ray diffraction*. 2013, Deakin University.

135. P. Partridge, *The crystallography and deformation modes of hexagonal close-packed metals.* Metallurgical reviews, 1967. **12**(1): 169-194.

136. Q. Yu, *Cyclic Plastic Deformation, Fatigue, and the Associated Micro-Mechanisms in Magnesium: from Single Crystal to Polycrystal*. 2014.

137. D. Hull, D.J. Bacon, *Introduction to dislocations*. 2001: Butterworth-Heinemann.

138. L. Wu, S. Agnew, D. Brown, G. Stoica, B. Clausen, A. Jain, D. Fielden, P. Liaw, *Internal stress relaxation and load redistribution during the twinning–detwinning-dominated cyclic deformation of a wrought magnesium alloy, ZK60A.* Acta Materialia, 2008. **56**(14): 3699-3707.

139. X.-L. Nan, H.-Y. Wang, L. Zhang, J.-B. Li, Q.-C. Jiang, *Calculation of Schmid factors in magnesium: Analysis of deformation behaviors.* Scripta Materialia, 2012. **67**(5): 443-446.

140. W.D. Callister, D.G. Rethwisch, *Materials science and engineering: an introduction*. Vol. 7. 2007: John wiley & sons New York.

141. E. Burke, W. Hibbard, *Plastic deformation of magnesium single crystals.* JOM, 1952. **4**(3): 295-303.

142. S. Agnew, *Deformation mechanisms of magnesium alloys*, in *Advances in wrought magnesium alloys*. 2012, Elsevier. 63-104.

143. J.D. Robson, *Critical Assessment 9: Wrought magnesium alloys.* Materials Science and Technology, 2015. **31**(3): 257-264.

144. H. Asgari, J.A. Szpunar, A.G. Odeshi, *Texture evolution and dynamic mechanical behavior of cast AZ magnesium alloys under high strain rate compressive loading.* Materials & Design, 2014. **61**: 26-34.

145. G. Taylor, *Plastic strain in metals: Journal of the Institute of Metals, v. 62.* 1938.

146. M. Barnett, *Twinning and the ductility of magnesium alloys: Part I:"Tension" twins.* Materials Science and Engineering: A, 2007. **464**(1-2): 1-7.

147. A. Chapuis, J.H. Driver, *Temperature dependency of slip and twinning in plane strain compressed magnesium single crystals.* Acta Materialia, 2011. **59**(5): 1986-1994.

148. B.C. Wonsiewicz, *Plasticity of magnesium crystals*. 1966, Massachusetts Institute of Technology.

149. R.E. Reed-Hill, W.D. Robertson, *Deformation of magnesium single crystals by nonbasal slip.* JOM, 1957. **9**(4): 496-502.

150. T. Obara, H. Yoshinga, S. Morozumi, *{11$\bar{2}$2}< 1123> Slip system in magnesium.* Acta Metallurgica, 1973. **21**(7): 845-853.

151. T.H. Courtney, *Mechanical behavior of materials*. 2005: Waveland Press.

152. S. Agnew, D. Brown, C. Tomé, *Validating a polycrystal model for the elastoplastic response of magnesium alloy AZ31 using in situ neutron diffraction.* Acta materialia, 2006. **54**(18): 4841-4852.

153. W. Hartt, R. Reed-Hill, *Internal deformation and fracture of second-order/1011/-/1012/twins in magnesium.* 1968.

154. K.H. Eckelmeyer, R.W. Hertzberg, *Deformation in wrought Mg− 9Wt Pct Y.* Metallurgical Transactions, 1970. **1**(12): 3411-3414.

155. R. Abbaschian, R.E. Reed-Hill, *Physical Metallurgy Principles-SI Version*. 2009: Cengage Learning.

156. J. Christian, S. Mahajan, *Deformation twinning.* Progress in materials science, 1995. **39(1-2)**: 1-157.

157. A. Khosravani, D. Fullwood, B. Adams, T. Rampton, M. Miles, R. Mishra, *Nucleation and propagation of {101¯ 2} twins in AZ31 magnesium alloy.* Acta Materialia, 2015. **100**: 202-214.

158. I. Beyerlein, L. Capolungo, P. Marshall, R. McCabe, C. Tomé, *Statistical analyses of deformation twinning in magnesium.* Philosophical Magazine, 2010. **90**(16): 2161-2190.

159. M. Bevis, E. Crellin, *The geometry of twinning and phase transformations in crystalline polyethylene.* Polymer, 1971. **12**(11): 666-684.

160. R. Bell, R. Cahn, *The nucleation problem in deformation twinning.* Acta Metallurgica, 1953. **1**(6): 752-753.

161. H. Qiao, M. Barnett, P. Wu, *Modeling of twin formation, propagation and growth in a Mg single crystal based on crystal plasticity finite element method.* International Journal of Plasticity, 2016. **86**: 70-92.

162. P. Wu, X. Guo, H. Qiao, D. Lloyd, *A constitutive model of twin nucleation, propagation and growth in magnesium crystals.* Materials Science and Engineering: A, 2015. **625**: 140-145.

163. J. Wang, I. Beyerlein, C. Tomé, *An atomic and probabilistic perspective on twin nucleation in Mg.* Scripta Materialia, 2010. **63**(7): 741-746.

164. N. Thompson, D. Millard, *XXXVIII. Twin formation, in cadmium.* The London, Edinburgh, and Dublin Philosophical Magazine and Journal of Science, 1952. **43**(339): 422-440.

165. S. Mendelson, *Zonal dislocations and twin lamellae in hcp metals.* Materials Science and Engineering, 1969. **4**(4): 231-242.

166. S. Mendelson, *Dislocation dissociations in hcp metals.* Journal of applied physics, 1970. **41**(5): 1893-1910.

167. J. Blahovec, F. Kroupa, *A dislocation model of twinning.* physica status solidi (a), 1972. **11**(1): K21-K25.

168. L. Capolungo, I. Beyerlein, *Nucleation and stability of twins in hcp metals.* Physical review B, 2008. **78**(2): 024117.

169. M. Yoo, *Interaction of slip dislocations with twins in hcp metals*. 1969, Oak Ridge National Lab., Tenn.

170. A. Serra, R. Pond, D. Bacon, *Computer simulation of the structure and mobility of twinning disclocations in hcp metals.* Acta metallurgica et materialia, 1991. **39**(7): 1469-1480.

171. A. Serra, D. Bacon, *A new model for {10 1 2} twin growth in hcp metals.* Philosophical Magazine A, 1996. **73**(2): 333-343.

172. C. Bettles, M. Barnett, *Advances in wrought magnesium alloys: fundamentals of processing, properties and applications*. 2012: Elsevier.

173. M. Barnett, Z. Keshavarz, M. Nave, *Microstructural features of rolled Mg-3Al-1Zn.* Metallurgical and Materials Transactions A, 2005. **36**(7): 1697-1704.

174. O. Muránsky, D. Carr, P. Šittner, E. Oliver, *In situ neutron diffraction investigation of deformation twinning and pseudoelastic-like behaviour of extruded AZ31 magnesium alloy.* International Journal of Plasticity, 2009. **25**(6): 1107-1127.

175. M. Barnett, M. Setty, F. Siska, *Estimating critical stresses required for twin growth in a magnesium alloy.* Metallurgical and Materials Transactions A, 2013. **44**(7): 2962-2969.

176. M.R. Barnett, N. Stanford, A. Ghaderi, F. Siska, *Plastic relaxation of the internal stress induced by twinning.* Acta materialia, 2013. **61**(20): 7859-7867.

177. E. Kelley, W. Hosford, *Plane-strain compression of magnesium and magnesium alloy crystals.* Trans Met Soc AIME, 1968. **242**(1): 5-13.

178. N. Stanford, M. Barnett, *Solute strengthening of prismatic slip, basal slip and {101¯ 2} twinning in Mg and Mg–Zn binary alloys.* International Journal of Plasticity, 2013. **47**: 165-181.

179. Y. Liu, N. Li, M.A. Kumar, S. Pathak, J. Wang, R.J. Mccabe, N.A. Mara, C.N. Tome, *Experimentally quantifying critical stresses associated with basal slip and twinning in magnesium using micropillars.* Acta Materialia, 2017. **135**: 411-421.

180. J. Wang, N. Stanford, *Investigation of precipitate hardening of slip and twinning in Mg5% Zn by micropillar compression.* Acta Materialia, 2015. **100**: 53-63.

181. R. Sánchez-Martín, M.T. Pérez-Prado, J. Segurado, J. Bohlen, I. Gutiérrez-Urrutia, J. Llorca, J.M. Molina-Aldareguia, *Measuring the critical resolved shear stresses in Mg alloys by instrumented nanoindentation.* Acta Materialia, 2014. **71**: 283-292.

182. S. Agnew, C. Tomé, D. Brown, T. Holden, S. Vogel, *Study of slip mechanisms in a magnesium alloy by neutron diffraction and modeling.* Scripta Materialia, 2003. **48**(8): 1003-1008.

183. S.R. Kada, P. Lynch, M. Barnett, *Development of a laboratory-based transmission diffraction technique for in situ deformation studies of Mg alloys.* Journal of Applied Crystallography, 2015. **48**(2): 365-376.

184. H. Abdolvand, M. Majkut, J. Oddershede, J.P. Wright, M.R. Daymond, *Study of 3-D stress development in parent and twin pairs of a hexagonal close-packed polycrystal: Part I–in-situ three-dimensional synchrotron X-ray diffraction measurement.* Acta Materialia, 2015. **93**: 246-255.

185. S.R. Kada, P.A. Lynch, J.A. Kimpton, M.R. Barnett, *In-situ X-ray diffraction studies of slip and twinning in the presence of precipitates in AZ91 alloy.* Acta Materialia, 2016. **119**: 145-156.

186. M. Barnett, *A Taylor model based description of the proof stress of magnesium AZ31 during hot working.* Metallurgical and materials transactions A, 2003. **34**(9): 1799-1806.

187. S. Agnew, M. Yoo, C. Tome, *Application of texture simulation to understanding mechanical behavior of Mg and solid solution alloys containing Li or Y.* Acta Materialia, 2001. **49**(20): 4277-4289.

188. B. Clausen, C. Tomé, D. Brown, S. Agnew, *Reorientation and stress relaxation due to twinning: modeling and experimental characterization for Mg.* Acta Materialia, 2008. **56**(11): 2456-2468.

189. O. Muránsky, D. Carr, M. Barnett, E. Oliver, P. Šittner, *Investigation of deformation mechanisms involved in the plasticity of AZ31 Mg alloy: In situ neutron diffraction and EPSC modelling.* Materials Science and Engineering: A, 2008. **496**(1-2): 14-24.

190. N. Stanford, J. Geng, Y.B. Chun, C.H.J. Davies, J.F. Nie, M.R. Barnett, *Effect of plate-shaped particle distributions on the deformation behaviour of magnesium alloy AZ91 in tension and compression.* Acta materialia, 2012. **60**(1): 218-228.

191. O. Muránsky, M. Barnett, D. Carr, S. Vogel, E. Oliver, *Investigation of deformation twinning in a fine-grained and coarse-grained ZM20 Mg alloy: Combined in situ neutron diffraction and acoustic emission.* Acta materialia, 2010. **58**(5): 1503-1517.

192. S. Celotto, *TEM study of continuous precipitation in Mg–9 wt% Al–1 wt% Zn alloy.* Acta materialia, 2000. **48**(8): 1775-1787.

193. M. Gharghouri, G. Weatherly, J. Embury, *The interaction of twins and precipitates in a Mg-7.7 at.% Al alloy.* Philosophical Magazine A, 1998. **78**(5): 1137-1149.

194. I. Polmear, *Light alloys: from traditional alloys to nanocrystals*. 2005: Elsevier.

195. N. Stanford, M. Barnett, *Effect of particles on the formation of deformation twins in a magnesium-based alloy.* Materials Science and Engineering: A, 2009. **516**(1-2): 226-234.

196. J. Jain, P. Cizek, W.J. Poole, M.R. Barnett, *Precipitate characteristics and their effect on the prismatic-slip-dominated deformation behaviour of an Mg–6 Zn alloy.* Acta Materialia, 2013. **61**(11): 4091-4102.

197. J. Wang, N. Stanford, *Investigation of precipitate hardening of slip and twinning in Mg5%Zn by micropillar compression.* Acta Materialia, 2015. **100**: 53-63.

198. S.R. Agnew, R.P. Mulay, F.J. Polesak, C.A. Calhoun, J.J. Bhattacharyya, B. Clausen, *In situ neutron diffraction and polycrystal plasticity modeling of a Mg–Y–Nd–Zr alloy: Effects of precipitation on individual deformation mechanisms.* Acta Materialia, 2013. **61**(10): 3769-3780.

199. J. Buha, *Interrupted ageing of Al-Mg-Si-Cu alloys*. 2005, University of New South Wales.

200. Y. Chen, *The Effect of Interrupted Ageing on the Strength and Elongation of Precipitation Hardened Aluminium Alloys*. 2012, Monash University.

201. U.F. Kocks, K. UF, A. AS, A. MF, *Thermodynamics and kinetics of slip.* 1975.

202. A. Deschamps, Y. Brechet, *Influence of predeformation and ageing of an Al–Zn–Mg alloy—II. Modeling of precipitation kinetics and yield stress.* Acta Materialia, 1998. **47**(1): 293-305.

203. F. Wang, J.J. Bhattacharyya, S.R. Agnew, *Effect of precipitate shape and orientation on Orowan strengthening of non-basal slip modes in hexagonal crystals, application to magnesium alloys.* Materials Science and Engineering: A, 2016. **666**: 114-122.

204. E.L.S. Solomon, E.A. Marquis, *Deformation behavior of* β' *and* β''' *precipitates in Mg-RE alloys.* Materials Letters, 2018. **216**: 67-69.

205. J.J. Bhattacharyya, F. Wang, N. Stanford, S.R. Agnew, *Slip mode dependency of dislocation shearing and looping of precipitates in Mg alloy WE43.* Acta Materialia, 2018. **146**: 55-62.

206. T. Nakata, J.J. Bhattacharyya, S.R. Agnew, S. Kamado, *Unexpected influence of prismatic plate-shaped precipitates on strengths and yield anisotropy in an extruded Mg-0.3Ca-1.0In-0.1Al-0.2Mn (at.%) alloy.* Scripta Materialia, 2019. **169**: 70-75.

207. J. Geng, Y. Chun, N. Stanford, C. Davies, J. Nie, M. Barnett, *Processing and properties of Mg–6Gd–1Zn–0.6 Zr: Part 2. Mechanical properties and particle twin interactions.* Materials Science and Engineering: A, 2011. **528**(10-11): 3659-3665.

208. M. Matsuda, S. Ii, Y. Kawamura, Y. Ikuhara, M. Nishida, *Interaction between long period stacking order phase and deformation twin in rapidly solidified Mg97Zn1Y2 alloy.* Materials Science and Engineering: A, 2004. **386**(1-2): 447-452.

209. J. Jain, W. Poole, C. Sinclair, M. Gharghouri, *Reducing the tension–compression yield asymmetry in a Mg–8Al–0.5 Zn alloy via precipitation.* Scripta Materialia, 2010. **62**(5): 301-304.

210. J. Robson, N. Stanford, M. Barnett, *Effect of precipitate shape on slip and twinning in magnesium alloys.* Acta materialia, 2011. **59**(5): 1945-1956.

211. J. Robson, *The effect of internal stresses due to precipitates on twin growth in magnesium.* Acta Materialia, 2016. **121**: 277-287.

212. C. Liu, P. Shanthraj, J.D. Robson, M. Diehl, S. Dong, J. Dong, W. Ding, D. Raabe, *On the interaction of precipitates and tensile twins in magnesium alloys.* Acta Materialia, 2019. **178**: 146-162.

213. J. Jain, P. Cizek, W.J. Poole, M.R. Barnett, *The role of back stress caused by precipitates on {101¯2} twinning in a Mg–6Zn alloy.* Materials Science and Engineering: A, 2015. **647**: 66-73.

214. N. Stanford, A.S. Taylor, P. Cizek, F. Siska, M. Ramajayam, M.R. Barnett, *{101¯2} Twinning in magnesium-based lamellar microstructures.* Scripta Materialia, 2012. **67**(7): 704-707.

215. J.D. Robson, N. Stanford, M.R. Barnett, *Effect of particles in promoting twin nucleation in a Mg–5wt.% Zn alloy.* Scripta Materialia, 2010. **63**(8): 823-826.

216. J. Wang, M.R.G. Ferdowsi, S.R. Kada, C.R. Hutchinson, M.R. Barnett, *Influence of precipitation on yield elongation in Mg-Zn alloys.* Scripta Materialia, 2019. **160**: 5-8.

217. J. Wang, M. Ramajayam, E. Charrault, N. Stanford, *Quantification of precipitate hardening of twin nucleation and growth in Mg and Mg-5Zn using micro-pillar compression.* Acta Materialia, 2019. **163**: 68-77.

218. P. Hidalgo-Manrique, J. Robson, M. Pérez-Prado, *Precipitation strengthening and reversed yield stress asymmetry in Mg alloys containing rare-earth elements: A quantitative study.* Acta Materialia, 2017. **124**: 456-467.

219. J.D. Robson, M.R. Barnett, *The effect of precipitates on twinning in magnesium alloys.* Advanced Engineering Materials, 2019. **21**(4): 1800460.

220. M.R. Barnett, H. Wang, T. Guo, *An Orowan precipitate strengthening equation for mechanical twinning in Mg.* International Journal of Plasticity, 2019. **112**: 108-122.

221. v.L. Nordheim, C. Gorter, *Bemerkungen über thermokraft und widerstand.* Physica, 1935. **2**: 383-390.

222. K.S. Wallwork, B.J. Kennedy, D. Wang. *The high resolution powder diffraction beamline for the Australian Synchrotron*. in *AIP Conference Proceedings*. 2007. American Institute of Physics.

223. J.S. Evans. *Advanced input files & parametric quantitative analysis using topas*. in *Materials Science Forum*. 2010. Trans Tech Publ.

224. A. Balan, M. Perez, T. Chaise, S. Cazottes, D. Bardel, F. Corpace, F. Pichot, A. Deschamps, F. De Geuser, D. Nelias, *Precipitation of γ "in Inconel 718 alloy from microstructure to mechanical properties.* Materialia, 2021. **20**: 101187.

225. J. Friedel, *Dislocations.(Pergamon Press, Oxford-London-Edinburgh-New York-Paris-Frankfurt.* 1964.

226. M. Peach, J. Koehler, *The forces exerted on dislocations and the stress fields produced by them.* Physical Review, 1950. **80**(3): 436.

227. D. Bardel, A. Balan, G. Meyruey, M. Perez, Y. Yang, *Precipitates strengthening*, in *Internal document*. 2021.

228. I. Polmear, *Magnesium alloys and applications.* Materials science & technology, 1994. **10**(1): 1-16.

229. Handbook, *Chemical and Electrolytic Polishing.* ASM International, 2004. **9**: 281-293.

230. K. Momma, F. Izumi, *VESTA 3 for three-dimensional visualization of crystal, volumetric and morphology data.* Journal of applied crystallography, 2011. **44**(6): 1272-1276.

231. B. Smith, *knovel: Engineering & Scientific Online References.* Reference Reviews, 2002.

232. J.-O. Andersson, T. Helander, L. Höglund, P. Shi, B. Sundman, *Thermo-Calc & DICTRA, computational tools for materials science.* Calphad, 2002. **26**(2): 273-312.

233. S. Chen, S. Daniel, F. Zhang, Y. Chang, X. Yan, F. Xie, R. SchmidFetzer, W. Oates, *The PANDAT software package and its applications.* Calphad, 2002. **26**(2): 175-188.

234. C. Kammerer, N.S. Kulkarni, R.J. Warmack, Y.H. Sohn, *Interdiffusion and impurity diffusion in polycrystalline Mg solid solution with Al or Zn.* Journal of alloys & compounds, 2014. **617**: 968-974.

235. G. Meyruey, V. Massardier, W. Lefebvre, M. Perez, *Over-ageing of an Al-Mg-Si alloy with silicon excess.* Materials Science and Engineering: A, 2018. **730**: 92-105.

236. D. Eskin, V. Massardier, P. Merle, *A study of high-temperature precipitation in Al–Mg–Si alloys with an excess of silicon.* Journal of materials science, 1999. **34**(4): 811-820.

237. V. Massardier, T. Epicier, P. Merle, *Correlation between the microstructural evolution of a 6061 aluminium alloy and the evolution of its thermoelectric power.* Acta materialia, 2000. **48**(11): 2911-2924.

238. D. Dafir, *Etude de l'influence du renfort sur la cinétique de précipitation dans un composite 6061/SiCp élabore par métallurgie des poudres*. 1993, Lyon, INSA.

239. Y.-P. Xie, Z.-Y. Wang, Z. Hou, *The phase stability and elastic properties of MgZn2 and Mg4Zn7 in Mg–Zn alloys.* Scripta Materialia, 2013. **68**(7): 495-498.

240. X. Li, H. Ma, Z. Dai, Y. Qian, L. Hu, Y. Xie, *First-principles study of coherent interfaces of Laves-phase MgZn2 and stability of thin MgZn2 layers in Mg-Zn alloys.* Journal of Alloys & Compounds, 2017. **696**: 109-117.

241. M. Paliwal, I. Jung, *Precipitation kinetic model and its applications to Mg alloys.* Calphad, 2019. **64**: 196-204.

242. J.M. Rosalie, H. Somekawa, A. Singh, T. Mukai, *The effect of size and distribution of rod-shaped precipitates on the strength and ductility of a Mg–Zn alloy.* Materials Science and Engineering: A, 2012. **539**: 230-237.

243. A. Simar, Y. Bréchet, B. De Meester, A. Denquin, C. Gallais, T. Pardoen, *Integrated modeling of friction stir welding of 6xxx series Al alloys: Process, microstructure and properties.* Progress in materials science, 2012. **57**(1): 95-183.

244. B. Lagowski, J. Meier, *Characteristics of sand-cast magnesium–zinc alloys.* Trans. American Foundrymen’s Society, 1964. **72**: 561-574.

245. H. Somekawa, Y. Osawa, T. Mukai, *Effect of solid-solution strengthening on fracture toughness in extruded Mg–Zn alloys.* Scripta materialia, 2006. **55**(7): 593-596.

246. N. Stanford, M.R. Barnett, *Effect of particles on the formation of deformation twins in a magnesium-based alloy.* Materials Science and Engineering: A, 2009. **516**(1): 226-234.

247. C.H. Zenk, L. Feng, D. McAllister, Y. Wang, M.J. Mills, *Shearing mechanisms of co-precipitates in IN718.* Acta Materialia, 2021. **220**: 117305.

248. E. Christiansen, C.D. Marioara, B. Holmedal, O.S. Hopperstad, R. Holmestad, *Nano-scale characterisation of sheared β” precipitates in a deformed Al-Mg-Si alloy.* Scientific reports, 2019. **9**(1): 1-11.

249. N. Stanford, M.R. Barnett, *Solute strengthening of prismatic slip, basal slip and {101 2} twinning in Mg and Mg–Zn binary alloys.* International Journal of Plasticity, 2013. **47**: 165-181.

250. A. Tehranchi, B. Yin, W. Curtin, *Solute strengthening of basal slip in Mg alloys.* Acta Materialia, 2018. **151**: 56-66.

251. E. Flügel, *Microfacies of carbonate rocks: analysis, interpretation and application*. 2013: Springer Science & Business Media.

252. J.D. Robson, N. Stanford, M.R. Barnett, *Effect of particles in promoting twin nucleation in a Mg–5 wt.% Zn alloy*. Scripta materialia, 2010. **63**(8): 823-826.

253. N. Ecob, B. Ralph, *The effect of grain size on deformation twinning in a textured zinc alloy*. Journal of Materials Science, 1983. **18**(8): 2419-2429.

254. M.R. Barnett, M.D. Nave, A. Ghaderi, *Yield point elongation due to twinning in a magnesium alloy*. Acta materialia, 2012. **60**(4): 1433-1443.